

Exploring Primordial Gaussian Fields through Constrained Realizations

Wendy Docters
under supervision of Rien van de Weygaert

May 31, 2010

Contents

1	Introduction	4
1.1	Nature of the primordial density field	5
1.2	Evolution	7
2	Constrained Field Formalism	10
2.1	One plus one equals one	10
2.1.1	Introduction to Gaussian random fields	11
2.1.2	User-specified conditions	12
2.2	The Hoffman-Ribak method	14
2.2.1	Fourierspace	15
2.3	Applications of the Hoffman-Ribak Method	17
2.3.1	Constrained peak formalism	17
2.4	Constraint probability	24
2.4.1	Change of coordinate system.	28
2.5	Other methods	29
2.5.1	Convolution method	29
3	Realizations	35
3.1	Cosmological parameters	36
3.2	Presentation of the simulation results	36
3.3	Creating a constrained realization	36
3.3.1	Residual field	38
3.4	Simulation limitations	38
3.4.1	Scale	38
3.4.2	Position	40
3.5	Density constraints	41
3.5.1	Single Objects: Peaks	42
3.5.2	Single Objects: Voids	49
3.5.3	Multiple Objects	51
3.6	Velocity constraints	55
3.6.1	Peculiar velocity	55
3.6.2	Shear constraints	62
4	GRF's in spherical harmonics	67
4.1	Density field in spherical harmonics	67
4.2	General base	69
4.3	Fourier space	70
4.4	Density field in Spherical harmonics	71

4.5	Constrained realizations: Binney and Quinn formalism	72
5	Applications	76
5.1	Specific objects: voids, galaxies, halos, etc.	76
5.1.1	Testing theories	79
5.2	Local Universe	80
5.2.1	Reconstruction method	83
5.2.2	Extra Galactic Magnetic Field	84
6	Summary and Discussion	88
A	Linear evolution of perturbation fields	97
A.1	Solutions	98
A.1.1	Solution for density perturbations	98
A.1.2	Gravitational potential perturbations	99
A.1.3	Velocity perturbations	99
B	Defining most likely field	101
C	Proof statistics residual field	102
D	Overview configurations	103
E	General solution time-independent Schrodinger equation in spherical coordinates	107
E.1	Expressions for the spherical harmonics and spherical Bessel functions	109

Abstract

The gravitational instability scenario suggests that the large scale structure observed in the universe today grew from small perturbations in the density and velocity field. The evolution of these perturbations is a nonlinear process and can be recreated using N-body simulations. They are used as laboratories by astronomers to study the formation and evolution of different types of structure. The primordial cosmological density field is commonly assumed to be a Gaussian random field, whose properties are dictated by the cosmological parameters and the content of the universe. Most N-body simulations start from a realization of a purely random Gaussian field. In the case of certain applications, it would be desirable to be able to zoom in on a region with specific properties. To this end, one can use a constrained field formalism. This can be done by constructing user-specified initial conditions for N-body simulations. By imposing constraints on the Gaussian density and velocity perturbation field, the evolution and formation of the structure can be influenced.

This research reviews a number of methods of constructing constrained realizations. The first systematic was Bertschinger (1987), stating that a constrained realization is the sum of the ensemble average of all fields subject to the desired set of constraints and a field containing the random fluctuations of the power spectrum. The constrained realization was generated using Monte Carlo simulation techniques in Fourier space. Hoffman & Ribak (1991) realized that the statistics of the residual field were independent of the numerical values chosen, making the algorithm designed by Bertschinger efficient for a large number of constraints. Applications of the Hoffman-Ribak method are studied, in particular the constrained peak formalism by van de Weygaert & Bertschinger (1996). This allows us to impose up to 18 different constraints per object, sculpting the local density field and the dynamics of the evolution. The computational implementation is used in this research to generate a number of constrained realizations which can be used as initial conditions for N-body simulations. A coordinate change in this method, proposed by Binney & Quinn (1991) is studied.

Other methods are also mentioned, such as the convolution method of Salmon (1996). By calculating the convolution of white noise with a filter specified by the power spectrum, a Gaussian random field can be created. Filtering this field with a specific filter creates the new Gaussian field with the same statistics as the desired field.

The various methods described are used in projects, such as the CLUES project to simulate the large scale structure in our Local Group, the void simulations done by van de Weygaert & van Kampen (1993) to study the formation of voids in different cosmological contexts under various sets of constraints and the study of the evolution of the Extra Galactic Magnetic Field of Dolag *et al.* (2005).

Chapter 1

Introduction

Due to constantly improving technology, the field of astronomy has been experiencing an amazingly rapid development. Up till the beginning of the nineties, virialized galaxy super clusters were believed to be the largest structures in the universe. (Oort, 1983) Deeper and high resolution observations done by various redshift surveys proved this not to be the case. They revealed that matter in the universe is arranged in a web like structure, consisting of nodes, connected by planar and filamentary overdensities, surrounding near-empty regions. The web is woven by threads called filaments and sheetlike structures called walls and at their intersections, nodes are formed. The clusters and super clusters of galaxies can be found in the nodes, filaments and walls. The near-empty regions in the universe are called voids. This structure was given the name of 'Cosmic Web'. (Bond *et al.*, 1996) One of the results of such a redshift sky survey can be seen in figure 1.1. The figure shows that the same structural behavior is seen at higher redshifts, but at smaller scales. This is an indication for the gravitational instability scenario. In this framework structure formation grows through mergers of smaller substructure under the influence of gravity, indicating that more massive structure will form as time progresses. (Zel'dovich, 1970)

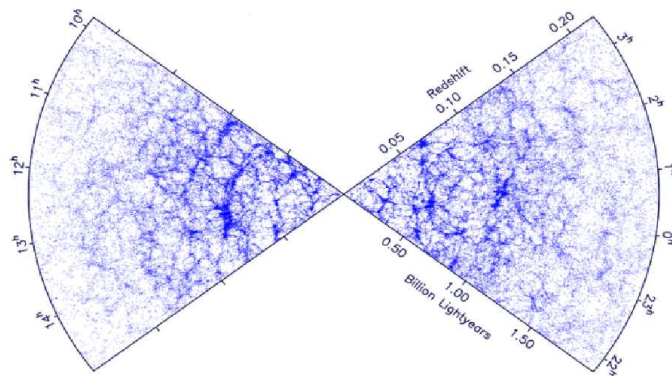


Figure 1.1: Results of the 2dF galaxy redshift survey, giving a clear picture of the web like composition of the matter in the universe.

1.1 Nature of the primordial density field

The gravitational instability scenario beholds that the large scale structure seen today grew from tiny perturbations in the primordial density and velocity field. These perturbations are believed to have originated from quantum fluctuations blown up in an inflationary era in the evolution of the universe. Evidence for this theory can be found in the temperature fluctuations in the Cosmic Microwave Background radiation (CMB). These fluctuations originate due to various gravitational effects, where the overdense regions will appear at a higher temperature in observations. The variations in temperature are therefore an imprint of the primordial power spectrum at the surface of last scattering, around 300.00 years after the Big Bang.

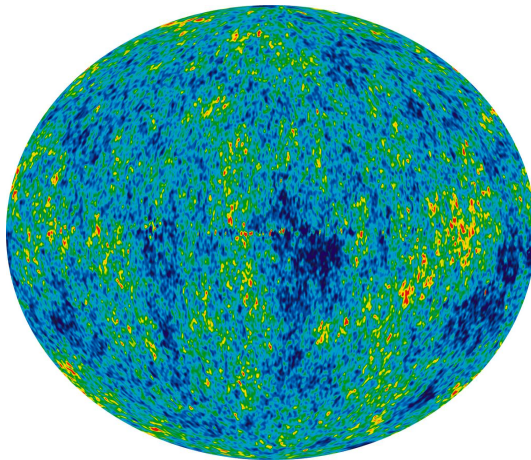


Figure 1.2: Cosmic Microwave Background Radiation. The image reveals 13.7 billion year old temperature fluctuations (shown as color differences) that correspond to the seeds that grew to become the galaxies. This image shows a temperature range of 200 micro Kelvin. Image Courtesy to the WMAP-project.

Quantum fluctuations blown up in an inflationary era create perturbation fields that are Gaussian distributed. Even if inflation is not invoked in the evolution theory of the universe, the central limit theorem argues that a Gaussian distribution could still arise if the density field is a superposition of independent Fourier modes, each with their own Gaussian probability distribution.

$$f(\mathbf{x}) = \int \frac{d\mathbf{k}}{(2\pi)^3} \hat{f}(\mathbf{k}) e^{-i\mathbf{k}\cdot\mathbf{x}} \quad (1.1)$$

where $f(\mathbf{x})$ is the density perturbation field in real space and $\hat{f}(\mathbf{k})$ are the different modes in Fourier space. The properties of a Gaussian random field are fully specified by its power spectrum $P(k)$. (Scherrer, 1992) The simplest inflationary Λ CDM model predicts a so-called scale-invariant primordial power spectrum for the density, given by $P(k) \propto k^n$. On large scales, there is a slight preference for the value of $n = 1$, which was predicted by Peebles & Yu (1970), Harrison (1970) and Zel'dovich (1970). The complete power spectrum is quantified by the transfer function and the normalization constant. An fit for the transfer function for an universe dominated by dark matter over baryonic

matter and the presence of radiation and a cosmological constant was made by Bardeen *et al.* (1986), (BBKS).

$$T(k) = \frac{\ln(1 + 2.34q)}{2.34q} [1 + 3.89q + (16.1q)^2 + (5.46q)^3 + (6.71q)^4]^{-1/4} \quad (1.2)$$

where $q \equiv k/h\Gamma \text{ Mpc}^{-1}$. The function Γ was defined by BBKS to be equal to $\Omega_m h$, where Ω_m is fraction of matter density with respect to the total density content. Sugiyama (1995) refined this expression further to:

$$q = \frac{k(T_0/2.7K)^2}{\Omega_0 h^2 \exp(-\Omega_b - \sqrt{h/0.5\Omega_b/\Omega_0}) \text{Mpc}^{-1}} \quad (1.3)$$

where T_0 is the present temperature, Ω_0 is the total matter content, Ω_b is the fraction of baryonic matter content. One way to determine the normalization constant is using the definition of cosmological parameter σ_8^2 , which is defined as the root-mean-square density variation when smoothed with a tophat-filter of radius of $8h^{-1} \text{ Mpc}$. In Fourier space, this is given by:

$$\sigma_8^2 = \frac{1}{(2\pi)^3} \int W_{TH}^2(\mathbf{k}) P(k) d\mathbf{k} \quad (1.4)$$

in which W_{TH} is the Fourier expression of the top-hat filter. The value for parameter σ_8 used in this research originates from the WMAP7 data and is equal to 0.809. (Komatsu *et al.*, 2009)

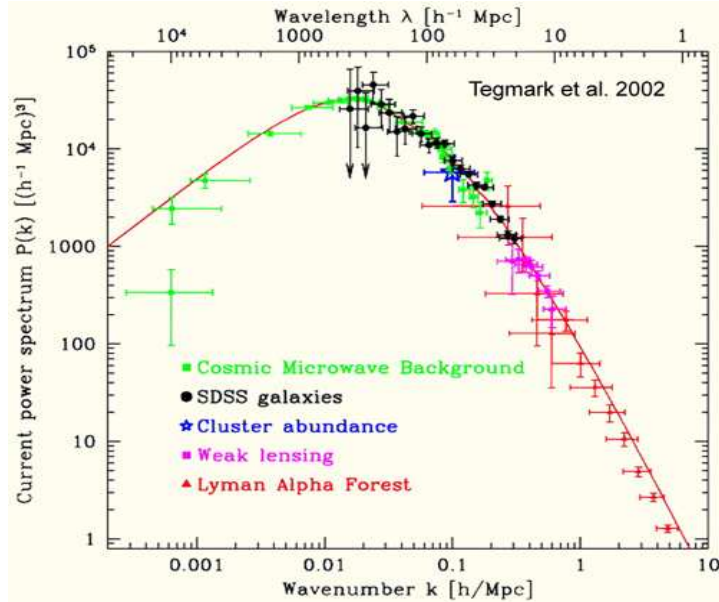


Figure 1.3: Plot of the primordial power spectrum in a Λ CDM model. The different marks represent the different kind of observations done in order to reproduce the power spectrum. Seen is the k^1 preference of Peebles & Yu (1970), Harrison (1970) and Zel'dovich (1970) before the turn-point.

1.2 Evolution

The evolution of the primordial density and velocity perturbations is described by a set of fluid equations. (see Appendix A for the specific equations) Because the perturbations are of main interest for the astronomers, comoving coordinates are chosen to describe the evolution. On large scales, the universe is considered to be homogeneous and isotropic with a mean density of ρ_u and a velocity that is equal to the expansion of the universe $H\mathbf{r}$ where H is the Hubble parameter. This is considered our static background in the comoving coordinate system. The density perturbation field with respect to this static background is defined as:

$$f(\mathbf{x}, t) = \frac{\rho(\mathbf{x}, t) - \rho_u}{\rho_u} \quad (1.5)$$

A nonzero $f(\mathbf{x}, t)$ will attract or repulse matter due to the excess gravity, inducing a corresponding velocity perturbations $\mathbf{v}(\mathbf{x}, t)$ with respect to the velocity of the universe. When the amplitudes of the density perturbations are much smaller than one, the nonlinear terms in the set of three fluid equations can be discarded. The solutions for the density and velocity perturbation fields can then be found analytically. (see Appendix A)

A positive density perturbation for example, will grow without a bound as long as the pressure forces do not counteract the infall of matter. When the pressure forces become large enough, the overdensity starts to contract, ultimately collapsing in a gravitationally bound structure. This can become a galaxy, cluster or super cluster, depending on the scale of the initial overdensity. In our exploration of the cosmic web and the development of appropriate tools to analyze structure, morphology and dynamics, it is assumed that the cosmic web is traced by a population of discrete objects, which are the galaxies in real observations. But the formation of galaxies is a nonlinear process: when the density perturbations become in the order of unity, the different scales in the perturbation fields start to interact. The nonlinear terms in the fluid equations can no longer be neglected, making it impossible to find the solutions analytically.

In order to gain insight in the formation and evolution of structure, N-body simulations are used. They are able to deal with the entire evolution of a system through the full range of linear up to highly nonlinear stages, where the particles are the traceable objects. These N-body simulations can be considered laboratories to help cosmologists understand the universe as observed today. The different processes that play a role in the formation of various types of structures can be studied. By comparing the obtained simulation results with the observations, different cosmological models and the influence of various constraints can be studied. For example, the value of cosmological parameters can be tested by re simulating the large scale structure in a region of the universe and comparing this with observations done. This is done by various research groups, such as the Millenium Project (Springel *et al.*, 2005). One of the results of the Millenium Simulation can be seen in figure 1.4, where our local universe is simulated.

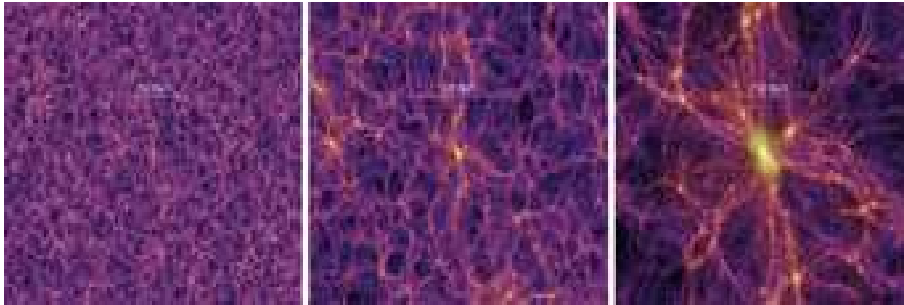


Figure 1.4: The cosmic web in a box: three slices of the Millenium Simulation of the Λ CDM model. The frames show the projected dark matter distribution in slices of $15h^{-1}Mpc$, extracted at $z = 0$ corresponding to 13.6 Gyrs after the Big Bang. The hierarchical structure can be seen. Image courtesy of V. Springel and Virgo consortium.

To recreate a certain structure based on observations, specific initial conditions should be present in the N-body simulation. One can influence the structure and its environment by imposing constraints on the density and velocity perturbation field used for the initial conditions. For example, if the desired result of the N-body simulation should be a super cluster, a peak of a certain height with respect to the background has to be found in the initial conditions. An example of different constraints is found in figure 1.5, where constraints are imposed on the density and velocity field.

A trivial way to obtain specific initial conditions is to generate unconstrained random realizations and reject those who not meet the desired constraints. However, in the cases where extreme conditions or the formation of a very large structure are longed for, this method becomes impractical. Different procedures were proposed to create user-specified initial conditions for N-body simulations. In this project, I have focused on the method of Hoffman & Ribak (1991), based on the formalism by Bertschinger (1987).

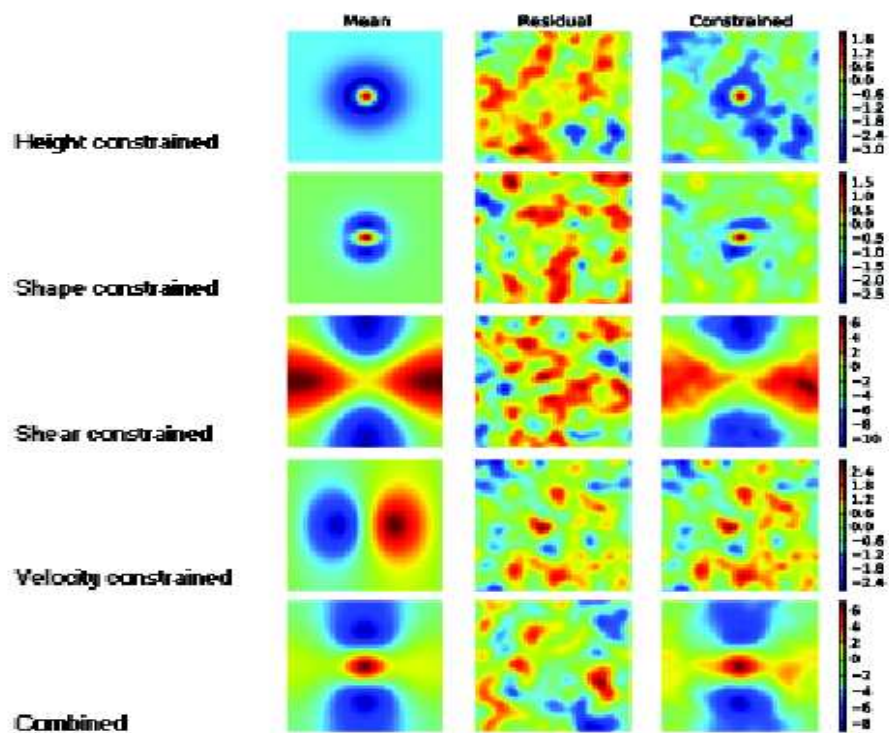


Figure 1.5: Depicting the different types of constraints, using the Hoffman-Ribak method.

Chapter 2

Constrained Field Formalism

When the importance of constrained realizations was realized, various methods to generate these were suggested. Bertschinger (1987) was the first to tackle the constrained realization problem. His formalism, extensions and applications will be discussed in the upcoming section. Another method to pass the review is the convolution method by Salmon (1996) and some of its applications.

2.1 One plus one equals one

Bertschinger (1987) was the first to set up a formalism to construct a constrained Gaussian realization. By adding two fields, the mean field $\bar{f}(\mathbf{x})$ and the residual field $F(\mathbf{x})$ a constrained realization can be built.

$$f(\mathbf{x}) = F(\mathbf{x}) + \bar{f}(\mathbf{x}) \quad (2.1)$$

The mean field $\bar{f}(\mathbf{x})$ is equal to the ensemble average of all fields obeying a desired set of constraints. By the virtue of the ergodic theorem, the ensemble average can be seen as the average over the normalization volume and is in this research denoted by angle brackets. In other words, the mean field is considered to be the most likely field. It is the weighted sum of the correlation functions between the field and the imposed constraint function, defined as $\xi_i = \langle f(\mathbf{x})C_i \rangle$, where the constraint functions C_i are linear functionals of the field denoted as $C_i = C_i[f(\mathbf{x})] = c_i$. The constraint correlation function is an indication of the measure of influence of the constraint on the field throughout the volume. The weights for each field constraint correlation are determined by the imposed constraint c_j and the inverse of the cross-correlation function between the different constraints $\xi_{ij} = \langle C_i C_j \rangle$. This defines the mean field as:

$$\bar{f}(\mathbf{x}) = \xi_i(\mathbf{x})\xi_{ij}^{-1}c_j \quad (2.2)$$

The second field is the residual field $F(\mathbf{x})$. This field embodies the field fluctuations in the power spectrum and therefore is completely specified by the choice of power spectrum. An illustration of this can be seen in figure 2.1, where in the left panel the mean field is shown, in the middle panel the residual field and

in the right plot the sum of the two, the constrained realization.

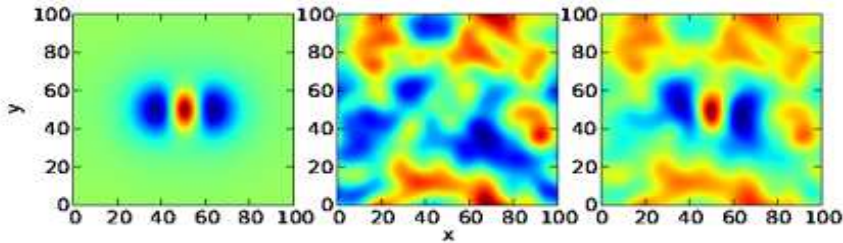


Figure 2.1: Illustration with from left to right, an illustration of the mean field, the residual field and the constrained realization. Constraints were imposed on the height, shape and curvature of a peak in the center of the simulation box. These fields were created using the program of Van de Weygaert and Bertschinger (1996).

2.1.1 Introduction to Gaussian random fields

The large scale structure is believed to have grown under the influence of gravity from primordial density and peculiar velocity perturbations that are Gaussian randomly distributed. As explained in the first chapter, this is based on inflation and the central limit theorem. On large scales, these fields are considered homogeneous and isotropic with zero mean. Gaussian fields are specified by their probability distribution function, which gives the probability that the field will have values $f(\mathbf{x}_i)$ up to $f(\mathbf{x}_j) + df(\mathbf{x}_j)$ for $j = 1, \dots, N$. Since the fields are by definition Gaussian distributed, the joint probability distribution function is defined by a set of N Gaussian probabilities all specified by their mean and variance (Bardeen *et al.*, 1986):

$$P_N(f(\mathbf{x}_1), \dots, f(\mathbf{x}_N))df(\mathbf{x}_1), \dots, df(\mathbf{x}_N) = \frac{1}{[(2\pi)^N \det(M)]^{1/2}} e^{-A} df(\mathbf{x}_1), \dots, df(\mathbf{x}_N) \quad (2.3)$$

where N is the number of points and A is defined as:

$$A \equiv \frac{1}{2} \sum_{i=1}^N \sum_{j=1}^N f(\mathbf{x}_i) K_{ij} f(\mathbf{x}_j) \quad (2.4)$$

$$= \frac{1}{2} \mathbf{f}^t K \mathbf{f} \quad (2.5)$$

where \mathbf{f} is an N -dimensional column vector with entries f_i and \mathbf{f}^t is its transpose. The matrix K is the inverse of the covariance matrix M . In case of a Gaussian field, M is specified by the autocorrelation function $\xi(\mathbf{r})$.

$$M_{ij} = \xi(\mathbf{x}_i - \mathbf{x}_j) = \langle f(\mathbf{x}_i) f(\mathbf{x}_j) \rangle \quad (2.6)$$

In the continuous limit the summations can be replaced with integrals. The joint probability distribution becomes:

$$P[f] = e^{-S[f]} D[f] \quad (2.7)$$

where $D[f]$ is a measure of the distribution function and $S[f]$ is referred to as the action integral, analogous to the action integral in path form in quantum mechanics. The expression for $S[f]$ can be obtained from eq. 2.4:

$$S[f] = \frac{1}{2} \int d\mathbf{x}_1 \int d\mathbf{x}_2 f(\mathbf{x}_1) K(\mathbf{x}_1 - \mathbf{x}_2) f(\mathbf{x}_2) \quad (2.8)$$

The action integral can be rewritten into the form of $\frac{1}{2} \mathbf{f}^t K \mathbf{f}$. Since the action integral determines the joint probability distribution function, constructing a Gaussian random field comes down to correctly sampling the action integral of the field.

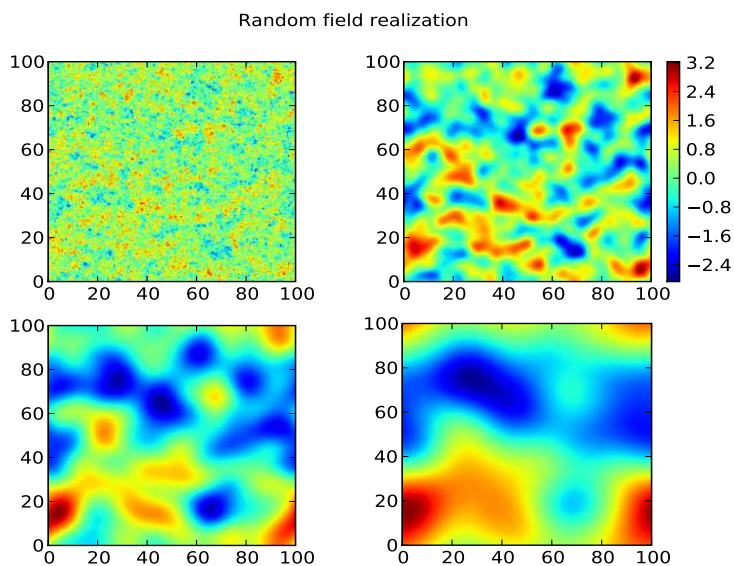


Figure 2.2: Plot of a Gaussian random field. Upper left panel is an unfiltered realization. Upper right panel is the same realization, filtered with a Gaussian filter on a scale of $2h^{-1} \text{ Mpc}$. Lower left panel is the same realization, filtered on a scale of $5h^{-1} \text{ Mpc}$ while the same realization is seen in the lower right panel filtered on a smoothing scale of $10h^{-1} \text{ Mpc}$.

Gaussian random fields can be used for setting up initial conditions for N-body simulations. By letting such a realization evolve in time, structure will evolve due to the influence of gravity and become non-Gaussian.

2.1.2 User-specified conditions

Nevertheless, there are many interesting problems in which one is interested in generating special purpose conditions which are obeyed to give some specific outcome of the simulation. For example, one would like to reconstruct the large scale structure in a particular region of the universe, such as is done by a number of groups, CLUES and the Virgo consortium being just a few of them. Generating special purpose initial conditions can be done by imposing numerical values at certain points in the simulation. This technique is called

the constrained field formalism. The set of desired constraints can be written as:

$$\Gamma = C_i[f; \mathbf{x}_i] = c_i \quad i = 1, \dots, M \quad (2.9)$$

where M is the number of constraints and c_i is the imposed numerical value. The constraint functions C_i are linear functionals of the field $f(\mathbf{x}_i)$ and the position \mathbf{x}_i and therefore also Gaussian distributed. This means that the probability distribution of a Gaussian random field $f(\mathbf{x})$ subject to a set of constraints Γ is equal to:

$$P[f | \Gamma] = \frac{P[f]}{P[\Gamma]} \quad (2.10)$$

where $P[\Gamma]$ is the probability function of the set of constraints and $P[f]$ the probability function of the random field $f(\mathbf{x})$, which is given by eq. 2.3.

A similar expression for the probability distribution function for the set of constraints can be derived. The joint probability function for the set of constraints is equal to:

$$P(C_1, C_2, \dots, C_M) dC_1, dC_2, \dots, dC_M = \frac{1}{[(2\pi)^M \det(Q)]^{1/2}} e^{-B} dC_1, \dots, dC_M \quad (2.11)$$

with

$$B \equiv \frac{1}{2} \sum_{i=1}^M \sum_{j=1}^M C_i (Q^{-1})_{ij} C_j \quad (2.12)$$

The covariance matrix of the set of constraints is defined as:

$$Q = \langle C_i(\mathbf{x}_i) C_j(\mathbf{x}_j) \rangle \quad (2.13)$$

The complete conditional probability distribution function for a Gaussian field subject to set of constraints can be defined as:

$$P[f | \Gamma] = e^{-\frac{1}{2}(\mathbf{f}^t K \mathbf{f} - \mathbf{C}^t Q^{-1} \mathbf{C})} \frac{D[f]}{D[\Gamma]} \quad (2.14)$$

where the notation of eq. 2.7 was used and \mathbf{C} is a M -dimensional column vector with entries $C_i = C_i[f; \mathbf{x}_i] = c_i$ and \mathbf{C}^t is its transpose. Note that the imposed set of constraints is now incorporated in the action integral $S[f]$, which now can be rewritten to:

$$S[F] = \frac{1}{2} \mathbf{F}^t K \mathbf{F} \quad (2.15)$$

where $F(\mathbf{x})$ is the residual field and is defined as the difference between a Gaussian field satisfying the constraint set Γ , $f(\mathbf{x})$, and the most likely set satisfying the constraint set Γ , $\bar{f}(\mathbf{x})$:

$$F(\mathbf{x}) \equiv f(\mathbf{x}) - \bar{f}(\mathbf{x}) \quad (2.16)$$

The problem of constructing a Gaussian constrained field is reduced to properly sampling the action integral of the residual field $F(\mathbf{x})$. However, when imposing a set of constraints on a Gaussian random field, the residual field is implicitly subject to a set of constraints Γ_0 , imposing the residual field to be zero at the positions of the constraints by definition. This can be seen in figure 2.3.

Construction of a constrained realization

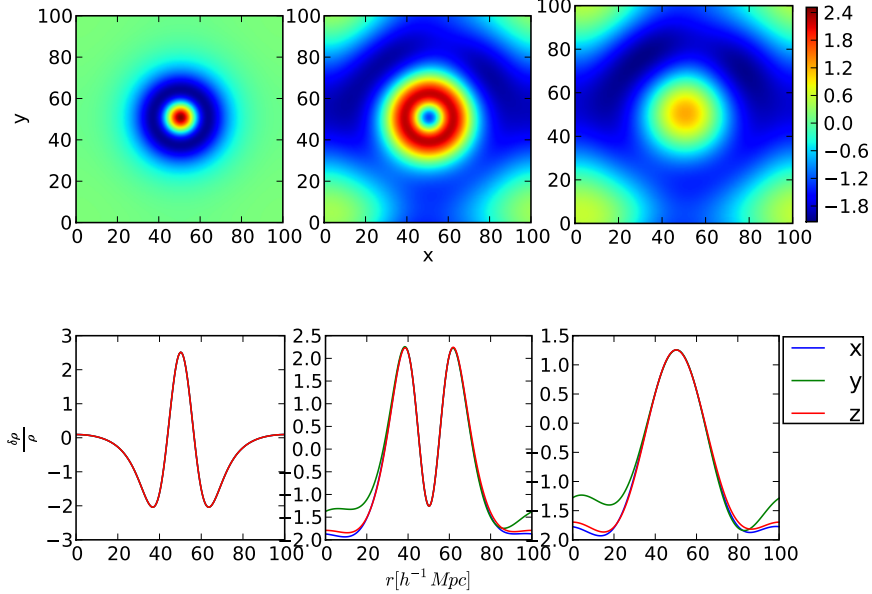


Figure 2.3: An illustration of, from left to right, a mean field, a residual field and a constrained realization. Because of the large scale of the object, hardly any fluctuations are seen. Notice that clearly the residual field is the difference between the constrained realization and the mean field. These illustrations were made using the algorithm by Van de Weygaert and Bertschinger (1996).

Bertschinger (1987) solved this problem by using Markov Chain Monte Carlo methods to sample the action integral. This was done in Fourier space, since the Fourier modes are mutually independent and the action integral is therefore diagonal:

$$S[f] = \int \frac{d\mathbf{k}}{(2\pi)^3} \frac{|\hat{F}(\mathbf{k})|^2}{2P(k)} \quad (2.17)$$

where $\hat{F}(\mathbf{k})$ are the Fourier transforms of the residual field $F(\mathbf{x})$. The algorithm requires $\Theta[(M^2+1)N]$ operations to generate one independent realization, where M is the number of constraints and N is the number of degrees of freedom, roughly equal to the number of density points. Note that for a large number of constraints or a high grid density, the system converges slowly and the algorithm becomes expansive.

2.2 The Hoffman-Ribak method

Hoffman and Ribak (1991) solved the issue of sampling the residual field. They realized that the variance of the residual field was given by:

$$\langle F^2(\mathbf{x}) | \Gamma \rangle = \sigma_0^2 - \xi_i(\mathbf{x}) \xi_{ij}^{-1} \xi_j(\mathbf{x}) \quad (2.18)$$

where $\sigma_0^2 = \langle f(\mathbf{x})f(\mathbf{x}) \rangle$. Note that the variance depends on position \mathbf{x} and is therefore neither homogeneous and isotropic. Since it is defined as the difference of two Gaussian fields with zero mean, it is also a Gaussian field with zero mean. This indicates that the distribution is completely specified by its variance. Equation 2.18 shows that the variance is independent of the imposed numerical value and that therefore the complete conditional probability distribution function of the residual field independent is of the numerical values of the constraint set. (Additional proof of this statement can be found in Appendix C and was done by van de Weygaert & Bertschinger (1996)). By realizing that the statistics of the residual field are independent of the numerical values of c_i , the method of repeatedly sampling the action integral is unnecessary: the residual field $F(\mathbf{x})$ might as well be sampled from the field subject to a set of constraints Γ as from the field subject to some arbitrary set of constraints $\tilde{\Gamma}$. Hoffman and Ribak developed the following algorithm to construct a constrained realization:

1. Create a random, unconstrained realization $\tilde{f}(\mathbf{x})$, which is a homogeneous and isotropic Gaussian random field determined by its power spectrum.
2. Calculate the values \tilde{c}_j of the realizations corresponding to the constraints $C_i(\mathbf{x}) |_{\mathbf{x}_i}$ for $i = 1, \dots, M$. These values define a set of constraints $\tilde{\Gamma} = \tilde{c}_j$.
3. Evaluate for this constraint set $\tilde{\Gamma}$ the corresponding mean field $\tilde{f}(\mathbf{x})$ using:

$$\tilde{f}(\mathbf{x}) = \langle \tilde{f}(\mathbf{x}) | \tilde{\Gamma} \rangle = \xi_i(\mathbf{x}) \xi_{ij}^{-1} \tilde{c}_j \quad (2.19)$$

4. Calculate the residual field of the random realization $\tilde{f}(\mathbf{x})$.

$$\tilde{F}(\mathbf{x}) = \tilde{f}(\mathbf{x}) - \tilde{f}(\mathbf{x}) \quad (2.20)$$

5. Now calculate the desired mean field $\bar{f}(\mathbf{x})$ subject to the desired set of constraints $\Gamma = c_j$ and add this to the calculated residual field $F(\mathbf{x})$.

$$f(\mathbf{x}) = \tilde{f}(\mathbf{x}) + \xi_i(\mathbf{x}) \xi_{ij}^{-1} (c_j - \tilde{c}_j) \quad (2.21)$$

The field $f(\mathbf{x})$ created according to this method obeys the set of imposed constraints.

2.2.1 Fourierspace

Bertschinger (1987) demonstrated already how generating a constrained realization is easily done in Fourier space. The expression found by Hoffman and Ribak can also be generated in Fourier space. The Fourier components for the individual entries of eq. 2.21 should be derived. (see van de Weygaert & Bertschinger (1996)). By assuming that the constraints are linear functionals of the field, they can be written as the convolutions of the field $f(\mathbf{x})$ and some kernel $H(\mathbf{x}; \mathbf{x}_i)$.

$$C_i[f; \mathbf{x}_i] = \int d\mathbf{x} H(\mathbf{x}; \mathbf{x}_i) f(\mathbf{x}) = c_i \quad (2.22)$$

The Fourier transform of the density field is defined to be:

$$f(\mathbf{x}) = \int \frac{d\mathbf{k}}{(2\pi)^3} \hat{f}(\mathbf{k}) e^{-i\mathbf{k}\cdot\mathbf{x}} \quad (2.23)$$

Defining the Fourier transform of the kernel as:

$$H(\mathbf{x}; \mathbf{x}_i) = \int \frac{d\mathbf{k}}{(2\pi)^3} \hat{H}_i(\mathbf{k}) e^{-i\mathbf{k}\cdot\mathbf{x}} \quad (2.24)$$

Because of the convolution theorem, the Fourier expression of the constraint function becomes:

$$C_i[f; \mathbf{x}_i] = \int \frac{d\mathbf{k}}{(2\pi)^3} \hat{H}_i(\mathbf{k}) \hat{f}^*(\mathbf{k}) = c_i \quad (2.25)$$

Having evaluated the constraint $C_i[f; \mathbf{x}_i]$, we can find the Fourier expressions for the constraint-constraint correlation function ξ_{ij} :

$$\xi_{ij} \equiv \langle C_i C_j \rangle \quad (2.26)$$

$$= \left\langle \int \frac{d\mathbf{k}_1}{(2\pi)^3} \hat{H}_i^*(\mathbf{k}_1) \hat{f}(\mathbf{k}_1) \int \frac{d\mathbf{k}_2}{(2\pi)^3} \hat{H}_j(\mathbf{k}_2) \hat{f}^*(\mathbf{k}_2) \right\rangle \quad (2.27)$$

$$= \int \int \frac{d\mathbf{k}_1}{(2\pi)^3} \frac{d\mathbf{k}_2}{(2\pi)^3} \hat{H}_i^*(\mathbf{k}_1) \hat{H}_j(\mathbf{k}_2) \langle \hat{f}(\mathbf{k}_1) \hat{f}^*(\mathbf{k}_2) \rangle \quad (2.28)$$

where we used the derived Fourier expression for the constraint function. Using the power spectrum definition of Bertschinger (1992) modified by a factor of $(2\pi)^3$ for Fourier convention:

$$(2\pi)^3 P(k) \delta_D(\mathbf{k}_1 - \mathbf{k}_2) = \langle \hat{f}(\mathbf{k}_1) \hat{f}^*(\mathbf{k}_2) \rangle \quad (2.29)$$

The Fourier integral expression for the constraint correlation function then becomes:

$$\xi_{ij} = \int \frac{d\mathbf{k}}{(2\pi)^3} \hat{H}_i^*(\mathbf{k}) \hat{H}_j(\mathbf{k}) P(k) \quad (2.30)$$

This quantifies the coupling between the different constraints in Fourier space, since some of these are correlated. The same calculation can be done for the constraint-field correlation function providing the expression:

$$\xi_i(\mathbf{x}) = \int \frac{d\mathbf{k}}{(2\pi)^3} \hat{H}_i(\mathbf{k}) P(k) e^{-i\mathbf{k}\cdot\mathbf{x}} \quad (2.31)$$

In all, this leads to the following expression for the constrained field:

$$f(\mathbf{x}) = \tilde{f}(\mathbf{x}) + \xi_i(\mathbf{x}) \xi_{ij}^{-1} (c_j - \tilde{c}_j) \quad (2.32)$$

$$= \int \frac{d\mathbf{k}}{(2\pi)^3} [\tilde{f}(\mathbf{k}) + P(k) \hat{H}_i(\mathbf{k}) \xi_{ij}^{-1} (c_j - \tilde{c}_j)] e^{i\mathbf{k}\cdot\mathbf{x}} \quad (2.33)$$

2.3 Applications of the Hoffman-Ribak Method

Generating a constrained realization using the Hoffman-Ribak method in Fourier space is evaluated on a three-dimensional grid with N grid points, where the Fourier transforms are replaced by discrete Fourier sums. The total costs of generating a constrained realization comes down to $\Theta[(M^2 + \log N)N]$. (van de Weygaert & Bertschinger, 1996) The most time consuming processes are the evaluation of the correlation functions ξ_{ij} and ξ_i , requiring the calculation of $M^2 + M$ Fourier integrals.

For certain applications of the Hoffman-Ribak method, the computational cost can be reduced. In order for this to happen, further restrictions have to be imposed on the convolution constraints. The first option is that the constraints are sampled of the same physical quantity at many different places. The advantage of this restriction is that for all constraints, the constraint-field correlation matrix can be evaluated from the same general correlation function. This then also holds for the constraint-constraint correlation function. The second requirement is that the grid points are evenly spaced. In this case, the kernels differ just by a phase factor.

These two additional restrictions make it possible to replace the discrete Fourier sums with Fast Fourier Transforms. The complete computational cost becomes $\Theta[N \log N]$.

Using the above restrictions, the Hoffman-Ribak method becomes an effective method for a large number of constraints, suitable for creating initial conditions for recreating large scale structure in a region of the universe. Ganon & Hoffman (1993) was one of the first to do this. More details of their research is found in chapter five. On a smaller scale, the Hoffman-Ribak method was used for specifying initial conditions for certain structures. A few of these applications are also mentioned in chapter five, but the constrained peak formalism by van de Weygaert & Bertschinger (1996) is explored here.

2.3.1 Constrained peak formalism

The constrained peak formalism is developed to generate a Gaussian random field subject to a number of peaks or dips. By imposing up to eighteen constraints per object on the local density field and the peculiar velocity or gravitational potential perturbation field, the matter distribution can be sculpted to influence the evolution as the user desires.

Scale and position: parameter values

A peak is defined as a local maximum in the density field, when filtered on appropriate scale. In this research, a Gaussian filter is used, which is important in the derivation of the constraint kernels \hat{H}_i in addition to defining the scale of the peak. The filtered density field in real space is defined as:

$$f_G(\mathbf{x}) = \int dy f(\mathbf{y}) W_G(\mathbf{x}, \mathbf{y}) \quad (2.34)$$

where W_G is the expression for the filter function. This leads to the following Fourier expression using the convolution theorem:

$$f_G(\mathbf{x}) = \int \frac{d\mathbf{k}}{(2\pi)^3} \hat{f}(\mathbf{k}) \hat{W}^*(\mathbf{k}) e^{-i\mathbf{k}\cdot\mathbf{x}} \quad (2.35)$$

where $W(\mathbf{k})$ is the expression for a Gaussian filter in Fourier space:

$$W(\mathbf{k}) = e^{-k^2 R_G^2/2} \quad (2.36)$$

with R_G defined as the smoothing scale. The scale of the peak is one of the parameters in this formalism and is an indication of the resulting structure after evolution. Besides the scale of the peak, the position x_d can be chosen freely. These three imposed position-coordinates can be merely seen as parameters appearing in the kernel $H(\mathbf{x}, \mathbf{x}_i)$ causing a phase shift $\mathbf{k} \cdot \mathbf{x}_d$.

For a peak or dip, up to eighteen constraints can be specified besides the scale and position of the peak. The first ten constraints will determine the density distribution of the immediate surroundings of the peak and therefore includes the density field and its derivatives. By finding the appropriate constraint functions, height, shape, compactness and orientation of the peak or dip can be determined. The specification of the gravitational field introduces eight other constraints in the form of the peculiar gravitational acceleration and the tidal force field, sculpting the remaining density distribution in the simulation box.

Constraints on the density field

The density field around a peak at a position \mathbf{x}_d can be locally described by the second-order Taylor expansion of the density contrast profile around the peak.

$$f_G(\mathbf{x}) = f_G(\mathbf{x}_d) + \nabla \cdot f_G(\mathbf{x}_d) + \frac{1}{2} \sum_{i,j=1}^3 \frac{\partial^2 f_G}{\partial x_i \partial x_j}(\mathbf{x}_d) (x_i - x_{d,i})(x_j - x_{d,j}) \quad (2.37)$$

The requirement that the smoothed density field has a maximum of a certain height, shape, compactness and orientation translates into constraints on the values of the smoothed density field $f_G(\mathbf{x})$ at \mathbf{x}_d , the gradient $\nabla \cdot f_G(\mathbf{x}_d)$ and on the second derivative tensor $\nabla_i \nabla_j f_G(\mathbf{x}_d)$. Note that when a certain constraint is imposed, the constraint function has to be equal to the imposed value:

$$C_i[f; \mathbf{x}_i] = \int \frac{d\mathbf{k}}{(2\pi)^3} \hat{H}_i(\mathbf{k}) \hat{f}^*(\mathbf{k}) = c_i \quad (2.38)$$

First constraint is the height of the peak $f_G(\mathbf{x}_d)$. This is usually expressed in units of the variance $\sigma_0 = \langle f_G f_G \rangle^{1/2}$.

$$f_G(\mathbf{x}_d) = \nu_c \sigma_0 (R_G) \quad (2.39)$$

where ν_c can be chosen freely and therefore imposed. Combining eq. 2.39 and eq. 2.35, the constraint function can be rewritten to:

$$\int \frac{d\mathbf{k}}{(2\pi)^3} \hat{f}(\mathbf{k}) \hat{W}^*(\mathbf{k}) e^{-i\mathbf{k}\cdot\mathbf{x}_d} = \nu_c \sigma_0 (R_G) \quad (2.40)$$

The corresponding constraint kernel $\hat{H}_j(\mathbf{k})$ and the constraint value c_j are recognized, when comparing the derived formula with the definition for the constraint formula (eq. 2.38):

$$\hat{H}_i(\mathbf{k}) = \hat{W}(\mathbf{k})e^{i\mathbf{k}\cdot\mathbf{x}_d} \quad c_i = \nu_c\sigma_0(R_G) \quad (2.41)$$

The second set of constraints applies to the first-order derivatives of the density field at position \mathbf{x}_d . To ensure that the peak is a local maximum, the divergence of the density field should be equal to zero. The Fourier expression for the gradient is defined as:

$$\frac{\partial f_G}{\partial x_i} = \frac{\partial}{\partial x_i} \int \frac{d\mathbf{k}}{(2\pi)^3} \hat{f}(\mathbf{k})\hat{W}^*(\mathbf{k})e^{-i\mathbf{k}\cdot\mathbf{x}_d} \quad (2.42)$$

In which $i = 1, 2, 3$ represent the three directions. The combined set of the three constraint expressions then yields:

$$\int \frac{d\mathbf{k}}{(2\pi)^3} -i\mathbf{k}\hat{f}(\mathbf{k})\hat{W}^*(\mathbf{k})e^{-i\mathbf{k}\cdot\mathbf{x}_d} = 0 \quad (2.43)$$

Again, the kernel $\hat{H}(\mathbf{k})_j$ and the numerical value of c_j can be easily recognized in the above formula.

$$\hat{H}_j(\mathbf{k}) = ik_l\hat{W}(\mathbf{k})e^{i\mathbf{k}\cdot\mathbf{x}_d} \quad c_j = 0 \quad (2.44)$$

for $j = 2, 3, 4$ and $l = j - 1$.

The last set of constraints corresponds to the shape, compactness and orientation of the density field around the position of the peak. The density field subject to a peak can be seen to be ellipsoidal (see quadratic term in eq.2.37) by using a change of coordinate system \mathbf{x}' where the axes are aligned with the eigenvectors of $\nabla_i \nabla_j f_G$ with $-\lambda_1, -\lambda_2$ and $-\lambda_3$ the eigenvalues. The density field in this coordinate system can be described as:

$$f_G(\mathbf{x}') = f_G(\mathbf{x}_d) - \frac{1}{2} \sum_{i=1}^3 \lambda_i x_i'^2 \quad (2.45)$$

The shape of an ellipsoid is completely specified by the two axial ratios $a_{12} \equiv a_1/a_2$ and $a_{13} \equiv a_1/a_3$. The suggested coordinate system transformation has the advantage that imposing constraints on the axial ratios and therefore the shape, results in imposing constraints on the ratios of eigenvalues:

$$\left(\frac{\lambda_2}{\lambda_1}\right) = a_{12}^2 \quad \left(\frac{\lambda_3}{\lambda_1}\right) = a_{13}^2 \quad (2.46)$$

The magnitude of the eigenvalues depend on the steepness of the density profile at the peak, which is specified by the Laplacian $\nabla^2 f_G$. The steepness is usually expressed in terms of $\sigma_2(R_G) = \langle \nabla^2 f_G \nabla^2 f_G \rangle^{1/2}$, which creates the expression for the constraint:

$$\nabla^2 f_G = -x_d \sigma_2(R_G) = - \sum_{i=1}^3 \lambda_i \quad (2.47)$$

where the minus sign insures x_d to be positive in the case of a peak. The eigenvalue λ_1 can then found to be:

$$\lambda_1 = \frac{x_d \sigma_2(R_G)}{1 + a_{12}^2 + a_{13}^2} \quad (2.48)$$

where λ_2 and λ_3 are multiplications of λ_1 with a_{12}^2 and a_{13}^2 respectively. The orientation of the peak in coordinate system \mathbf{x}' with respect to the simulation box axes is specified by the three Euler angles α , β and φ . An illustration of the angles can be seen in figure 2.4.

It can be represented by the corresponding transformation matrix A_{ij} , which

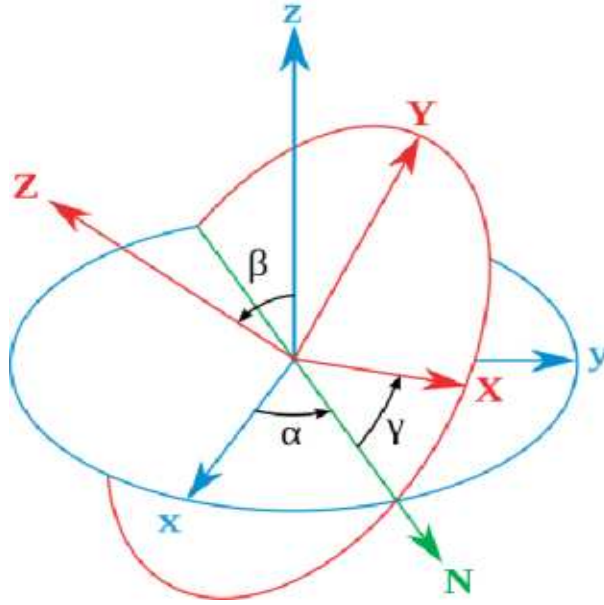


Figure 2.4: The Euler angles α , β and φ .

is given by:

$$\mathbf{A} = \begin{pmatrix} \cos \alpha \cos \varphi - \cos \beta \sin \alpha \sin \varphi & \sin \alpha \cos \varphi + \cos \beta \cos \alpha \sin \varphi & \sin \beta \sin \varphi \\ -\cos \alpha \sin \varphi - \cos \beta \sin \alpha \cos \varphi & -\sin \alpha \sin \varphi + \cos \beta \cos \alpha \cos \varphi & -\sin \beta \cos \varphi \\ \sin \beta \sin \alpha & -\sin \beta \cos \alpha & \cos \beta \end{pmatrix}$$

This means that the change of coordinate system can be represented as:

$$x'_i = \sum_{j=1}^3 A_{ij}(x_j - x_{j,d}) \quad j = 2, 3, 4 \quad (2.49)$$

where $x_{j,d}$ is the position of the peak in coordinate system \mathbf{x} . Thus, $x_i'^2$ will transform according to:

$$x_i'^2 = \sum_{j=1}^3 \sum_{k=1}^3 A_{ij} A_{ik} (x_j - x_{j,d})(x_k - x_{k,d}) \quad (2.50)$$

Combining the transformation of $x_i'^2$ and the description of the density field (eq. 2.45), the full expression for the density field in the coordinate system \mathbf{x} can be derived:

$$f_G(\mathbf{x}) = f(\mathbf{x}_d) - \frac{1}{2} \sum_{j,k=1}^3 \left(\sum_{i=1}^3 \lambda_i A_{ij} A_{ik} \right) (x_j - x_{j,d})(x_k - x_{k,d}) \quad (2.51)$$

The set of second derivatives of the density field can be recognized, when comparing eq. 2.51 and eq. 2.37:

$$\frac{\partial^2 f_G}{\partial x_i \partial x_j} = - \sum_{i=1}^3 \lambda_i A_{ij} A_{ik} \quad (2.52)$$

The Fourier expression for the Laplacian of the density field must be obtained in order to find the expression of the kernel \hat{H}_j to be:

$$H_j(\mathbf{k}) = -k_i k_l \hat{W}(\mathbf{k}) e^{i\mathbf{k} \cdot \mathbf{x}_d} \quad c_j = - \sum_{k=1}^3 \lambda_k A_{ki} A_{kl} \quad (2.53)$$

where $j = 5, \dots, 10$ and $i, l = 1, \dots, 3$.

Constraints on the gravitational field

When a patch of matter evolves, its shape and density distribution will change. The path followed by the patch and the shape are defined by the forces it experiences and the density changes due to expansion or compression. This means that the dynamics of the matter distribution are described by the gravitational potential field. Including the derivatives of the gravitational potential perturbation field $\phi(\mathbf{x})$ in the choice of constraints allows the dynamics to be sculpted. But in the linear evolution regime and for a growing mode solution, the divergence of the potential perturbation field, the peculiar gravitational acceleration $\mathbf{g}(\mathbf{x})$ is proportional to the peculiar velocity $\mathbf{v}(\mathbf{x})$ (Peebles, 1980),

$$\mathbf{v}(\mathbf{x}, t) = \frac{2}{3} \frac{f(\Omega)}{H\Omega} \mathbf{g}(\mathbf{x}, t) \quad (2.54)$$

where $f(\Omega)$ is defined as the dimensionless linear growth factor and approximated by Peebles to $\Omega^{0.6}$. (Peebles, 1980) The peculiar velocity at a specific position \mathbf{x}_d can be described by a Taylor expansion where the velocity deformation tensor, consists of three modes:

$$v_{G,i}(\mathbf{x}) = v_G(\mathbf{x}_d) + a \sum_{j=1}^3 \left[\frac{1}{3a} (\nabla \cdot \mathbf{v}_G)(\mathbf{x}_d) \delta_{ij} + \sigma_{ij}(\mathbf{x}_d) + w_{ij}(\mathbf{x}_d) \right] (x_j - x_{d,j}) \quad (2.55)$$

where σ_{ij} is defined as the shear and can be described by the trace-free symmetric part of $\partial v_{G,i} / \partial r_j$:

$$\sigma_{ij} = \frac{1}{2a} \left[\frac{\partial v_{G,i}}{\partial x_j} + \frac{\partial v_{G,j}}{\partial x_i} \right] - \frac{1}{3a} (\nabla \cdot \mathbf{v}_G) \delta_{ij} \quad (2.56)$$

In the linear regime the shear elements σ_{ij} are proportional to the tidal tensor components E_{ij} . The vorticity w_{ij} is described by the anti-symmetric part of this tensor:

$$w_{ij} = \frac{1}{2a} \left[\frac{\partial v_{G,i}}{\partial x_j} - \frac{\partial v_{G,j}}{\partial x_i} \right] \quad (2.57)$$

Since vorticity will not grow in the linear regime, it will be further discarded. The trace of the velocity field gradient represent the deformation of the peak and is the only component responsible for a change in density. Note that constraining the peculiar velocity gradient is equal to imposing a constraint on the density field, since the two are coupled via the continuity equation:

$$\frac{\nabla \cdot \mathbf{v}}{a} = Hf(\Omega)f_G(\mathbf{x}) \quad (2.58)$$

From this relationship we can infer the relation between the Fourier components of the smoothed velocity field $\hat{v}_{G,i}$ and the Fourier components of the density field \hat{f}_G .

$$\hat{v}_G = -f(\Omega)Ha \frac{ik_i}{k^2} \hat{f}(\mathbf{k}) \hat{W}^*(\mathbf{k}) \quad (2.59)$$

This relationship will be used to obtain expressions for the constraint functions of the peculiar velocity and the tidal tensor.

The first three constraints concern the peculiar velocity at the position of the peak itself, $\mathbf{v}(\mathbf{x}_d)$. It is useful to specify the constraints in units of the variance of the peculiar velocity of the peak, $\sigma_{v,pk}(R_G) = \langle v_{G,pk} v_{G,pk} \rangle$. The constraint expression becomes:

$$v_{G,i}(\mathbf{x}_d) = \bar{v}_i \sigma_{v,pk}(R_G) \quad (2.60)$$

where $i = 1, 2, 3$ represents the three directions. The variance of the velocity of the peak is less than the overall dispersion of the velocity of the field because of the gravitational pull of the peak itself. The two variances are related by:

$$\sigma_{v,pk}(R_G) = \sigma_v(R_G) \sqrt{1 - \gamma_v^2} \quad \gamma_v \equiv \frac{\sigma_0^2}{\sigma_{-1}\sigma_1} \quad (2.61)$$

where the dispersion of the velocity of the field is defined as:

$$\sigma_v(R_G) = f(\Omega)H\sigma_{-1}(R_G) \quad (2.62)$$

with $\sigma_j(R_G)$ being the spectral moments:

$$\sigma_j^2(R_G) \equiv \int \frac{d\mathbf{k}}{(2\pi)^3} P(\mathbf{k}) \hat{W}(\mathbf{k}) k^{2j} \quad (2.63)$$

The peculiar velocity at position \mathbf{x}_d is defined as:

$$v_{G,i}(\mathbf{x}_d) = \int \frac{d\mathbf{k}}{(2\pi)^3} \hat{v}_G(\mathbf{k}) \hat{W}^* e^{-i\mathbf{k} \cdot \mathbf{x}_d} \quad (2.64)$$

Using the relation between the Fourier components of the density and peculiar velocity field (eq. 2.59) and the derived expression for the numerical constraint, the constraint function can be derived:

$$\int \frac{d\mathbf{k}}{(2\pi)^3} \hat{f}_G(\mathbf{k}) \left(-Hf(\Omega)a \frac{ik_i}{k^2} \hat{W}^*(\mathbf{k}) \right) e^{-i\mathbf{k} \cdot \mathbf{x}_d} = \bar{v}_i f(\Omega)Ha\sigma_{-1}(R_G) \sqrt{1 - \gamma_v^2} \quad (2.65)$$

The corresponding kernels and constraints can be found to be:

$$\hat{H}_j(\mathbf{k}) = Hf(\Omega)a\frac{ik_j}{k^2}\hat{W}(\mathbf{k})e^{-i\mathbf{k}\cdot\mathbf{x}_d} \quad c_j = \bar{v}_i af(\Omega)H\sigma_{-1}(R_G)\sqrt{1-\gamma_v^2} \quad (2.66)$$

Because the tidal tensor E_{ij} is trace-less, which means that $\sum \varepsilon_k = 0$, only two eigenvalues need to be specified independently. In combination with the orientation of the shear, five additional constraints are needed to characterize the tidal field sculpting the density field. They quantify the deformation of the patch of matter. It is most practical expressed in terms of the eigenvectors and eigenvalues:

$$E_{G,ij} = \frac{1}{a} \left(\nabla \cdot \mathbf{v} - \frac{1}{3} \nabla^2 \mathbf{v} \delta_{ij} \right) = \sum_{k=1}^3 \varepsilon_k T_{ki} T_{kj} \quad (2.67)$$

where the elements of T are the components of the various eigenvectors of the tidal tensor, whose angles are defined by the Euler angles α_E , β_E and φ_E . In constrained theory there is a strong correlation present between the tidal tensor and the Laplacian of the density field, which depicts in the tendency of the tidal force field to align with the principal axes of the ellipsoid in the one-peak formalism. It is therefore convenient to express the elements of the tidal force field with respect to the reference system defined by the axes of the peak:

$$T_{ki} = \sum_{m=1}^3 \tilde{T}_{km} A_{mi} \quad (2.68)$$

where A is the transformation matrix for the principal axes with respect to the standard reference frame. The eigenvalues of the tidal tensor, ε_1 , ε_2 and ε_3 , specify the magnitude of the tidal field. They determine the morphology of the structure that is to evolve.

Structure	$\varepsilon_1 > 0$	$\varepsilon_2 > 0$	$\varepsilon_3 > 0$
Peak	$\varepsilon_1 > 0$	$\varepsilon_2 > 0$	$\varepsilon_3 > 0$
Filament	$\varepsilon_1 > 0$	$\varepsilon_2 > 0$	$\varepsilon_3 < 0$
Wall	$\varepsilon_1 > 0$	$\varepsilon_2 < 0$	$\varepsilon_3 < 0$
Void	$\varepsilon_1 < 0$	$\varepsilon_2 < 0$	$\varepsilon_3 < 0$

The eigenvalues of the tidal tensor are usually specified in units of the dispersion of the off-diagonal elements of the tidal tensor $E_{G,ij}$

$$\sigma_E(R_G) = Hf(\Omega)\sigma_0(R_G)\sqrt{\frac{1-\gamma^2}{15}} \quad \gamma \equiv \frac{\sigma_1^2}{\sigma_0\sigma_2} \quad (2.69)$$

The Fourier components $\hat{E}_{G,ij}$ of the tidal tensor can be found to be:

$$\hat{E}_{G,ij} = f(\Omega)H \left(\frac{k_i k_j}{k^2} - \frac{1}{3} \delta_{ij} \right) \hat{W}^*(\mathbf{k}) \hat{f}(\mathbf{k}) \quad (2.70)$$

The constraint expression therefore becomes:

$$\int \frac{d\mathbf{k}}{(2\pi)^3} \left(f(\Omega) H \left(\frac{k_i k_j}{k^2} - \frac{1}{3} \delta_{ij} \right) \hat{W}^*(\mathbf{k}) \right) \hat{f}(\mathbf{k}) e^{-i\mathbf{k} \cdot \mathbf{x}_d} = \varepsilon_i \sigma_E \quad (2.71)$$

in which the kernel and the constraints can be recognized.

Note that when the density and velocity perturbations are in the order of unity, the linear regime breaks down and the peculiar velocity and peculiar gravitational acceleration will no longer be proportional to each other. In order to prevail this problem, the constraints can be imposed on the peculiar gravitational potential field, which evolves linearly for a longer time. The same expressions for the constraints and the constraint kernels will then be found, up to a proportionality constant.

2.4 Constraint probability

To assess the likelihood of a set of imposed constraints, the χ^2 can be calculated. This is defined as:

$$\chi^2 = \sum_{i,j=1}^M C_i (Q^{-1}) C_j = c_i \xi_{ij}^{-1} c_j \quad (2.72)$$

where M is the number of constraints. The constraint set can be considered likely when the χ^2 per degree of freedom, $\bar{\chi}^2 = \chi^2/M$, is in the order of unity.

In the case of the full eighteen constraints on a peak, we can find the χ^2 in the following matter. The density and gravity field around an arbitrary point \mathbf{x}_d in a Gaussian random field can now be characterized by the following eighteen constraints, combined in the parameter set Υ .

$$\Upsilon = (f, \eta_1, \eta_2, \eta_3, \zeta_1, \zeta_2, \zeta_3, \zeta_4, \zeta_5, \zeta_6, v_1, v_2, v_3, E_1, E_2, E_4, E_5, E_6) \quad (2.73)$$

where f is the value of the field at \mathbf{x}_d , the divergence of the field is denoted by η_i , and ζ_A are the six independent components of the Laplacian of the density field, with $A = 1, 2, 3, 4, 5, 6$ referring to the six components $ij = 11, 22, 33, 12, 13, 23$ of the tensor. The gravitational potential field is defined by the peculiar velocity v_i , while the five independent components of the tidal tensor are denoted by E_A with $A = 11, 22, 12, 13, 23$ referring to the $ij = 11, 22, 12, 13, 23$ components.

The joint probability distribution function of these eighteen parameters can be found by calculating the corresponding correlation matrix $\mathbf{Q} = \langle \mathbf{C} \mathbf{C}^t \rangle$. The entries of the constraint-constraint correlation matrix were analytically derived, which is possible due to the restriction that the constraints are linear functionals of the field itself. In this case the definition for the power spectrum by Bertschinger (1992) can be used. A few of the derivations will be presented here.

The first entry of the matrix is the correlation between the field at a certain position and itself.

$$\xi_{11} = \langle C_1 C_1 \rangle$$

$$\begin{aligned}
&= \langle f_G(\mathbf{x})f_G(\mathbf{x}) \rangle \\
&= \left\langle \int \frac{d\mathbf{k}_1}{(2\pi)^3} \hat{f}(\mathbf{k}_1) \hat{W}(\mathbf{k}_1) e^{-i\mathbf{k}_1 \cdot \mathbf{x}} \int \frac{d\mathbf{k}_2}{(2\pi)^3} \hat{f}^*(\mathbf{k}_2) \hat{W}^*(\mathbf{k}_2) e^{i\mathbf{k}_2 \cdot \mathbf{x}} \right\rangle \\
&= \int \frac{d\mathbf{k}_1}{(2\pi)^3} \int \frac{d\mathbf{k}_2}{(2\pi)^3} \hat{W}(\mathbf{k}_1) \hat{W}^*(\mathbf{k}_2) e^{-i\mathbf{k}_1 \cdot \mathbf{x}} e^{i\mathbf{k}_2 \cdot \mathbf{x}} \langle \hat{f}(\mathbf{k}_1) \hat{f}^*(\mathbf{k}_2) \rangle \\
&= \int \frac{d\mathbf{k}_1}{(2\pi)^3} \int \frac{d\mathbf{k}_2}{(2\pi)^3} \hat{W}(\mathbf{k}_1) \hat{W}^*(\mathbf{k}_2) e^{-i(\mathbf{k}_1 - \mathbf{k}_2) \cdot \mathbf{x}} (2\pi)^3 \delta_D(\mathbf{k}_1 - \mathbf{k}_2) P(k) \\
&= \int \frac{d\mathbf{k}}{(2\pi)^3} \hat{W}^2(\mathbf{k}) P(k)
\end{aligned}$$

Note that by comparing the derived expression for the constraint-constraint correlation function with the definition of the spectral moments (see eq. 2.63), the entry of the correlation is equal to σ^2 . This derivation is just a mathematical example since the two same situations always correlate with each other.

Another entry in the correlation matrix is the correlation between the density field and the set of its second derivatives $\nabla_i \nabla_j f$. In this calculation, six entries of the constraint-constraint correlation matrix are derived at once.

$$\begin{aligned}
\xi_{1m} &= \langle C_1 C_m \rangle \quad m = 5, 6, 7, 8, 9, 10 \\
&= \langle f_G(\mathbf{x}) \frac{\partial^2 f_G(\mathbf{x})}{\partial x_i \partial x_j} \rangle \\
&= \left\langle \int \frac{d\mathbf{k}_1}{(2\pi)^3} \hat{f}(\mathbf{k}_1) \hat{W}(\mathbf{k}_1) e^{-i\mathbf{k}_1 \cdot \mathbf{x}} \int \frac{d\mathbf{k}_2}{(2\pi)^3} \hat{f}^*(\mathbf{k}_2) \hat{W}^*(\mathbf{k}_2) i k_{2i} i k_{2j} e^{i\mathbf{k}_2 \cdot \mathbf{x}} \right\rangle \\
&= \int \frac{d\mathbf{k}_1}{(2\pi)^3} \frac{d\mathbf{k}_2}{(2\pi)^3} i k_{2i} i k_{2j} \hat{W}(\mathbf{k}_1) \hat{W}^*(\mathbf{k}_2) e^{-i(\mathbf{k}_1 - \mathbf{k}_2) \cdot \mathbf{x}} \langle \hat{f}(\mathbf{k}_1) \hat{f}^*(\mathbf{k}_2) \rangle \\
&= \int \frac{d\mathbf{k}_1}{(2\pi)^3} \frac{d\mathbf{k}_2}{(2\pi)^3} -k_{2i} k_{2j} \hat{W}(\mathbf{k}_1) \hat{W}^*(\mathbf{k}_2) e^{-i(\mathbf{k}_1 - \mathbf{k}_2) \cdot \mathbf{x}} (2\pi)^3 \delta_D(\mathbf{k}_1 - \mathbf{k}_2) P(k) \\
&= - \int \frac{d\mathbf{k}}{(2\pi)^3} k_j k_i \hat{W}^2(\mathbf{k}) P(k)
\end{aligned}$$

Again comparing with the equation for spectral moments it is found that for $i = j$, this is equal to σ_1^2 , and zero when $i \neq j$. This means that there is a negative correlation between the density field and the Laplacian of the density field. Note that this value is a total for the complete Laplacian.

As an example two constraints that have no influence on each other whatsoever, the correlation function between the first derivatives and the second derivatives of the density field are calculated.

$$\begin{aligned}
\xi_{lm} &= \langle C_l C_m \rangle \quad l = 2, 3, 4; m = 5, 6, 7, 8, 9, 10 \\
&= \left\langle \frac{\partial f_G(\mathbf{x})}{\partial x_i} \frac{\partial^2 f_G(\mathbf{x})}{\partial x_j \partial x_k} \right\rangle \\
&= \left\langle \int \frac{d\mathbf{k}_1}{(2\pi)^3} k_{1i} \hat{f}(\mathbf{k}_1) \hat{W}(\mathbf{k}_1) e^{-i\mathbf{k}_1 \cdot \mathbf{x}} \int \frac{d\mathbf{k}_2}{(2\pi)^3} \hat{f}^*(\mathbf{k}_2) \hat{W}^*(\mathbf{k}_2) i k_{2j} i k_{2k} e^{i\mathbf{k}_2 \cdot \mathbf{x}} \right\rangle \\
&= \int \frac{d\mathbf{k}_1}{(2\pi)^3} \frac{d\mathbf{k}_2}{(2\pi)^3} k_{1i} i k_{2j} i k_{2k} \hat{W}(\mathbf{k}_1) \hat{W}^*(\mathbf{k}_2) e^{-i(\mathbf{k}_1 - \mathbf{k}_2) \cdot \mathbf{x}} \langle \hat{f}(\mathbf{k}_1) \hat{f}^*(\mathbf{k}_2) \rangle \\
&= \int \frac{d\mathbf{k}_1}{(2\pi)^3} \frac{d\mathbf{k}_2}{(2\pi)^3} -k_{1i} k_{2j} k_{2k} \hat{W}(\mathbf{k}_1) \hat{W}^*(\mathbf{k}_2) e^{-i(\mathbf{k}_1 - \mathbf{k}_2) \cdot \mathbf{x}} (2\pi)^3 \delta_D(\mathbf{k}_1 - \mathbf{k}_2) P(k)
\end{aligned}$$

$$= - \int \frac{d\mathbf{k}}{(2\pi)^3} -k_i k_j k_k \hat{W}^2(\mathbf{k}) P(k)$$

By comparing the last equation to the definition of spectral moments, it shows that this will always be equal zero, since there is an odd number of wave numbers present.

The constraint correlation function can also be calculated for the divergence of the gravitational potential field, or in the linear regime, the peculiar velocity field. Here the between the various components of the peculiar velocity field is derived.

$$\begin{aligned} \xi_{lm} &= \langle C_l C_m \rangle \quad l, m = 11, 12, 13 \\ &= \langle v_{G,i}(\mathbf{x}) v_{G,j}(\mathbf{x}) \rangle \\ &= \left\langle \int \frac{d\mathbf{k}_1}{(2\pi)^3} \hat{v}_i(\mathbf{k}_1) \hat{W}(\mathbf{k}_1) e^{-i\mathbf{k}_1 \cdot \mathbf{x}} \int \frac{d\mathbf{k}_2}{(2\pi)^3} \hat{v}_j^*(\mathbf{k}_2) \hat{W}^*(\mathbf{k}_2) e^{i\mathbf{k}_2 \cdot \mathbf{x}} \right\rangle \\ &= \left\langle \int \frac{d\mathbf{k}_1}{(2\pi)^3} -f(\Omega) H a \frac{ik_{1,i}}{k^2} \hat{f}(\mathbf{k}_1) \hat{W}(\mathbf{k}_1) e^{-i\mathbf{k}_1 \cdot \mathbf{x}} \int \frac{d\mathbf{k}_2}{(2\pi)^3} -f(\Omega) H a \frac{ik_{2,j}}{k^2} \hat{f}^*(\mathbf{k}_2) \hat{W}^*(\mathbf{k}_2) e^{i\mathbf{k}_2 \cdot \mathbf{x}} \right\rangle \\ &= \int \frac{d\mathbf{k}_1}{(2\pi)^3} \int \frac{d\mathbf{k}_2}{(2\pi)^3} f(\Omega)^2 H^2 a^2 \frac{-k_{1,i} k_{2,j}}{k^4} \hat{W}(\mathbf{k}_1) \hat{W}^*(\mathbf{k}_2) e^{-i(\mathbf{k}_1 - \mathbf{k}_2) \cdot \mathbf{x}} \langle \hat{f}(\mathbf{k}_1) \hat{f}^*(\mathbf{k}_2) \rangle \\ &= \int \frac{d\mathbf{k}_1}{(2\pi)^3} \int \frac{d\mathbf{k}_2}{(2\pi)^3} f(\Omega)^2 H^2 a^2 \frac{-k_{1,i} k_{2,j}}{k^4} \hat{W}(\mathbf{k}_1) \hat{W}^*(\mathbf{k}_2) e^{-i(\mathbf{k}_1 - \mathbf{k}_2) \cdot \mathbf{x}} (2\pi)^3 \delta_D(\mathbf{k}_1 - \mathbf{k}_2) \\ &= \int \frac{d\mathbf{k}}{(2\pi)^3} f(\Omega)^2 H^2 a^2 \frac{-k_i k_j}{k^4} \hat{W}^2(\mathbf{k}) P(k) \end{aligned}$$

This has a value for $i = j$ equal to $-f^2(\Omega) H^2 a^2 \sigma_{-1}^2$ but not for $i \neq j$. This means that there is a correlation between a velocity in a certain direction and itself, but there is no correlation between the velocities in the different directions.

The complete constraint-constraint correlation matrix is found in figure 2.7.

An insightful expression can be found by reducing this 18×18 matrix into nine 2×2 matrices by transferring the set of variables $\zeta_1, \zeta_2, \zeta_3, E_1, E_2$ into a new set x, y, z, E_y, E_z :

$$x = -\frac{\zeta_1 + \zeta_2 + \zeta_3}{\sigma_2} \quad y = -\frac{\zeta_1 - \zeta_3}{2\sigma_2} \quad z = -\frac{\zeta_1 - 2\zeta_2 + \zeta_3}{2\sigma_2} \quad (2.74)$$

$$E_y = \frac{E_1 - E_3}{2} \quad E_z = \frac{E_1 - 2E_2 + E_3}{2} \quad (2.75)$$

The constraint-constraint correlation matrix changes accordingly and can be found in figure 2.8.

The joint probability distribution function for the set of constraints Υ can be defined as:

$$P[\Upsilon] = A e^{-Q/2} dv d^3 \eta dx dy dz d\zeta_4 d\zeta_5 d\zeta_6 d^3 \mathbf{v} dE_y dE_z dE_4 dE_5 dE_6 \quad (2.76)$$

where the normalization constant A is given by:

$$A = \frac{3^6 5^5}{1024 \pi^9 (1 - \gamma^2)^3 (1 - \gamma_v^2)^{3/2} (f(\Omega) H)^4 \sigma_{-1}^3 \sigma_0 \sigma_1^3 \sigma_2^3} \quad (2.77)$$

and

$$Q = \sum_{i,j=1}^{18} C_i(Q^{-1})_{ij}C_j \quad (2.78)$$

$$= \nu^2 + \frac{(x - x_*)^2}{1 - \gamma^2} + 15y^2 + 5z^2 + \frac{3\eta \cdot \eta}{\sigma_1^2} + \sum_{A=4}^6 \frac{15\zeta_A^2}{\sigma_2^2} + \frac{3(\mathbf{v} - \mathbf{v}_*)^2}{\tilde{\sigma}_v^2} \quad (2.79)$$

$$+ \frac{(E_y - E_y^*)^2}{\sigma_E^2} + \frac{(E_z - E_z^*)^2}{3\sigma_E^2} + \sum_{A=4}^6 \frac{(E_A - E_A^*)^2}{\sigma_E^2} \quad (2.80)$$

where $\tilde{\sigma}_v$ and σ_E are defined as:

$$\tilde{\sigma}_v \equiv f(\Omega)Ha\sigma_{-1}\sqrt{1 - \gamma_v^2} \quad \sigma_E \equiv f(\Omega)H\sigma_0\sqrt{\frac{1 - \gamma^2}{15}} \quad (2.81)$$

while the various coupling quantities are defined:

$$x_* = \gamma\nu \quad (2.82)$$

$$\mathbf{v}_* = \gamma_v f(\Omega)H \frac{\sigma_{-1}}{\sigma_1} \eta \quad (2.83)$$

$$E_y^* = \gamma y f(\Omega)H\sigma_0 \quad (2.84)$$

$$E_z^* = \gamma z f(\Omega)H\sigma_0 \quad (2.85)$$

$$E_A^* = \gamma f(\Omega)H \frac{\sigma_0}{\sigma_2} \zeta_A \quad A = 4, 5, 6 \quad (2.86)$$

Note in the above description of the correlation matrix, the correlations between the different constraints become very clear, since there are cross terms present.

Extensions of the HR-method

Constrained realizations can be used to study noisy and incomplete data. When a region of the universe is obscured due to, for example, the Galactic plane, the surrounding region can be reconstructed in order to gain insight in the structure in the zone of avoidance.

Count-in-cells of IRAS galaxies shows that on large angular scales the distribution is Gaussian and that for example the Hoffman-Ribak method can be used to create constrained Gaussian initial conditions to re simulate the large scale distribution. But on small angular scales, the distribution appears to be non-Gaussian. (Coles & Jones, 1991) The distribution of the galaxies appears to come from a underlying lognormal distribution. This is defined as transforming a Gaussian field $f(\mathbf{x})$ via:

$$f_{LN}(\mathbf{x}) = e^{f(\mathbf{x})} \quad (2.87)$$

Mathematically it can be derived from the Euler equation, which in the linear regime is given by:

$$\frac{\partial f}{\partial t} + f \nabla \cdot \mathbf{v} \propto 0 \quad (2.88)$$

$$\frac{1}{f} \frac{\partial f}{\partial t} \propto \nabla \cdot \mathbf{v} \quad (2.89)$$

$$\partial \ln f \propto \nabla \cdot \mathbf{v} \quad (2.90)$$

This indicates a lognormal distribution for the density field. The probability distribution of a Gaussian random unconstrained field is in this case given by:

$$P_{LN}(f(\mathbf{x}_1), \dots, f(\mathbf{x}_N))df(\mathbf{x}_1), \dots, df(\mathbf{x}_N) = \frac{1}{[(2\pi)^N \det(M)]^{1/2}} e^{-A} df(\mathbf{x}_1), \dots, df(\mathbf{x}_N) \quad (2.91)$$

with A defined as:

$$A \equiv \frac{1}{2} \sum_{i=1}^N \sum_{j=1}^N \ln f(\mathbf{x}_i) K_{ij} \ln f(\mathbf{x}_j) \quad (2.92)$$

where K is the inverse matrix of the correlation matrix. The probability distribution of the set of constraints, which are also lognormal distributed, is equal to:

$$P_{LN}(C_1, C_2, \dots, C_M) dC_1, dC_2, \dots, dC_M = \frac{1}{[(2\pi)^M \det(Q)]^{1/2}} e^{-B} dC_1, \dots, dC_M \quad (2.93)$$

with

$$B \equiv \frac{1}{2} \sum_{i=1}^M \sum_{j=1}^M \ln C_i (Q^{-1})_{ij} \ln C_j \quad (2.94)$$

where Q is the constraint correlation matrix is (see eq.2.13 for the definition). Using the vector notation for the field f and the set of constraints Γ and the notation of eq.2.7 for the probability distribution function, the conditional probability distribution function can be written as:

$$P_{LN}(f | \Gamma) = \frac{P_{LN}(f)}{P_{LN}(\Gamma)} \quad (2.95)$$

$$= e^{-\frac{1}{2}(\ln \mathbf{f}^t K \ln \mathbf{f} - \ln \mathbf{C}^t Q^{-1} \ln \mathbf{C})} \frac{D[f]}{D[\Gamma]} \quad (2.96)$$

When f and c_j are Gaussian distributed, the conditional probability distribution function of the constrained field is a shifted Gaussian around the mean field. The same can be seen when the two distributions are lognormal: the conditional probability distribution function is that of shifted lognormal distribution. This means that every composition of $f(\mathbf{x})$ subject to the same set of constraints will have a lognormal distribution. The residual field is such a composition and will therefore have a lognormal distribution. Since the variance of the probability distribution function is no longer independent of the chosen numerical values for the constraints, the Hoffman-Ribak method can no longer be used to construct constrained realizations of lognormal fields.

But since the lognormal field is easily related to the underlying Gaussian density field, a simple transition was thought of by Sheth (1995). A new field should be defined such that $E \equiv \ln(f_{LN})$. The conditional probability distribution function for this field becomes again the shifted Gaussian function and the Hoffman-Ribak method can be used again.

2.4.1 Change of coordinate system.

When constructing a realization of a random density field in the neighborhood of a peak with a specific interest in gravitational and tidal forces, a change of

coordinate system is desired. Binney & Quinn (1991) formulated an description for the density field in spherical harmonics:

$$f(\mathbf{x}) = \sqrt{\frac{2}{\pi}} \sum_{lmn} f_{lm}(k_n r) \kappa_n j_l(k_n r) Y_l^m(\theta, \phi) \quad (2.97)$$

Since this description contains the eigenfunctions of the angular momentum operator, constraints on the angular momentum can be easily imposed. For e.g the study of angular momentum, we know its is far more convenient to work with a basis of spherical coordinates. For a localized set of constraints with a center of symmetry, the problem can be solved directly. For an N-body study of the generation of galaxy angular momentum, a constrained formalism within a spherical harmonics basis seems therefore a convenient choice.

2.5 Other methods

Creating Gaussian constrained fields by adding a residual field, defined by the power spectrum, to an ensemble mean field, completely specified by the constraints, is not the only way to do this. Over the years, the importance of constrained realizations was realized and other methods were found create the specified initial conditions. A few of them will be presented here.

2.5.1 Convolution method

Frenk *et al.* (1985) thought of Gaussian random field as a convolution of white noise, with a power spectrum equal to $P_0 \propto k^0$, and a transfer function given by the square root of the power spectrum determined by the chosen cosmology:

$$T = \sqrt{P} e^{i\phi} \quad (2.98)$$

where the phase ϕ is irrelevant. By choosing the power spectrum, the appropriate Gaussian random field is created. In the case of the Λ CDM cosmology, the power spectrum is defined as:

$$P_{\Lambda CDM}(k) \propto T_{\Lambda CDM}^2 P_0 \quad (2.99)$$

Since white noise is uncorrelated in real space, the integral of the probability distribution can be solved in real space rather than in Fourier space.

This research was extended by Salmon (1996) to generate initial constrained realizations. A constrained realization is defined by imposing constraints on a Gaussian random field. As is mentioned before, constraining a Gaussian random field will provide again a Gaussian field with a new mean and variance, defined as:

$$\mu_c = \bar{\mu} + (c_j - \bar{c}_j) \xi_{ij}^{-1} \xi_i \quad (2.100)$$

$$\sigma_c^2 = \bar{\sigma}^2 - \xi_i \xi_{ij}^{-1} \xi_j \quad (2.101)$$

where the notation of van de Weygaert & Bertschinger (1996) is adapted. The barred quantities are the quantities of the Gaussian random field. Instead of

creating the constrained field directly, the process of filtering an unconstrained Gaussian random field is studied.

$$f_c = \bar{f} + \Delta_i \xi_{ij}^{-1} \xi_j \quad (2.102)$$

where f_c is obtained filtered realization and Δ_i is defined as:

$$\Delta_i = (c_i - \bar{c}_i) \quad (2.103)$$

This is a linear transformation, so a Gaussian random realization is created. It can be shown that the mean and variance of this filtered field are equal to the desired mean and variance of the constrained field. This means that these fields are indistinguishable and therefore the same.

This method of generating Gaussian constrained realizations has many advantages. For example, this method does not require the grid points in the N-body simulations to be evenly spaced, making it suitable for all sorts of grids in N-body simulations. Another advantage is that the same white noise can be used for all simulations: a change of cosmological model is simply a change of transfer function. Choosing a different transfer function does not alter the initial conditions drastically and therefore the same type of structure should emerge, creating an excellent laboratory for comparing different cosmologies.

Pen (1997) has implemented this method and used FFT's to calculate the convolution. The advantage of the not-evenly spaced grid points remain, since the FFT can be done on the different grid scales. The power spectrum is still defined in real space on each grid point. If the power spectrum is determined discretely in Fourier space, large errors would rise on the small wavenumbers. The convolution of the density field and the transfer function is done in Fourier space, after which the result is FFT-ed back to real space. Another advantage of this method is that the average density in the simulation box does not have to be equal to the average density of the universe.

Applications

One of the main advantages of the convolution method described above is that applicable to all sorts of grids. Bertschinger (2001) was one of the first to grasp the possibilities this method provided. He develop an algorithm to create multi-scale Gaussian constrained fields. This application is interesting when studying the evolution and formation of a certain structure, since a higher resolution can be achieved at the area of interest. This method is called adaptive mesh refinement. One of these results can be seen in figure 2.5, where the inner structure in the lower realization is the product of adaptive mesh refinement. Note by comparing this with the realization above, the inner structure created with this method is of higher resolution.

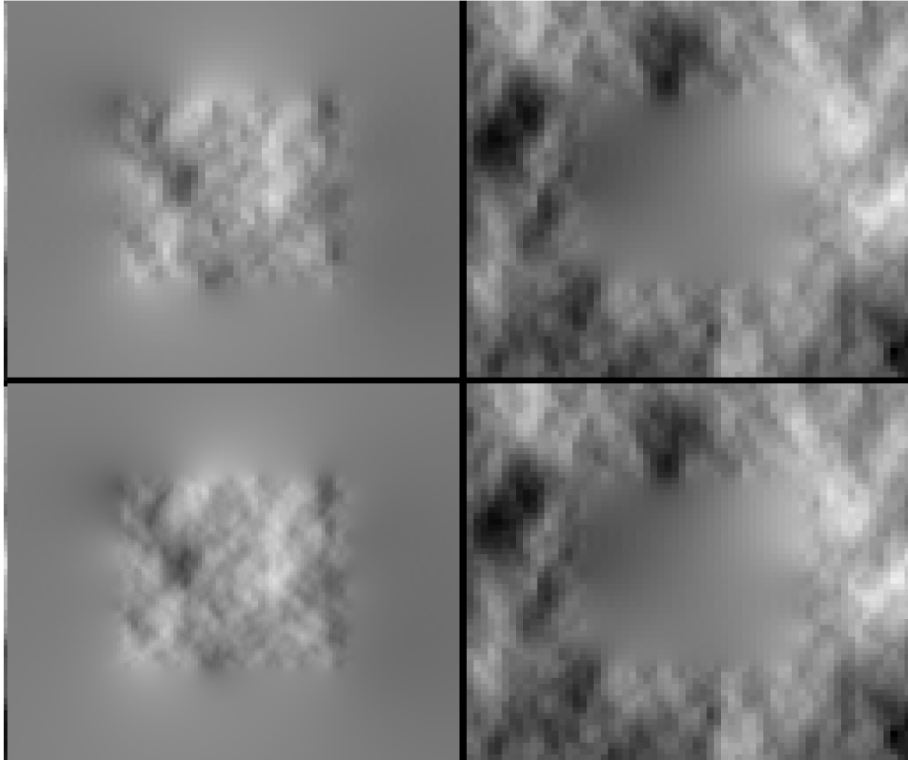


Figure 2.5: Results of the adaptive mesh refinement research of Bertschinger (2001). Shown are tidal fields in a volume of $64 Mpc$ across where the lower realization is the product of adaptive mesh refinement in the inner cube. Image courtesy to Bertschinger (2001).

The advantage of this package is that the large scale density perturbations can be related to smaller scale ones. The convolution with multi-scale resolution enforces a constraint on the white noise functions that made them coherent at the relevant scales, and not completely independent. This ensures that the small-scale structures that will develop in the high resolution simulations through gravitational collapse will know in which large-scale structure they form, at low resolution. The package Bertschinger designed is used by number of projects, for example in the Horizon project by Prunet *et al.* (2008). One of the goals of this project is to study the galaxy formation on small scales, which can be done in great precision with this adaptive mesh refinement method for the convolution method. An illustration of the project can be found in figure 2.6. (Horizonproject, n.d.)

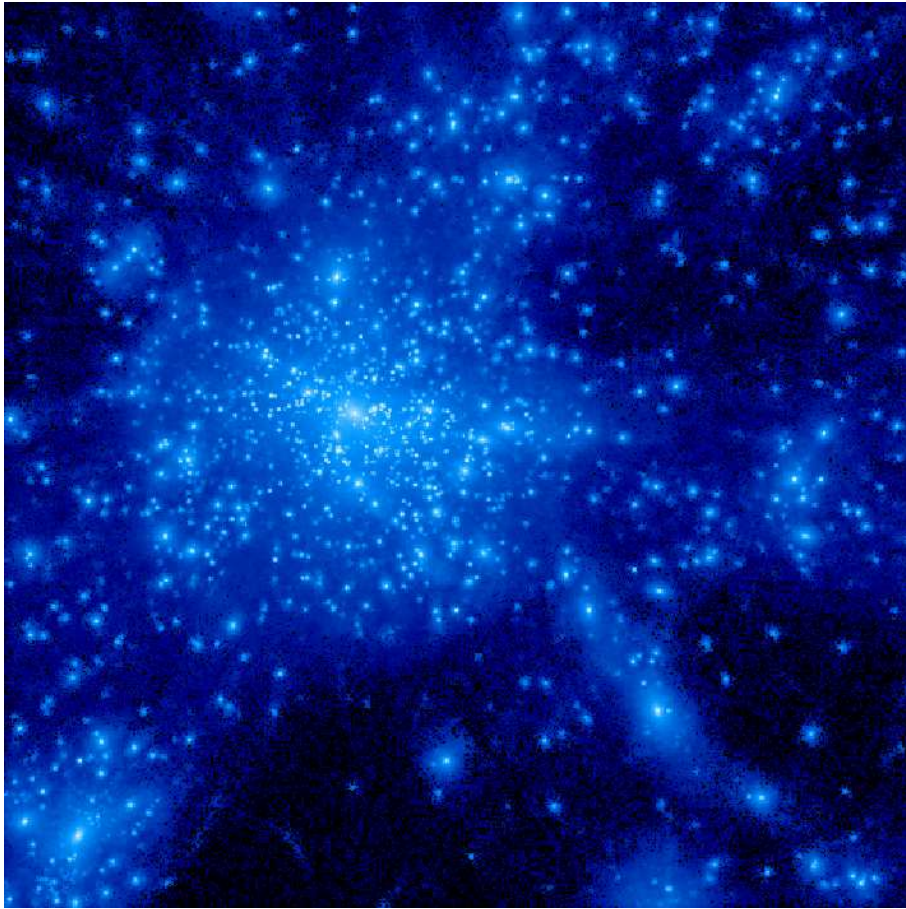


Figure 2.6: Simulation of a galaxy cluster, done by the Horizon project. Credit for the realization: Romain Teyssier.

f	$\frac{\partial f}{\partial x_1}$	$\frac{\partial f}{\partial x_2}$	$\frac{\partial f}{\partial x_3}$	$\frac{\partial^2 f}{\partial x_1^2}$	$\frac{\partial^2 f}{\partial x_2^2}$	$\frac{\partial^2 f}{\partial x_3^2}$	$\frac{\partial^2 f}{\partial x_1 \partial x_2}$	$\frac{\partial^2 f}{\partial x_1 \partial x_3}$	$\frac{\partial^2 f}{\partial x_2 \partial x_3}$	$\frac{\partial \phi}{\partial x_1}$	$\frac{\partial \phi}{\partial x_2}$	$\frac{\partial \phi}{\partial x_3}$	$\frac{\partial^2 \phi}{\partial x_1^2}$	$\frac{\partial^2 \phi}{\partial x_2^2}$	$\frac{\partial^2 \phi}{\partial x_1 \partial x_2}$	$\frac{\partial^2 \phi}{\partial x_1 \partial x_3}$	$\frac{\partial^2 \phi}{\partial x_2 \partial x_3}$
σ_0^2	0	0	0	$-\frac{\sigma_0^2}{3}$	$-\frac{\sigma_0^2}{3}$	$-\frac{\sigma_0^2}{3}$	0	0	0	0	0	0	$\frac{1}{3} f H \sigma_0^2$	$\frac{1}{3} f H \sigma_0^2$	0	0	0
0	$\frac{\sigma_0^2}{3}$	0	0	0	0	0	0	0	0	$\frac{1}{3} f H \sigma_0^2$	0	0	0	0	0	0	0
0	0	$\frac{\sigma_0^2}{3}$	0	0	0	0	0	0	0	0	$\frac{1}{3} f H \sigma_0^2$	0	0	0	0	0	0
0	0	0	$\frac{\sigma_0^2}{3}$	0	0	0	0	0	0	0	0	$\frac{1}{3} f H \sigma_0^2$	0	0	0	0	0
$-\frac{\sigma_1^2}{3}$	0	0	0	$\frac{\sigma_1^2}{5}$	$\frac{\sigma_1^2}{15}$	$\frac{\sigma_1^2}{15}$	0	0	0	0	0	0	$\frac{1}{5} f H \sigma_1^2$	$\frac{1}{15} f H \sigma_1^2$	0	0	0
$-\frac{\sigma_1^2}{3}$	0	0	0	$\frac{\sigma_1^2}{15}$	$\frac{\sigma_1^2}{5}$	$\frac{\sigma_1^2}{15}$	0	0	0	0	0	0	$\frac{1}{15} f H \sigma_1^2$	$\frac{1}{5} f H \sigma_1^2$	0	0	0
$-\frac{\sigma_1^2}{3}$	0	0	0	$\frac{\sigma_1^2}{15}$	$\frac{\sigma_1^2}{15}$	$\frac{\sigma_1^2}{5}$	0	0	0	0	0	0	$\frac{1}{15} f H \sigma_1^2$	$\frac{1}{15} f H \sigma_1^2$	0	0	0
0	0	0	0	0	0	0	$\frac{\sigma_2^2}{15}$	0	0	0	0	0	0	0	$\frac{1}{15} f H \sigma_1^2$	0	0
0	0	0	0	0	0	0	0	$\frac{\sigma_2^2}{15}$	0	0	0	0	0	0	0	$\frac{1}{15} f H \sigma_1^2$	0
0	0	0	0	0	0	0	0	0	$\frac{\sigma_2^2}{15}$	0	0	0	0	0	0	0	$\frac{1}{15} f H \sigma_1^2$
0	$\frac{1}{3} f H \sigma_0^2$	0	0	0	0	0	0	0	0	$\frac{1}{3} f H \sigma_{-1}^2$	0	0	0	0	0	0	0
0	0	$\frac{1}{3} f H \sigma_0^2$	0	0	0	0	0	0	0	0	$\frac{1}{3} f H \sigma_{-1}^2$	0	0	0	0	0	0
0	0	0	$\frac{1}{3} f H \sigma_0^2$	0	0	0	0	0	0	0	0	$\frac{1}{3} f H \sigma_{-1}^2$	0	0	0	0	0
$\frac{1}{3} f H \sigma_0^2$	0	0	0	$\frac{1}{5} f H \sigma_1^2$	$\frac{1}{15} f H \sigma_1^2$	$\frac{1}{15} f H \sigma_1^2$	0	0	0	0	0	0	$\frac{1}{5} f^2 H^2 \sigma_0^2$	$\frac{1}{15} f^2 H^2 \sigma_0^2$	0	0	0
$\frac{1}{3} f H \sigma_0^2$	0	0	0	$\frac{1}{15} f H \sigma_1^2$	$\frac{1}{5} f H \sigma_1^2$	$\frac{1}{15} f H \sigma_1^2$	0	0	0	0	0	0	$\frac{1}{15} f^2 H^2 \sigma_0^2$	$\frac{1}{5} f^2 H^2 \sigma_0^2$	0	0	0
0	0	0	0	0	0	0	$\frac{1}{15} f H \sigma_1^2$	0	0	0	0	0	0	0	$\frac{1}{15} f^2 H^2 \sigma_0^2$	0	0
0	0	0	0	0	0	0	0	$\frac{1}{15} f H \sigma_1^2$	0	0	0	0	0	0	0	$\frac{1}{15} f^2 H^2 \sigma_0^2$	0
0	0	0	0	0	0	0	0	0	$\frac{1}{15} f H \sigma_1^2$	0	0	0	0	0	0	0	$\frac{1}{15} f^2 H^2 \sigma_0^2$

Figure 2.7: The correlations described in the peak constrained formalism by van de Weygaert & Bertschinger (1996).

ν	x	y	E_y	z	E_z	$\frac{\partial f}{\partial x_1}$	$\frac{\partial \phi}{\partial x_1}$	$\frac{\partial f}{\partial x_2}$	$\frac{\partial \phi}{\partial x_2}$	$\frac{\partial f}{\partial x_3}$	$\frac{\partial \phi}{\partial x_3}$	$\frac{\partial^2 f}{\partial x_1 \partial x_2}$	$\frac{\partial^2 \phi}{\partial x_1 \partial x_2}$	$\frac{\partial^2 f}{\partial x_1 \partial x_3}$	$\frac{\partial^2 \phi}{\partial x_1 \partial x_3}$	$\frac{\partial^2 f}{\partial x_2 \partial x_3}$	$\frac{\partial^2 \phi}{\partial x_2 \partial x_3}$	
Υ	1	0	0	0	0	0	0	0	0	0	0	0	0	0	0	0	0	0
0	0	$\frac{1}{15}$	$-\frac{f \mathbb{H} \sigma_1^2}{15 \sigma_2^2}$	0	0	0	0	0	0	0	0	0	0	0	0	0	0	0
0	0	$-\frac{f \mathbb{H} \sigma_1^2}{15 \sigma_2^2}$	$\frac{1}{15} f^2 \mathbb{H}^2 \sigma_0^2$	0	0	0	0	0	0	0	0	0	0	0	0	0	0	0
0	0	0	0	$\frac{1}{5}$	$-\frac{f \mathbb{H} \sigma_1^2}{5 \sigma_2^2}$	0	0	0	0	0	0	0	0	0	0	0	0	0
0	0	0	0	$-\frac{f \mathbb{H} \sigma_1^2}{5 \sigma_2^2}$	$\frac{1}{5} f^2 \mathbb{H}^2 \sigma_0^2$	0	0	0	0	0	0	0	0	0	0	0	0	0
0	0	0	0	0	0	$\frac{\sigma_1^2}{3}$	$\frac{1}{3} f \mathbb{H} \sigma_0^2$	0	0	0	0	0	0	0	0	0	0	0
0	0	0	0	0	0	$\frac{1}{3} f \mathbb{H} \sigma_0^2$	$\frac{1}{3} f^2 \mathbb{H}^2 \sigma_{-1}^2$	0	0	0	0	0	0	0	0	0	0	0
0	0	0	0	0	0	0	0	$\frac{\sigma_1^2}{3}$	$\frac{1}{3} f \mathbb{H} \sigma_0^2$	0	0	0	0	0	0	0	0	0
0	0	0	0	0	0	0	0	$\frac{1}{3} f \mathbb{H} \sigma_0^2$	$\frac{1}{3} f^2 \mathbb{H}^2 \sigma_{-1}^2$	0	0	0	0	0	0	0	0	0
0	0	0	0	0	0	0	0	0	0	$\frac{\sigma_1^2}{3}$	$\frac{1}{3} f \mathbb{H} \sigma_0^2$	0	0	0	0	0	0	0
0	0	0	0	0	0	0	0	0	0	$\frac{1}{3} f \mathbb{H} \sigma_0^2$	$\frac{1}{3} f^2 \mathbb{H}^2 \sigma_{-1}^2$	0	0	0	0	0	0	0
0	0	0	0	0	0	0	0	0	0	0	0	$\frac{\sigma_2^2}{15}$	$\frac{1}{15} f \mathbb{H} \sigma_1^2$	0	0	0	0	0
0	0	0	0	0	0	0	0	0	0	0	0	$\frac{1}{15} f \mathbb{H} \sigma_1^2$	$\frac{1}{15} f^2 \mathbb{H}^2 \sigma_0^2$	0	0	0	0	0
0	0	0	0	0	0	0	0	0	0	0	0	0	0	$\frac{\sigma_2^2}{15}$	$\frac{1}{15} f \mathbb{H} \sigma_1^2$	0	0	0
0	0	0	0	0	0	0	0	0	0	0	0	0	0	$\frac{1}{15} f \mathbb{H} \sigma_1^2$	$\frac{1}{15} f^2 \mathbb{H}^2 \sigma_0^2$	0	0	0
0	0	0	0	0	0	0	0	0	0	0	0	0	0	0	0	0	$\frac{\sigma_2^2}{15}$	$\frac{1}{15} f \mathbb{H} \sigma_1^2$
0	0	0	0	0	0	0	0	0	0	0	0	0	0	0	0	0	$\frac{1}{15} f \mathbb{H} \sigma_1^2$	$\frac{1}{15} f^2 \mathbb{H}^2 \sigma_0^2$

Figure 2.8: The correlations described in the peak constrained formalism by van de Weygaert & Bertschinger (1996). Here the new variables are incorporated.

Chapter 3

Realizations

Constrained random fields are an useful tool for studying the evolution and formation of structure. The type of structure depends on the imposed constraints of the field. The influence of various constraints on the density and gravitational potential perturbation field can be studied easily, since the relation between cause and effect becomes directly apparent during the simulation. One frequent application of constrained field realizations are used as initial conditions for N-body simulations. As long as the density perturbations are small, the different modes in Fourier space will not interact and the evolution will evolve linearly. This can be described by a set of linearized fluid equations. (see Appendix A) When the density perturbations become large, the modes in Fourier space will interact and the nonlinear evolution sets in. This is then simulated with an N-body simulation.

By constructing various realizations and imposing different constraints, the influence on the matter distribution will be explored in this chapter. In the simplest cases, these realizations will contain a single object, either a void or a peak, but scenarios containing multiple objects will also pass the review. First the consequence of imposing constraints on the density field itself are studied, where the various realizations are compared with a reference configuration. The dynamics of the matter distribution is sculpted by constraining the peculiar velocity field. The correlations between the different constraints are studied and their consequences are derived.

3.1 Cosmological parameters

The program used to create these realizations is based on the constrained peak description by van de Weygaert & Bertschinger (1996), which is designed to create initial conditions for N-body simulations. This can be done either in the form of unconstrained Gaussian random fields or constrained realizations.

The first option generates Gaussian random fields, where the statistics of these Gaussian fields can be influenced by the user by choosing the desired power spectrum from a set of five pre-chosen power spectra. In this research the adiabatic Λ CDM power spectrum defined by BBKS is used. (Bardeen *et al.*, 1986) The normalization properties of the power spectrum are subject to the value of the cosmological parameter σ_8^2 and the most recent estimates of WMAP suggest $\sigma_8 = 0.809$. Other relevant cosmological parameters for the Λ CDM cosmology are chosen in line with recent estimates from WMAP7, such as $\Omega_m = 0.27$ and the Hubble parameter $H = 100h \text{ km/s/Mpc}$ with $h = 0.71$. (Komatsu *et al.*, 2009)

Also, a constrained realization can be created. Here both the mean field and the complete constrained realization can be constructed, along with the residual field. Naturally, the same parameters described above are used to generate the residual field.

3.2 Presentation of the simulation results

In this chapter, different sets of initial conditions will be presented. All results presented in this chapter are simulated in a cubic three-dimensional box of size $L = 100h^{-1} \text{ Mpc}$ and with a number of particles of 256 in each direction, unless otherwise denoted. All fields are smoothed with a Gaussian filter with user-specified smoothing scale R_G .

The simulation results are frequently represented by three slices through the simulation box and a corresponding density profile. The first three panels of a figure are slices through the center of the simulation box along the x -, y - and z -axis, creating a better understanding of the three-dimensional structure of the peak in the center. The color bar provides an indication of the fraction of overdensity. Overdense regions are colored towards red, while the underdense regions are colored towards blue. The color green is appointed for small or zero over- and underdensities. The density profile was sampled along the three directions through the center of the simulation box.

3.3 Creating a constrained realization

This program is built based on the formalism of Bertschinger, stating that a constrained realization is the sum of a mean field \bar{f} and a residual field $F(\mathbf{x})$. The three fields can be studied separately. An example of each of the fields is plot in figure 3.1 for a constrained realization with an elongated peak in the center of the simulation box with a height of 3σ . From left to right, one can see the mean field, the residual field and the complete constrained realization with the according density profiles.

In the first panel, the mean field is plotted. As defined, this field is com-

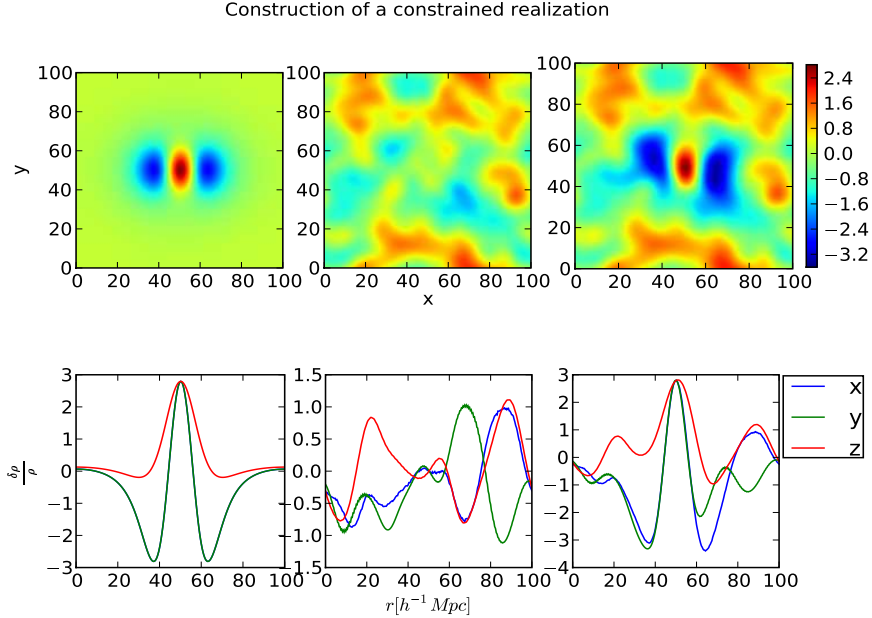


Figure 3.1: A single elongated peak at the center of the simulation box. The panel consists of the mean field, residual field and the constrained realization respectively. All three fields are smoothed with a Gaussian filter with smoothing scale of $4h^{-1} Mpc$.

pletely specified by the set of chosen constraints.

$$\bar{f}(\mathbf{x}) = \xi_i(\mathbf{x}) \xi_{ij}^{-1} c_j \quad (3.1)$$

In the corresponding density field profile of the mean field, the elongation along the z -axis becomes apparent in the width of the density profile in that particular direction.

The middle panel shows the residual field, containing the random fluctuations in the power spectrum. Here it becomes immediately apparent that the residual field is not a random generated field, since the definition specifies it to be zero at the position of imposed constraints. At the position of the peak, where the height is specified, the residual field has a value of zero. This shows again in the according density profiles, where the density is equal to zero at the specified position of the peak, which is in this case the center of the simulation box.

In the last panel, the complete constrained realization is shown, the sum of the mean field and the residual field.

$$f(\mathbf{x}) = \bar{f}(\mathbf{x}) + F(\mathbf{x}) \quad (3.2)$$

In the upper panel, both the mean and residual field can be recognized.

3.3.1 Residual field

The residual field contains the fluctuations in the power spectrum and is in the program generated using an algorithm from Press *et al.* (1992) based on the suggestion from Knuth (1981). At the position of the constraints, the residual field is equal to zero. This means that for a certain set of constraints, the residual field should always be zero at the same points. But the substructure would differ around the area due to the random number generator. Despite of this fact, the different realizations for the same set of constraints will have the same outcome. This was first realized by Ganon & Hoffman (1993).

Here initial conditions were generated for a spherical peak in the center of the simulation box with a height of $2\sigma_0$. The generation of the residual field was done four times in a row and the results of these are shown in figure 3.2, were from each realization the same slice is presented. Note that the constrained peak area is similar in all panels, but the surrounding structure differs. The color bar indicates the relative overdensity $\delta\rho/\rho$ at a specific point.

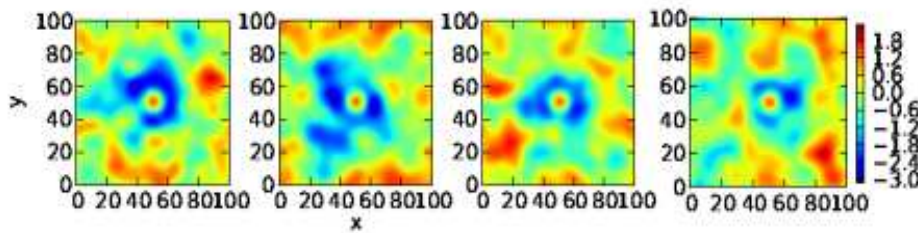


Figure 3.2: Single spherical peak in the center of the simulation box. The peak is on a scale of $4h^{-1} Mpc$ and the density field is smoothed with a Gaussian filter with a smoothing radius of $4h^{-1} Mpc$.

3.4 Simulation limitations

When working with simulations, one always has to be careful of its limitations. In this part, a study is done to the possible limitations of the scale and position of a specified object.

3.4.1 Scale

The simulation box has a finite length, which puts limits on the scale of the peak that can be chosen. In this part a default spherical peak is created with the same height and curvature, but on different scales. The results are combined in figure 3.3. The first column shows the mean unfiltered field, the second consists of the unfiltered constrained realization and the last shows the constrained realization smoothed with a smoothing scale equal to the peak scale. Note that for peaks

on scales larger than $8h^{-1} \text{ Mpc}$ the size of the box becomes a limitation. This is due to the fact that the program uses an FFT and therefore needs periodic boundary conditions. The consequence is that the average density is secured at a certain value, in this case the average density of the universe. By imposing a large size overdense object in the simulation, the surroundings of the object have to become underdense in order for the average density to be constant and there is no room for substructure.

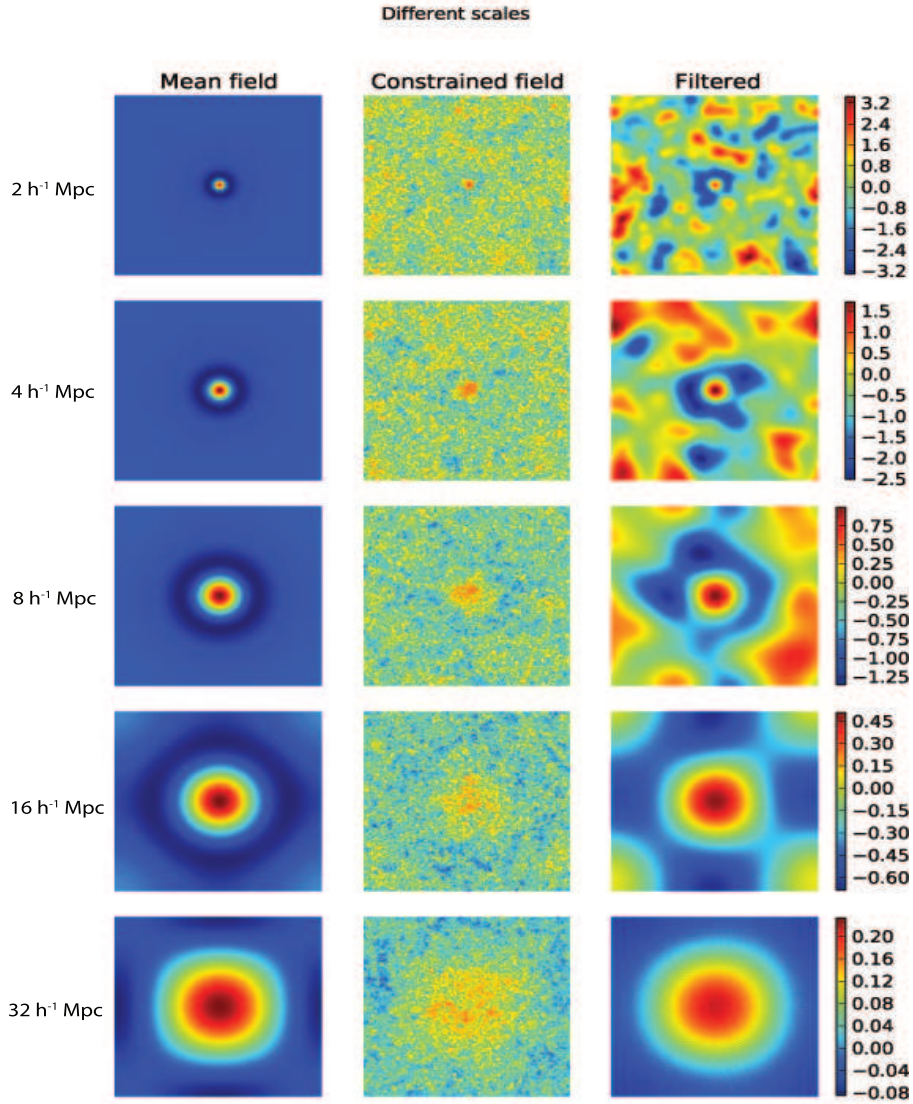


Figure 3.3: A single spherical peak at the center of the simulation box. The panel consists of the mean field, unfiltered constrained field and the filtered constrained realization respectively. The mean and filtered constrained realization are filtered with a Gaussian filter with smoothing radius equal to the scale of the object.

3.4.2 Position

One of the main limitations of the simulation is the fact that the size is not infinite. One could be curious what should happen when constraints are imposed in a way that a part will extend outside the simulation box. In order to test this, a spherical peak was placed on the edge of the simulation box, at position $(x, y, z) = (99, 99, 99)$, ensuring to extend outside it. Slices and density profiles at appropriate values were plotted to study the results. Shown in figure 3.4, the extensions of the peak which would have fallen outside the simulation box appear in the different corners of the simulation as if it was a continuous sphere. This guarantees the user that wherever a object is imposed, it will appear in the simulation box.

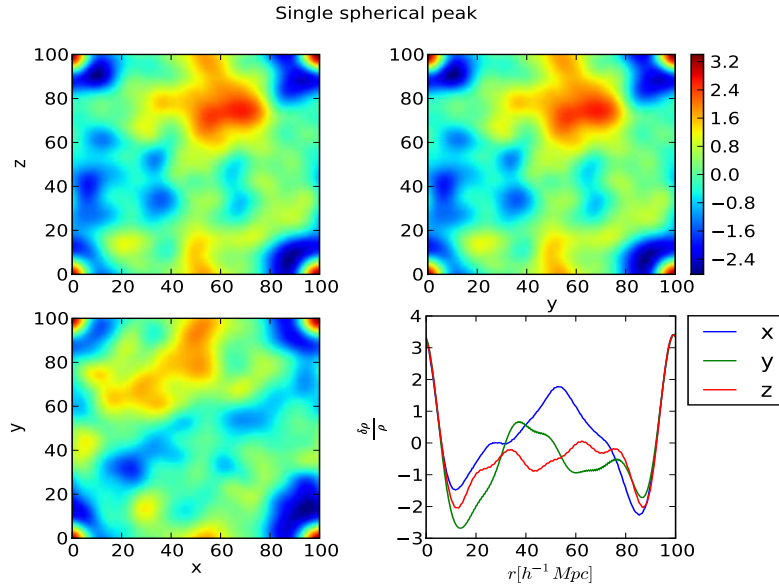


Figure 3.4: A single spherical peak at the corner of the simulation box. The three slices are taken through appropriate places in the simulation box. The field is smoothed with a Gaussian filter with smoothing scale of $4h^{-1} Mpc$.

3.5 Density constraints

The first few realizations in this chapter are focused on imposing constraints on the local density field. This can be specified by ten constraints in total. The first is the height of the peak or dip, specified by imposing a constraint on the density field itself. The height is given in the dimensionless parameter δ , which is specified according to:

$$\delta = \frac{\delta\rho}{\rho} = \nu\sigma_0 \quad (3.3)$$

This will provide a relative overdensity of underdensity at a position in the simulation box.

The first derivatives in three directions should be specified to be zero, ensuring the peak or dip to be a local maximum or minimum. If this is not specified, the study at that specific point is not a valid one, since one is then only studying a part of the structure.

The set of second derivatives of the density field specify the shape, orientation and the compactness of the peak or dip. The combination of specifying the axial ratios a_{12} and a_{13} for the shape of the peak or dip, the curvature x_d for the steepness of the profile and the Euler angles α , β and φ for the orientation, gives the second derivatives of the density field the following values:

$$\nabla_i \nabla_j f = - \sum_{k=1}^3 \lambda_k A_{ik} A_{jk} \quad (3.4)$$

where A_{jk} and A_{ik} are elements from the transformation matrix and λ_k is an eigenvalue in one of three directions, defined by:

$$\lambda_1 = \frac{x_d \sigma_2(R_G)}{1 + a_{12}^2 + a_{13}^2} \quad \lambda_2 = \lambda_1 a_{12}^2 \quad \lambda_3 = \lambda_1 a_{13}^2 \quad (3.5)$$

In general, all constraints are correlated. As we have shown in chapter 2, in the case of the constrained peak formalism, this is true for all. From the constraints mentioned above, the height of the peak or dip and the Laplacian of the density field are correlated. This is immediately shown in the correlation matrix (figure 2.7 and figure 2.8).

3.5.1 Single Objects: Peaks

In this part, the different sets of constraints on the local density field will be studied. The influence on the matter distribution of varying the height, the curvature, shape and orientation of an object will be examined. This will be done by comparing the various set of constraints with a reference configuration, created below.

Reference configuration

To realize a default scenario to compare our other simulation realizations to, a spherical peak on a scale of $4h^{-1} \text{ Mpc}$ in the center of the simulation box is created. The height is set at 3σ and the first derivatives are set at zero to ensure a local maximum. The second derivatives are constrained by choosing both axial ratios equal to one, creating a spherical shape, and the curvature term is set at the value of ten. The orientation of the peak is chosen to be aligned with the simulation box axes. The realization is smoothed with a Gaussian filter with smoothing radius equal to $4h^{-1} \text{ Mpc}$.

The results of this realization are shown in figure 3.5. Mind that the structure of the peak in the center is surrounded by a large underdense region. This is due to the requirement that the average density in the simulation box is equal to the average density of the universe.

The fourth panel presents the density profiles through the center of the simulation box along the three axis. Note that in these density profiles the imposed constraints can also be recognized. The height, shape and curvature are the imposed set of constraints that can be recognized in the density profiles, since these are the same in all three directions.

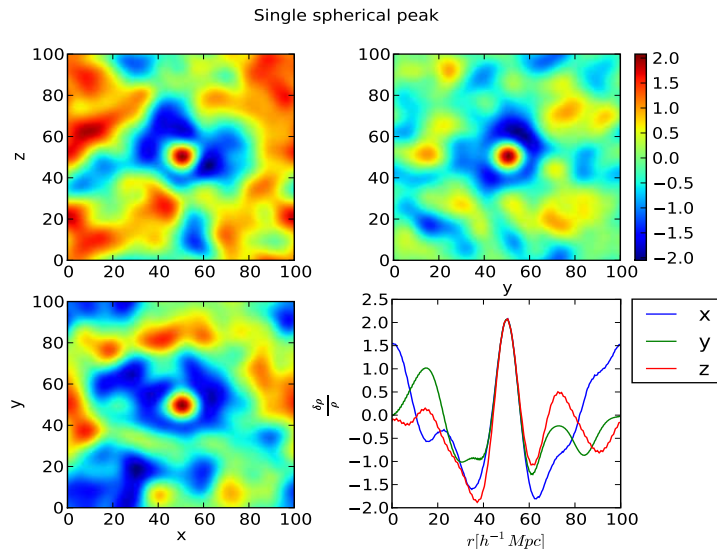


Figure 3.5: Single spherical peak in the center of the simulation box. The density field is smoothed with a Gaussian filter with smoothing radius $4h^{-1} \text{ Mpc}$ and the smoothing radius is equal to the peak scale.

Peakheight

The influence of the height of the peak on the surrounding matter distribution is examined. This is done by realizing many spherical peaks in the center of the simulation box with various heights. The values for the other constraints (the first and second derivatives) are chosen similar as in the default scenario, while the height differs between 1σ and 10σ .

The results are shown in figure 3.6. From left to right, from top to bottom, the increasing heights are presented in the same slice of the simulation box.

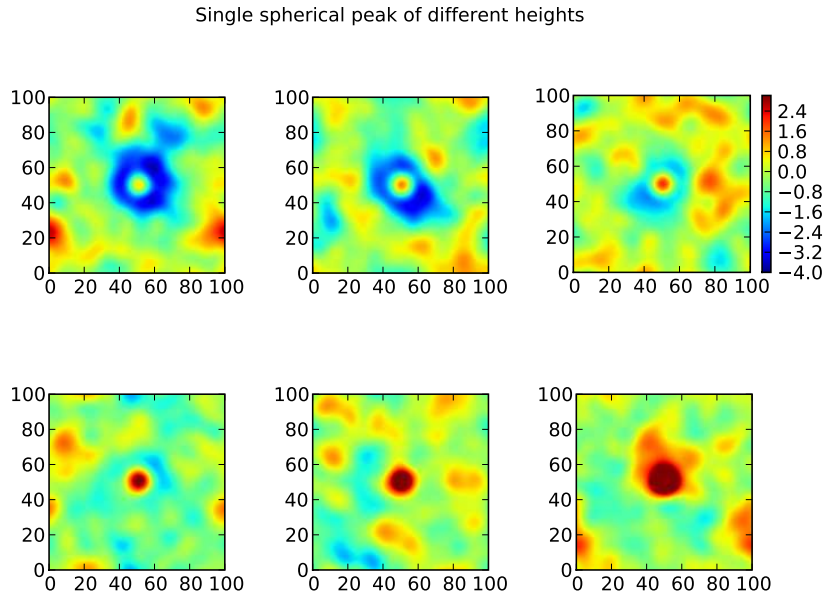


Figure 3.6: Single spherical peak in the center of the simulation box. The density field is smoothed with a Gaussian filter with smoothing radius $4h^{-1} Mpc$ and the height of the peak is different in each plot. From left to right and from top to bottom the height of the peak is equal to 1σ , 2σ , 3σ , 5σ , 7σ and 10σ .

What should be noticed is that the underdense regions surrounding the imposed structure disappears as the height of the peak increases. This is due to the correlation between the height of the peak and its curvature, which will be explained in the upcoming chapter. In this case it is interesting to compare the χ^2 distribution, to find an indication of the likelihood of the constrained field realization. The expression for the complete χ^2 can be found in eq. 2.74. Because all constraints are the same in the realizations, the χ^2 is in this case an indication of the likelihood of the height of the peak. The most likely realization is the realization with a peak with height of 2σ , where the sum of the χ^2 is approximately equal to number of degrees of freedom. The scenario with peak height of 1σ creates a χ^2 of around 15, while the scenario for a height of 10σ provides a χ^2 of 14.23.

Curvature

The effect of the changing surrounding matter distribution is due to the correlation found between height and curvature can also be studied by changing the imposed curvature value. This is done in the next two realizations, where the values of respectively $x_d = 20\sigma_2$ and $x_d = 5\sigma_2$ are chosen. The curvature at the scale of the peak is therefore either very steep ($x_d = 20\sigma_2$) or relatively less steep ($x_d = 5\sigma_2$). The other constraints, such as the height, shape and orientation are again chosen to be equal to default scenario values.

The results of the realizations can be found in figure 3.7 ($x_d = 20\sigma_2$) and figure 3.8 ($x_d = 5\sigma_2$).

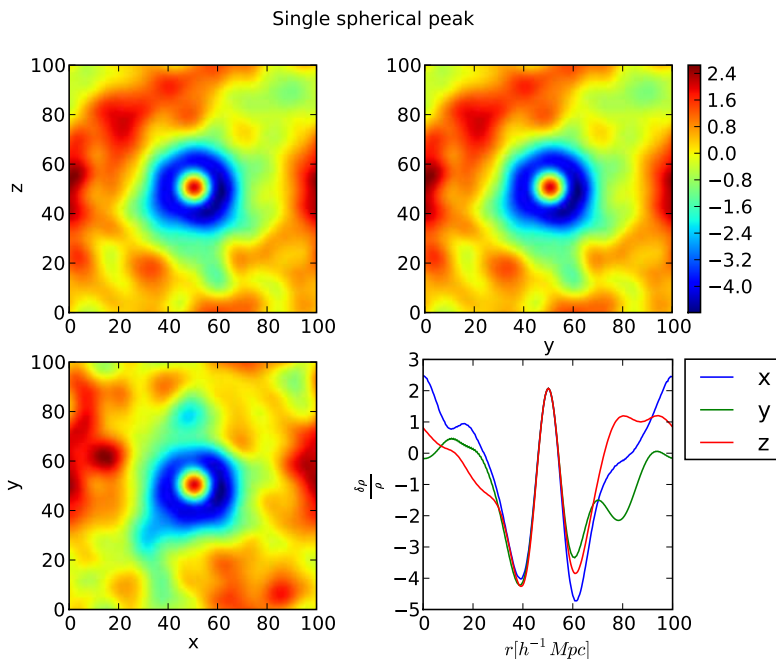


Figure 3.7: Curvature term is $x_d = 20\sigma_2$. The density field is smoothed with a Gaussian filter with smoothing radius $4h^{-1} \text{ Mpc}$ and the smoothing radius is equal to the peak scale.

As can be seen in the linear profiles through the simulations, the increase value of the curvature creates an underdense region surrounding the specified structure. Since the average density of the simulation is imposed to be equal to the average density of the universe, the density outside the underdense region should be mostly overdense. There is not a large amount of substructure present. This is not true for smaller values of curvature. In that case, there is no need to compensate for a large underdense area, so that smaller substructure is present in the simulation.

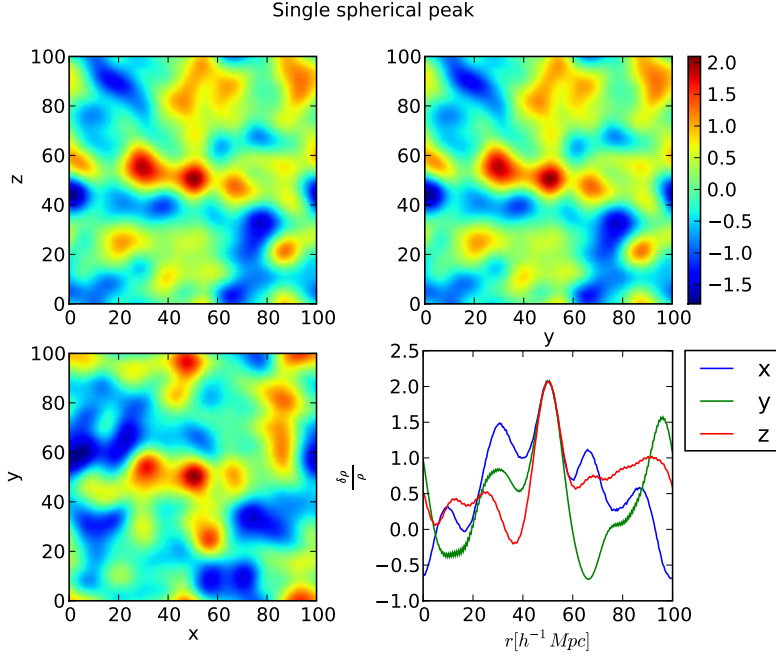


Figure 3.8: Curvature term is $x_d = 5\sigma_2$. The density field is smoothed with a Gaussian filter with smoothing radius $4h^{-1} \text{ Mpc}$ and the smoothing radius is equal to the peak scale.

We are interested in various aspects of the initial conditions realizations and in particular their underlying correlations. From the correlation matrix in figure 2.8, it can be seen that the height and the Laplacian of the density field are correlated.

$$Q_{f\nabla^2 f} = \begin{pmatrix} \langle f & f \rangle & \langle f & \nabla^2 f \rangle \\ \langle \nabla^2 f & f \rangle & \langle \nabla^2 f & \nabla^2 f \rangle \end{pmatrix} \quad (3.6)$$

$$= \begin{pmatrix} \sigma_0^2 & -\frac{\sigma_3^2}{3} \\ -\frac{\sigma_1^2}{3} & \frac{\sigma_2^2}{5} \end{pmatrix} \quad (3.7)$$

By introducing the new set of variables, the correlation matrix changes accordingly to:

$$Q_{\nu x} = \begin{pmatrix} \langle \nu\nu \rangle & \langle \nu x \rangle \\ \langle x\nu \rangle & \langle xx \rangle \end{pmatrix} \quad (3.8)$$

$$= \begin{pmatrix} 1 & \gamma \\ \gamma & 1 \end{pmatrix} \quad (3.9)$$

where ν and x are defined respectively as f/σ_0 and $-\frac{\nabla^2 f}{\sigma_2}$, where ζ_1 , ζ_2 and ζ_3 are defined as the first, second and third component of the Laplacian of the density field. The constraints are correlated by:

$$\mathbf{Q} = \sum_{i,j=1}^2 y_j Q_{ij}^{-1} y_i \quad (3.10)$$

where y is vector with the constraints. The inverse correlation matrix is equal to:

$$Q^{-1} = \begin{pmatrix} \frac{1}{1-\gamma^2} & \frac{-\gamma}{1-\gamma^2} \\ \frac{-\gamma}{1-\gamma^2} & \frac{1}{1-\gamma^2} \end{pmatrix}$$

This gives the following outcome for the correlation between the constraints:

$$\mathbf{Q} = \sum_{i,j=1}^2 y_j Q_{ij}^{-1} y_i \quad (3.11)$$

$$= \begin{pmatrix} \nu \\ x \end{pmatrix} \begin{pmatrix} \frac{1}{1-\gamma^2} & \frac{-\gamma}{1-\gamma^2} \\ \frac{-\gamma}{1-\gamma^2} & \frac{1}{1-\gamma^2} \end{pmatrix} \begin{pmatrix} \nu & x \end{pmatrix} \quad (3.12)$$

$$= \frac{\nu^2 + x^2 - 2\gamma\nu x}{1-\gamma^2} \quad (3.13)$$

$$= \nu^2 + \frac{(x - x_*)^2}{1-\gamma^2} \quad (3.14)$$

where x_* is defined as $\gamma\nu$. For a peak aligned with the simulation box axes and spherically shaped, the parameter x reduces to the curvature x_d . As the coupling term x_* indicates, this means that height and curvature are correlated.

Shape

The shape of the structure can be adapted by varying the axial ratios. All simulations up till this point have shown a spherical shaped peak. However in the universe very few perfect spherical structures are found, more common are ellipsoidal shapes. By imposing the axial ratios a_{12} and a_{13} to be respectively 1 and 2.5 an ellipsoid is created, elongated in the z -direction. Other imposed constraints are those of the reference configuration.

The results of the simulation are shown in figure 3.9. In the three slices through the simulation box the elongated peak is clearly visible. Also in the density profile the wider form in the z -direction is apparent by noting that the density profile along the z -axis is much wider than the other two.

Notice that there is but a slight underdense in the elongated direction of the specified structure. This can be explained due to the correlations represented in the correlation matrix.

$$\mathbf{Q} = \begin{pmatrix} \langle f f \rangle & \langle f \nabla_1^2 f \rangle & \langle f \nabla_2^2 f \rangle & \langle f \nabla_3^2 f \rangle \\ \langle \nabla_1^2 f f \rangle & \langle \nabla_1^2 f \nabla_1^2 f \rangle & \langle \nabla_1^2 f \nabla_2^2 f \rangle & \langle \nabla_1^2 f \nabla_3^2 f \rangle \\ \langle \nabla_2^2 f f \rangle & \langle \nabla_2^2 f \nabla_1^2 f \rangle & \langle \nabla_2^2 f \nabla_2^2 f \rangle & \langle \nabla_2^2 f \nabla_3^2 f \rangle \\ \langle \nabla_3^2 f f \rangle & \langle \nabla_3^2 f \nabla_1^2 f \rangle & \langle \nabla_3^2 f \nabla_2^2 f \rangle & \langle \nabla_3^2 f \nabla_3^2 f \rangle \end{pmatrix} \quad (3.15)$$

$$= \begin{pmatrix} \sigma_0^2 & -\frac{\sigma_1^2}{3} & -\frac{\sigma_2^2}{3} & -\frac{\sigma_3^2}{3} \\ -\frac{\sigma_1^2}{3} & \frac{\sigma_1^2}{15} & \frac{\sigma_2^2}{15} & \frac{\sigma_3^2}{15} \\ -\frac{\sigma_2^2}{3} & \frac{\sigma_2^2}{15} & \frac{\sigma_2^2}{5} & \frac{\sigma_3^2}{15} \\ -\frac{\sigma_3^2}{3} & \frac{\sigma_3^2}{15} & \frac{\sigma_3^2}{15} & \frac{\sigma_3^2}{5} \end{pmatrix} \quad (3.16)$$

By choosing the new parameters, the same part of the correlation matrix plays a role as with the curvature and again the correlation between ν and x is studied.

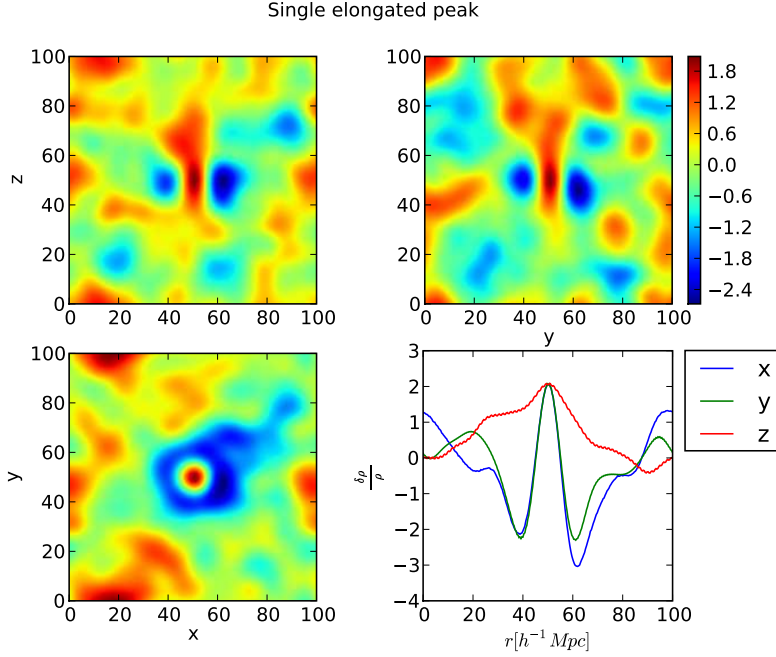


Figure 3.9: Single peak, elongated in the z -direction. in the center of the simulation box. The density field is smoothed with a Gaussian filter with smoothing radius $4h^{-1} Mpc$ and the scale of the peak is $4h^{-1} Mpc$.

By incorporating the definitions for the constraints (see eq. 2.47 and eq.2.48, the parameter x can be rewritten as:

$$x = \frac{-1}{\sigma_2} \left(\frac{-x_d \sigma_2}{1 + a_{12}^2 + a_{13}^2} + \frac{-x_d \sigma_2 a_{12}^2}{1 + a_{12}^2 + a_{13}^2} \frac{-x_d \sigma_2 a_{13}^2}{1 + a_{12}^2 + a_{13}^2} \right) \quad (3.17)$$

$$= \frac{1}{\sigma_2} \left(\frac{x_d \sigma_2}{8, 25} + \frac{x_d \sigma_2}{8, 25} + \frac{6, 25 x_d \sigma_2}{8, 25} \right) \quad (3.18)$$

The correlation between the height and the curvature is therefore more present in the z -direction, creating the probability to create more substructure in that direction.

Orientation

The orientation of an object can be changed by imposing values on the Euler angles α , β and φ . In this section, values for α and β were both chosen to be 45 degrees. This means that the structure will have rotated 45 degrees with respect to the x - and z axis of the simulation axes. The other constraints were again chosen to be the same as the default scenario.

The results of the simulation are shown in fig 3.10. Note that the density profile is equal to that of spherical peak in the center of the simulation box. This is to be expected since the imposed change of orientation created a spherical shaped peak in the center, along which the density profiles are sampled.

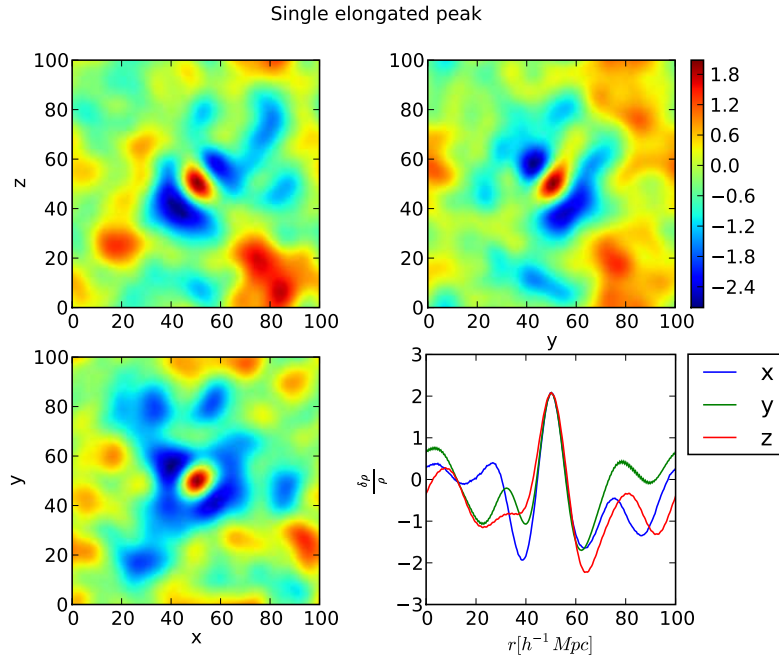


Figure 3.10: Single peak, elongated in the z -direction and turned with respect to the principal axis, in the center of the simulation box. The density field is smoothed with a Gaussian filter with smoothing radius $4h^{-1} \text{ Mpc}$.

Correlation can be found between the orientation and the shear of the peak, as was explained in the former chapter. These two tend to align. This will be explained further in section 3.6.2.

3.5.2 Single Objects: Voids

The peak formalism worked out by van de Weygaert & Bertschinger (1996) describes peaks as well as dips, since the latter are negative density extremum. The same set of constraints can be imposed, resulting in the same correlations. In this part of the research, a few realizations for voids were created. The first realization shows the default scenario for a spherical peak, but in this case with a negative height of 3σ . The similarities can be seen between figure 3.5 and figure 3.11 by comparing the contour plots and the density profiles.

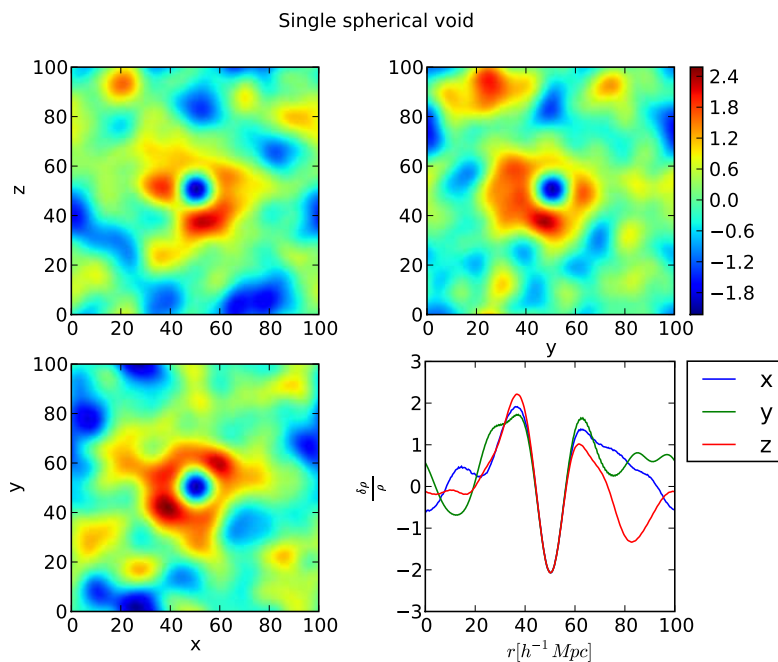


Figure 3.11: Single spherical void in the center of the simulation box. The density field is smoothed with a Gaussian filter with a smoothing radius of $4h^{-1} \text{Mpc}$ respectively and the void scale is also $4h^{-1} \text{Mpc}$.

With respect to the created spherical void, the shape is changed. The constraint values for the height, curvature and orientation remain the same. The axial ratios a_{21} and a_{31} are defined as 1 and 2.5, creating the shape of the void to be elongated in the z -direction. Note that these are the same values chosen for the axial ratios to create an elongated peak. The similarities between figure 3.12 and figure 3.9 are therefore evident.

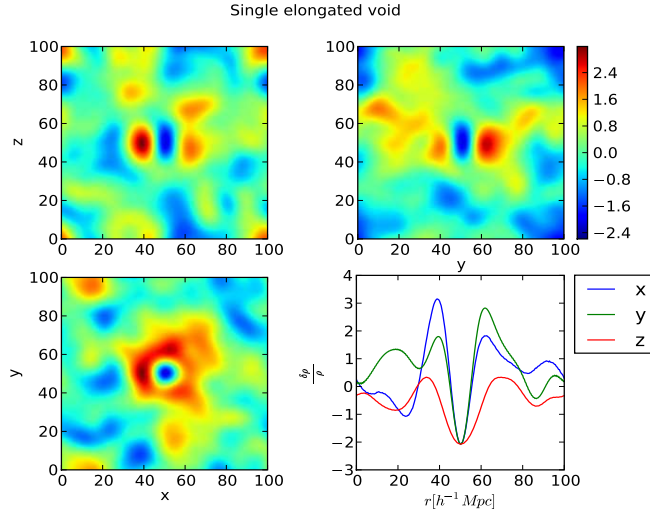


Figure 3.12: Single elongated void in the center of the simulation box. The density field is smoothed with a Gaussian filter with a smoothing radius of $4h^{-1} Mpc$ respectively and the scale of the void is $4h^{-1} Mpc$.

And just as was done when we studied the peak constraints, we also address the curvature. Here the rest of the numerical values is the same as the case of the spherical peak/void, but with a different value for the curvature, namely $x_d = 20$. Note the similarities between figure 3.7 and figure 3.13.

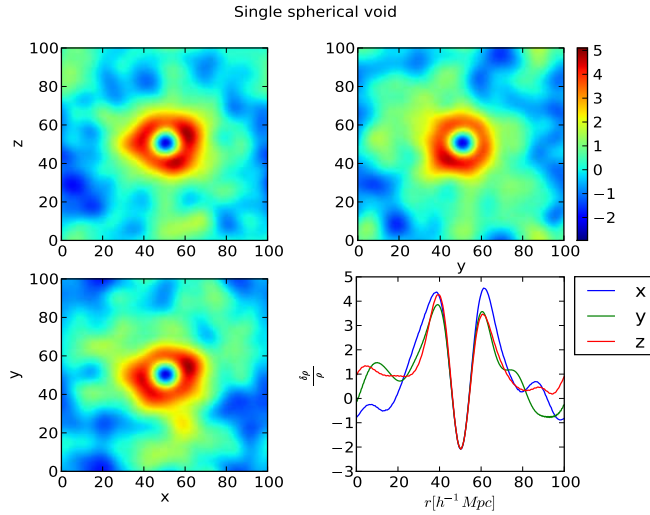


Figure 3.13: Single spherical void in the center of the simulation box. The density field is smoothed with a Gaussian filter with a smoothing radius of $4h^{-1} Mpc$ respectively and the scale of the void is $4h^{-1} Mpc$.

3.5.3 Multiple Objects

In the former realizations, we tried to get a better understanding of the constraints on the local density field around peaks and dips. This is appropriate set of initial conditions for N-body simulations for studying the evolution of specific object, such as a super void or a galaxy. N-body simulations also provide the opportunity to study the formation of large scale structure, where possible gravitational influence of diverse peaks and dips can be taken into account. In this part, some insight will be gained in the initial conditions for multiple objects. Although the objects can be placed randomly in the simulation box, for graphic reasons are the objects all placed in the same z -plane.

The first realization contains two peaks, both at the scale of $4h^{-1} \text{ Mpc}$. One peak is stationed at the center of the simulation box, spherically shaped and has a height of 3σ . The second peak is stationed slightly away from the center, at $(x, y) = (65, 65)$, has a height of 4σ and axial ratios of $a_{12} = 1.1$ and $a_{13} = 0.8$. The curvature in both cases is not specified.

The results of the simulation can be seen in figure 3.14. Note that the matter distribution of the two peaks will influence each other in the area between the two peaks. This can be seen in the left plot of the panel by the large overdense region containing both peaks. In the density profile the influence can be observed as well. Note that the density profile in all three directions is wider on the right side of the center of the simulation box.

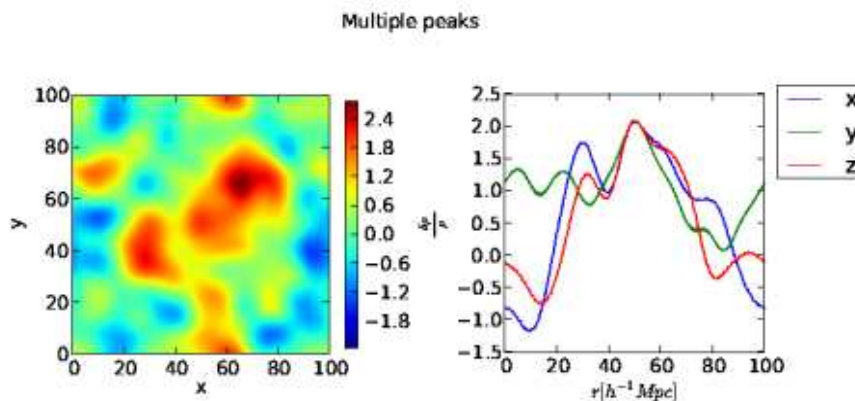


Figure 3.14: The density field was filtered with a Gaussian filter on a smoothing scale of $4h^{-1} \text{ Mpc}$ and the smoothing scale is equal to the peak scale of both peaks.

The peaks are spatially correlated as long as they are closer to each other than the correlation length. This is a measure of the range over which fluctuations in one region of space are correlated with (influence) those in another region. Two points which are separated by a distance larger than the correlation length will each have fluctuations which are relatively independent, that is, uncorrelated. The correlation can be described by the correlation matrix. The elements of this matrix consist of the two-point correlation functions, which is a function of

distance:

$$\mathbf{Q} = \begin{pmatrix} \langle f(\mathbf{x}_1)f(\mathbf{x}_1) \rangle & \langle f(\mathbf{x}_1)f(\mathbf{x}_2) \rangle \\ \langle f(\mathbf{x}_2)f(\mathbf{x}_1) \rangle & \langle f(\mathbf{x}_2)f(\mathbf{x}_2) \rangle \end{pmatrix}$$

The correlation of the density field at a position with itself is σ_0^2 , as shown in figure 2.7. The correlation between the two peaks is defined as:

$$\begin{aligned} \langle f(\mathbf{x}_1)f(\mathbf{x}_2) \rangle &= \langle f(\mathbf{x}_1 + \mathbf{r})f(\mathbf{x}_2) \rangle \\ &= \left\langle \int \frac{d\mathbf{k}_1}{(2\pi)^3} f(\mathbf{k}_1) e^{-i\mathbf{k}_1 \cdot (\mathbf{x}_1 + \mathbf{r})} W_G(\mathbf{k}_1) \int \frac{d\mathbf{k}_2}{(2\pi)^3} f^*(\mathbf{k}_2) e^{i\mathbf{k}_2 \cdot \mathbf{x}_2} W_G^*(\mathbf{k}_2) \right\rangle \\ &= \int \frac{d\mathbf{k}}{(2\pi)^3} P(k) W_G(\mathbf{k}) W_G^*(\mathbf{k}) e^{-i\mathbf{k} \cdot (\mathbf{x}_1 + \mathbf{r})} e^{i\mathbf{k} \cdot \mathbf{x}_1} \\ &= \int \frac{d\mathbf{k}}{(2\pi)^3} P(k) W_G(\mathbf{k}) W_G^*(\mathbf{k}) e^{-i\mathbf{k} \cdot \mathbf{r}} \end{aligned}$$

where \mathbf{r} is the distance between the two peaks. For two objects at the same scale, the correlation matrix can be solved analytically to:

$$\mathbf{Q} = \begin{pmatrix} \sigma_0^2 & \xi(r) \\ \xi(r) & \sigma_0^2 \end{pmatrix}$$

The correlation function can be rewritten to contain the correlation length r_0 :

$$\langle f(\mathbf{x}_1)f(\mathbf{x}_2) \rangle \propto e^{-i\mathbf{k} \cdot \frac{\mathbf{r}}{r_0}} \quad (3.19)$$

Note that the distance between the two objects is smaller than the correlation length, the exponent is large. When the distance \mathbf{r} is considerably larger than the correlation length r_0 , the exponent will become close to zero and the two objects are spatially uncorrelated. This is shown in the next realization where a third peak was added to the simulation. This peak is situated at $(x, y) = (25, 25)$ in the same z -plane. The scale is set at $5h^{-1} \text{ Mpc}$, the height is chosen to be 3.5σ and the axial ratios are both imposed at 2.

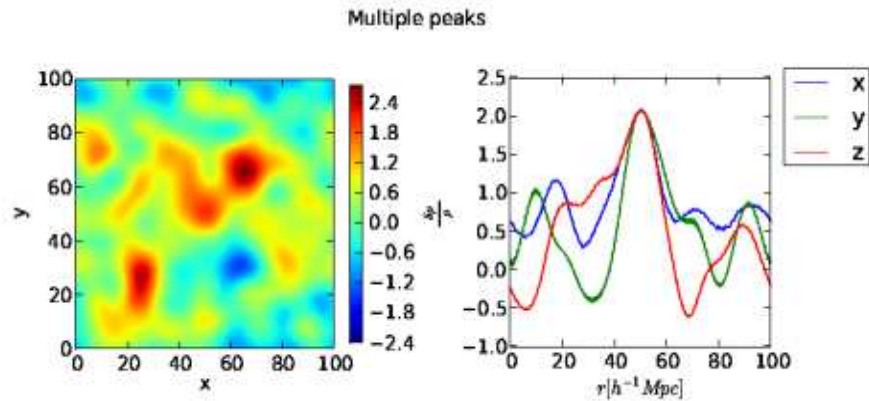


Figure 3.15: The density field was filtered with a Gaussian filter on a smoothing scale of $4h^{-1} \text{ Mpc}$ and the peak scale for two of the peaks is $4h^{-1} \text{ Mpc}$ and for one $5h^{-1} \text{ Mpc}$.

Note that the centered peak and the peak at $(x, y) = (25, 25)$ are still weakly correlated, as can be seen in the contour plots and the corresponding density profile. Now the same simulation was done, except the third peak becomes a void with the same constraints. Again, the same correlations are seen.

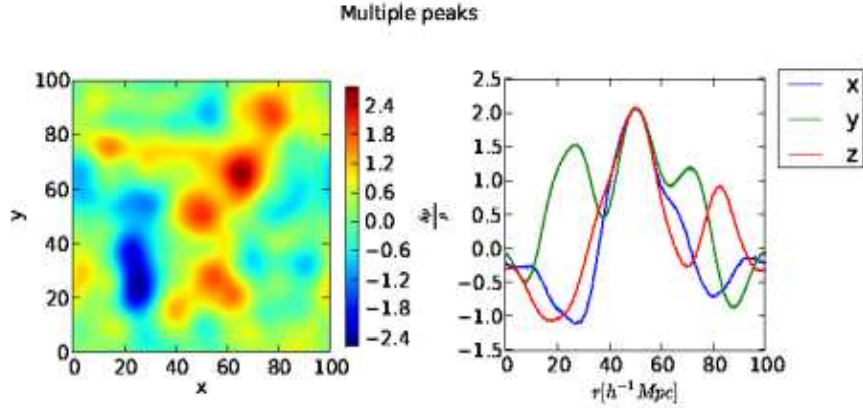


Figure 3.16: The density field was filtered with a Gaussian filter on a smoothing scale of $4h^{-1} Mpc$ and the peak scale for two of the peaks is $4h^{-1} Mpc$ and for the void $5h^{-1} Mpc$.

Subject to the assumption that galaxies trace the mass distribution, the two point correlation function of the overdensities could be deduced to the two point correlation function for galaxies. Observation reveals that the two-point correlation function then could best be represented by a power law of the form:

$$\xi(r) = \left(\frac{r_0}{r}\right)^\gamma \quad (3.20)$$

For galaxies, the best-fit parameters for $\xi(r)$ are $r_0 = 5.51 Mpc$ and $\gamma = 1.80.05$. We now can put a quantitative measure on the correlations, which can be found in the table below where the two point correlation functions for the different peaks are calculated. As expected, the correlation between the centered peak and the peak at $(65, 65)$ is the strongest.

Peak position	(25, 25)	(50, 50)	(65, 65)
(25, 25)	1	0.055	0.024
(50, 50)	0.055	1	0.138
(65, 65)	0.024	0.138	1

Substructure

When studying objects, one is also interested in the distribution of the substructure of the surrounding regions. A close-up was taken of the central regions of a simulation containing a single object to study surrounding substructure. The left panel shows a slice of the simulation box containing the unfiltered constrained realization of a Gaussian field containing a spherical object with a height/depth of 3σ . The central region of this plot is filtered at different smoothing scales to reveal the substructure. The smoothing scale R_G is equal to $1h^{-1} \text{ Mpc}$, $2h^{-1} \text{ Mpc}$ and $3h^{-1} \text{ Mpc}$ from left to right respectively. As can be seen in both the figures, smoothing the region with a smaller R_G uncovers the substructure quite nicely. Under the upper panel, the density profiles are shown. Note that the height of the simulated peak decreases as the smoothing scale increases.

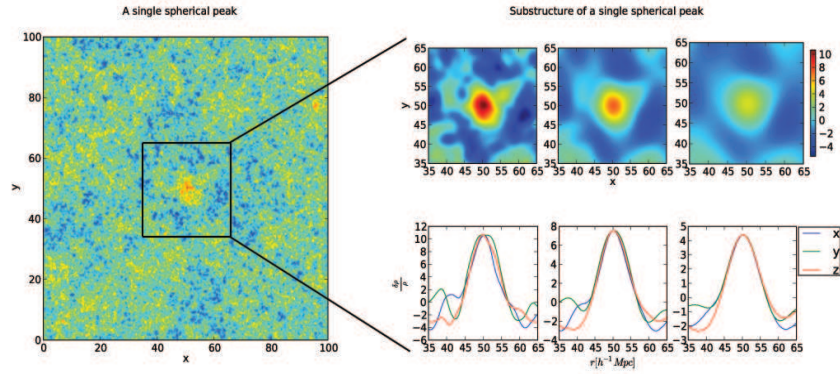


Figure 3.17: Single peak in the center of the simulation box. The density field is smoothed with a Gaussian filter with, from left to right, a smoothing radius of $1h^{-1}$, $2h^{-1}$ and $3h^{-1} \text{ Mpc}$ respectively and the scale of the peak is $3h^{-1} \text{ Mpc}$.

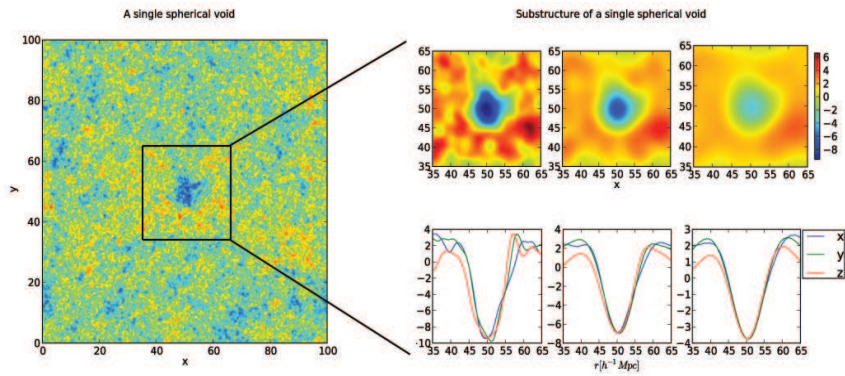


Figure 3.18: Single void in the center of the simulation box. The density field is smoothed with a Gaussian filter with, from left to right, a smoothing radius of $1h^{-1}$, $2h^{-1}$ and $3h^{-1} \text{ Mpc}$ respectively and the scale of the void is $4h^{-1} \text{ Mpc}$.

3.6 Velocity constraints

After imposing the constraints on the local density field, the dynamics of the matter evolution can be specified by imposing constraints on the gravitational potential field. Because the simulation is limited to the linear evolution regime, constraints are imposed on the peculiar velocity field instead.

$$\mathbf{v} \propto \mathbf{g} \propto \frac{\nabla\phi}{a} \quad (3.21)$$

The peculiar velocity is generated by a difference in density, implying a density dipole distribution. The strength of the peculiar velocity can be described in units of its dispersion:

$$f_v = v_i \sigma_{v, pk} \quad (3.22)$$

The orientation of the peculiar velocity field can be adjusted to obtain the user-specified initial conditions.

To study the influence of the peculiar velocity on the matter distribution, a set of default constraints is chosen for the local density field. All the simulations were created with a spherical peak on a scale of $4h^{-1}Mpc$ in the center of the simulation box. The height of the peak is chosen to be 2.5σ , while the curvature term is not imposed. The velocity constraints were varied with direction and with amplitude in order to study their effect on the matter distribution in the simulation box.

3.6.1 Peculiar velocity

In this section, the influence on the matter distribution of imposing constraints on the peculiar velocity field itself at the position of the object are studied. The direction and amplitude of a peculiar velocity in a single direction will be varied, before moving on to realizations with multiple velocities.

Direction

In this variant, the velocity is imposed to align with the simulation box axes. Here the default scenario of the peak was given a peculiar velocity of 850 km/s in the x -direction. The peculiar velocity in the y - and z -direction are chosen to be zero. As can be seen in figure 3.19 the density contour plots show a clear dipole density distribution, where there is an overdense region in the direction of the velocity and an underdense region in the opposite direction of the velocity. The influence of an imposed peculiar velocity field can also be seen in the density profile. Note that the density profile left from the center of the simulation box, in the opposite direction of the velocity, is much lower than the density profile on the right side of the simulation center, in the direction of the velocity. So here the dipole distribution is also clearly visible.

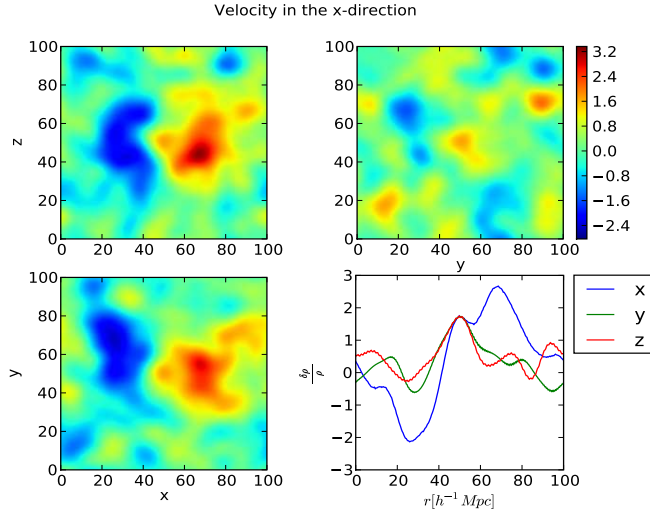


Figure 3.19: Density field containing a spherical peak in the center of the simulation box and a peculiar velocity field of 850 km/s in the x -direction. The field is smoothed with a Gaussian filter on a smoothing scale of $4h^{-1} \text{ Mpc}$.

The same results are obtained for the default scenario with a peculiar velocity in the y - and z -direction with the same strength, see figure 3.20 and figure 3.21.

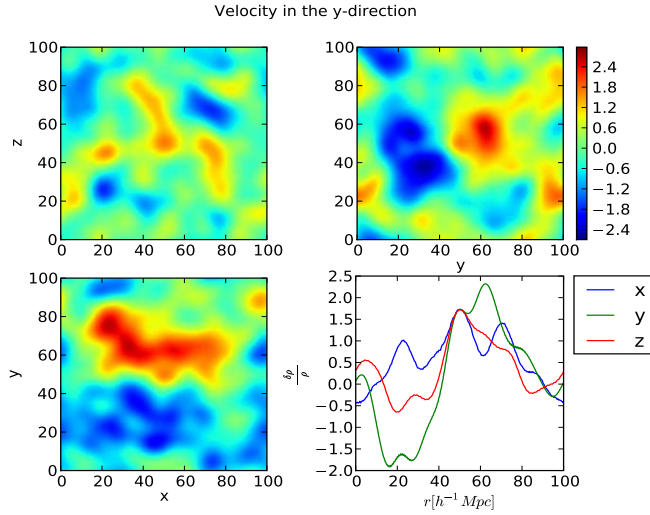


Figure 3.20: Density field containing a spherical peak in the center of the simulation box and a peculiar velocity field of 850 km/s in the y -direction. The field is smoothed with a Gaussian filter on a smoothing scale of $4h^{-1} \text{ Mpc}$.

The peculiar velocity is correlated with the first derivatives of the density field,

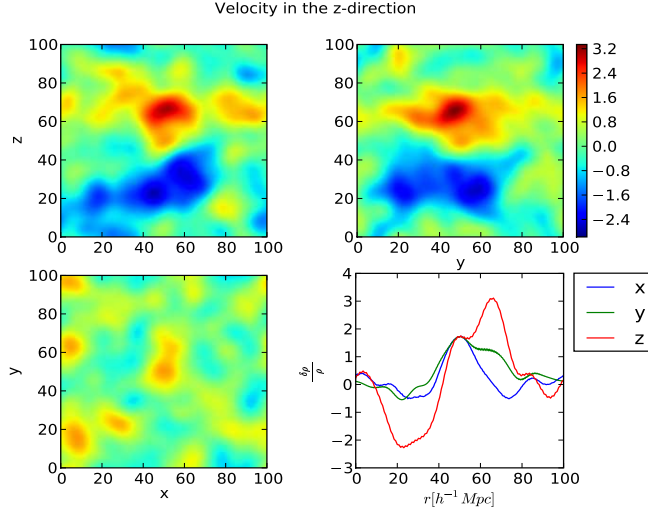


Figure 3.21: Density field containing a spherical peak in the center of the simulation box and a peculiar velocity field of 850 km/s in the z -direction. The field is smoothed with a Gaussian filter on a smoothing scale of $4h^{-1} \text{ Mpc}$.

as can be seen in figure 2.7 and figure 2.8.

$$\mathbf{Q} = \begin{pmatrix} \langle \nabla_i f \nabla_i f \rangle & \langle \nabla_i f v_i \rangle \\ \langle v_i \nabla_i f \rangle & \langle v_i v_i \rangle \end{pmatrix} \quad (3.23)$$

$$= \begin{pmatrix} \frac{\sigma_1^2}{3} & \frac{1}{3} f(\Omega) H \sigma_0^2 \\ \frac{1}{3} f(\Omega) H \sigma_0^2 & \frac{1}{3} f(\Omega)^2 H^2 \sigma_{-1}^2 \end{pmatrix} \quad (3.24)$$

In the constrained peak formalism, using the new set of variables, the above found correlation matrix does not change. The correlation in one direction can therefore be found to be:

$$\mathbf{Q} = \sum_{i,j=1}^1 y_j Q^{-1}_{ij} y_j \quad (3.25)$$

$$= \frac{v_i^2 + \gamma_v^2 f(\Omega)^2 H^2 \frac{\sigma_{-1}^2}{\sigma_1^2} \eta_i^2 - 2\gamma_v f(\Omega) H \frac{\sigma_{-1}}{\sigma_1} \eta_i v_i}{3\bar{\sigma}_v^2} \quad (3.26)$$

$$(3.27)$$

When the velocity field is positioned at the peak or dip of a structure, the first derivatives are equal to zero, such that the imposed velocity is the real velocity in the simulation. When the velocity field is not positioned at a local maximum or minimum, the first derivatives of the density field will not be zero. When the values for the first derivatives are large at the chosen position for the peculiar velocity, it indicates that the structure is compact. This means that the gravitational influence of the substructure is stronger than the force exercised by the peculiar velocity. This means that the peculiar velocity will be smaller. On the other hand, when the first derivatives are small, the influence of the gravity is negligible, so that the peculiar velocity at that position becomes large.

Amplitude

The above derivation suggests that a large peculiar velocity ensures that there is little (sub)structure. This is a statement which can be tested by imposing different amplitudes on the peculiar velocity in the field. The default configuration for the local density field is created and the strength of the peculiar velocity field is varied. The peculiar velocity is orientated in the x -direction. By doing this, some understanding of the limitations in the amplitude of the peculiar velocity is found. The program creates a standard by calculating the dispersion of the peak and the dispersion of the field in units of km/s using the definitions from the former section. For the default scenario created, $\sigma_{v,pk} \approx 639 km/s$ and $\sigma_v \approx 710 km/s$.

The resulting contour plots are shown in figure 3.22 and the corresponding density profiles in figure 3.23. In both figures, the dipole matter distribution is clearly visible and for stronger peculiar velocities even more so. The disappearance of the substructure is best seen in the corresponding profiles. For the relatively low peculiar velocities the density profiles contain a large number of fluctuations. When the strength of the peculiar velocity increases, the number of random fluctuations decrease.

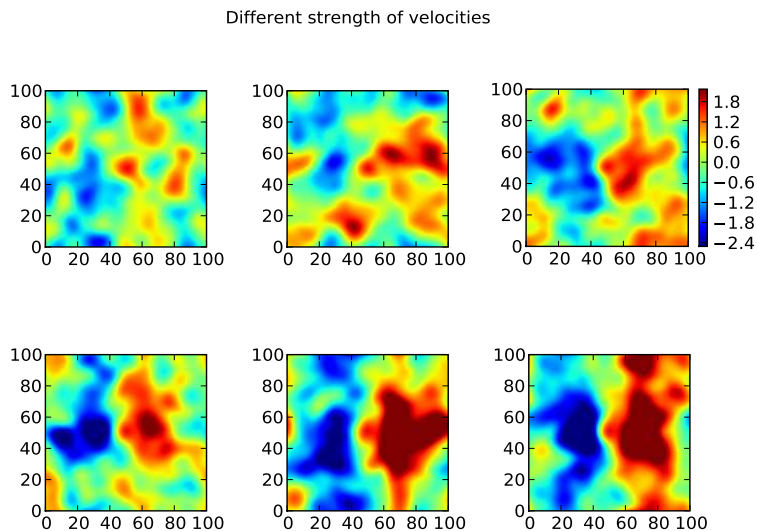


Figure 3.22: From left to right, from top top to bottom, the velocity is equal to $250 km/s$, $500 km/s$, $750 km/s$, $1000 km/s$, $1250 km/s$ and $1500 km/s$, all in the x -direction. The plots are smoothed with a Gaussian filter with a smoothing scale of $4h^{-1} Mpc$.

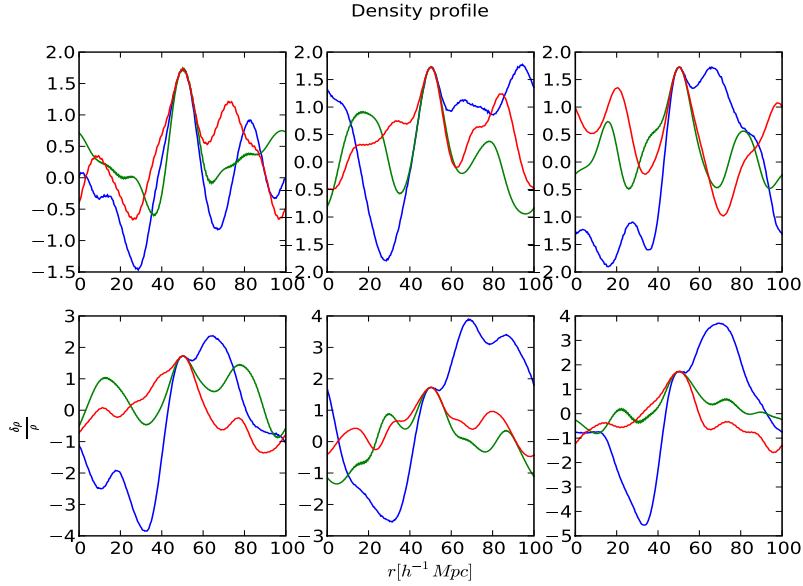


Figure 3.23: The corresponding density profiles due to the different strengths of velocities. The same setup is used as with the different strengths of velocities. The plots are smoothed with a Gaussian filter with a smoothing scale of $4h^{-1} Mpc$.

Multiple velocities

In this part of the research the matter distribution is studied for a Gaussian field subject to two peaks with varying velocity characteristics. The default Gaussian density field is created with two spherical peaks at positions $(x, y) = (25, 75)$ and $(x, y) = (75, 25)$, both in the same z -plane. The height and curvature are the same and imposed at 2σ and $x_d = 13\sigma$.

In the first figure, peak 1 (at position $(x, y) = (25, 75)$) is given a peculiar velocity of $1000 km/s$ in the positive x direction, while peak 2 (at position $(x, y) = (75, 25)$) has a peculiar velocity with the same strength, but in the opposite direction.

The results of the simulation can be found in figure 3.24, which shows respectively in the two upper panels the mean and residual field, while in the lower two panel the constrained realization and the density profile through the center of the simulation box of the latter are plotted. In the contour plots of the mean field and the constrained realization, the dipole distribution is clearly visible. The resulting matter distribution is shaped in a plane perpendicular to the x -axis. In the density profile along the x -direction a slight hint of the dipole distribution can be found.

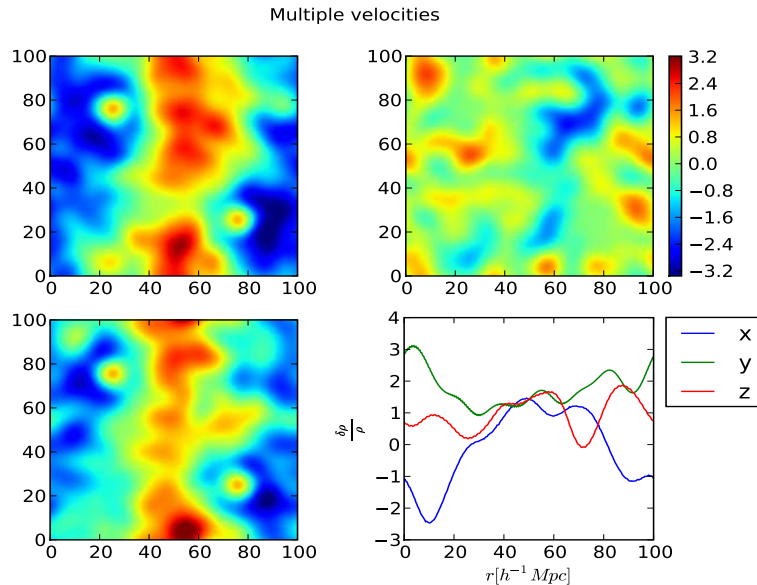


Figure 3.24: Two peaks with equal velocities in the opposite directions. The plots are smoothed with a Gaussian filter with a smoothing scale of $4h^{-1} \text{ Mpc}$.

The default local density field is contained, but the features of the peculiar velocity are changed. Peak 1 is given a peculiar velocity in the positive x -direction with a strength of 1250 km/s while peak 2 is imposed to have a peculiar velocity in the negative x -direction of 750 km/s . What one would expect is the same shape of matter distribution as in figure 3.24, both with a stronger dipole distribution in the neighborhood of peak 1 than in the neighborhood of peak 2. The results of these simulation is shown in figure 3.25 shows this (expected) result, with the mean field (upper left plot) as the most pronounced realization of the two dipoles.

Another possibility is to change the direction of the peculiar field instead of the amplitude. This is done in one last configuration concerning peculiar velocity fields. Again, the Gaussian density field is subject to the same two peaks, but now peak 1 has a peculiar velocity of 1000 km/s in the positive x -direction, while peak 2 is subject to a peculiar velocity field of the same strength but in the positive y -direction.

The results of the simulation are shown in figure 3.26. The two dipole densities create a large overdensity in the corner of the simulation. When these initial conditions are used for a N-body simulation, a large scale structure will evolve in this corner due to the two implied different dipole density distributions.

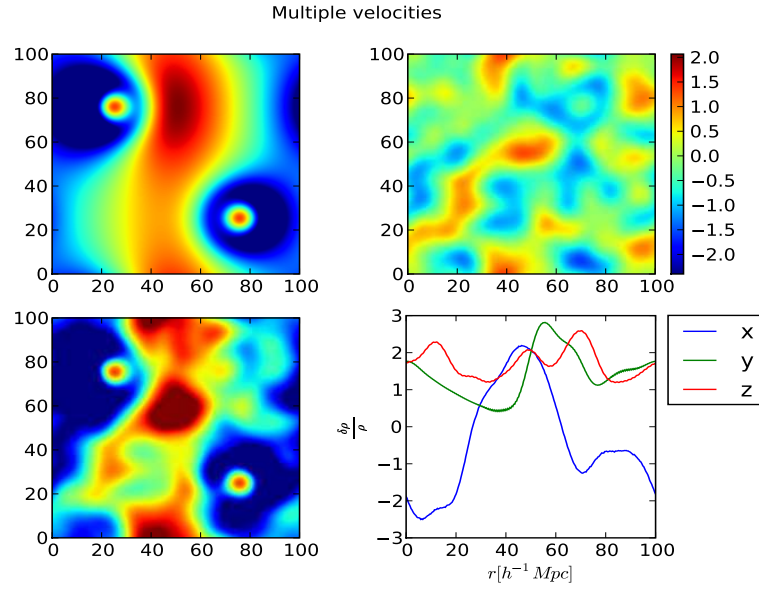


Figure 3.25: Two peaks with unequal velocities in the opposite directions. From left to right, from top to bottom, the mean field, the residual field, the constrained field and the density profile of the constrained field are plotted. The plots are smoothed with a Gaussian filter with a smoothing scale of $4h^{-1} \text{Mpc}$.

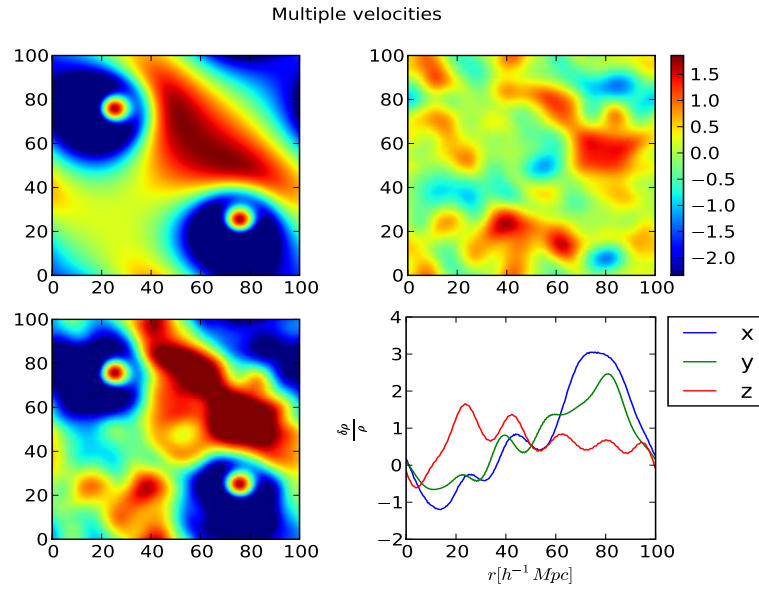


Figure 3.26: Two peaks with velocities in perpendicular directions. From left to right, from top to bottom, the mean field, the residual field, the constrained field and the density profile of the constrained field are plotted. The plots are smoothed with a Gaussian filter with a smoothing scale of $4h^{-1} \text{Mpc}$.

3.6.2 Shear constraints

The second term of the peculiar velocity multi pole expansion describes the shear of the realization. Since this is proportional to the second derivative of the gravitational potential a quadrupole distribution of matter is expected. The shear is defined by the trace free symmetric elements of the tidal field tensor, which is proportional to the shear in the linear regime:

$$\sigma_{ij} \equiv \frac{1}{2a} \left(\frac{\partial v_{G,i}}{\partial x_j} + \frac{\partial v_{G,j}}{\partial x_i} \right) - \frac{1}{3} (\nabla \cdot \mathbf{v}_G) \delta_{ij} \quad (3.28)$$

This is measure of the difference in attraction of the gravitational force. It is responsible for the creation of elongated and planar structures such as can be seen in the Cosmic Web. A positive shear component will create an expansion in that specific direction, indicating that the gravitational force is large enough to expand the structure, while a negative shear component will create an structure contraction.

The strength of the shear can be specified in terms of the dispersion of the off-diagonal components of the tensor:

$$\sigma_{ij} = \epsilon_i \sigma_E \quad (3.29)$$

For convenience, the imposed values in this research are given in $km/s/Mpc$. Here s_{11} is the shear in the x -direction, s_{22} in the y -direction, s_{33} in the z -direction and the rest a combination of these three directions. Since the tidal tensor is traceless, only two of these components can be chosen by the user. In this research, only shear components parallel to the box axes are studied, indicating that s_{12} , s_{13} and s_{23} are imposed to be zero in all upcoming simulations, just as the orientation angles α_E , β_E and φ_E .

Walls

To create the initial conditions for a sheetlike structure, contraction of the matter distribution in one direction is required and expansion in the other two directions. Translating this to the program variables it means that two shear components have to be positive, while the third is negative. (++-)

In this simulation, an elongated peak at a scale of $15h^{-1} \text{ Mpc}$ in the center of the simulation box is created. The height is set on 3σ , while the axial ratios a_{21} and a_{31} are specified to be 1 and 0.2 respectively. The curvature term is numerically set to $x_d = 15$. The shear components are imposed to $s_{11} = 50 \text{ km/s/Mpc}$ and $s_{22} = 50 \text{ km/s/Mpc}$. This means that there will be expansion of the matter distribution in the x - and y -direction, while the matter in the z -direction is contracted.

The results of the simulation can be seen in figure 3.27. The quadrupole distribution is visible in the two upper panels of the plots. Note that although the constrained realization is shown, there is just a small number of fluctuations in the density. This is due to the extreme set of constraints imposed and the requirement that the average in the simulation box must be equal to the average density in the universe.

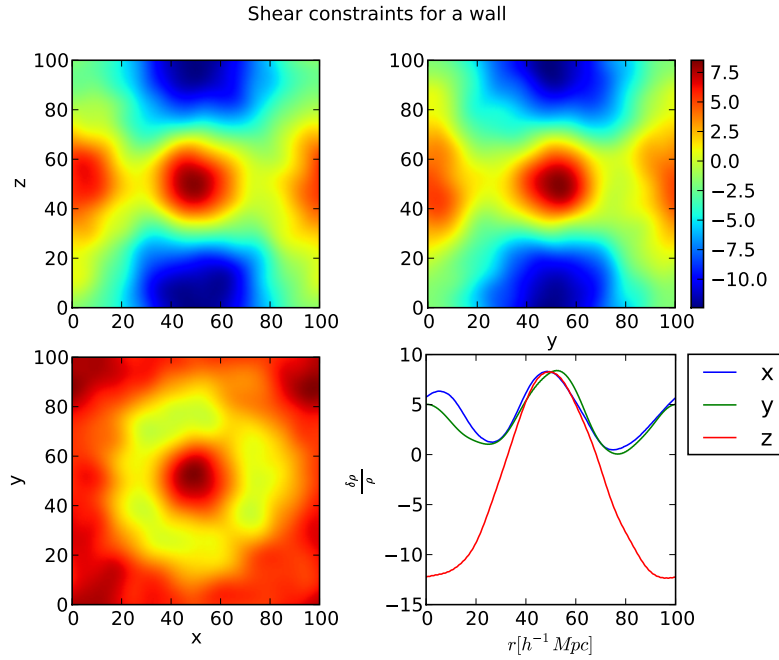


Figure 3.27: The initial conditions generated for a sheet-like structure in the large scale structure. The constraints imposed on the sphere are $s_{11} = 50 \text{ km/s/Mpc}$ and $s_{22} = 50 \text{ km/s/Mpc}$. The plots are smoothed with a Gaussian filter with a smoothing scale of $3h^{-1} \text{ Mpc}$.

When creating the same situation, both with different values for the shear com-

ponents, one would expect the matter distribution to be re sculpted. By choosing $s_{11} = 75 \text{ km/s/Mpc}$ and $s_{22} = 25 \text{ km/s/Mpc}$, the extraction of the matter should be more profound in the x -direction then in the y -direction. The results can be found in figure 3.28. The quadrupole distribution is more apparent in the x -direction then in the y direction.

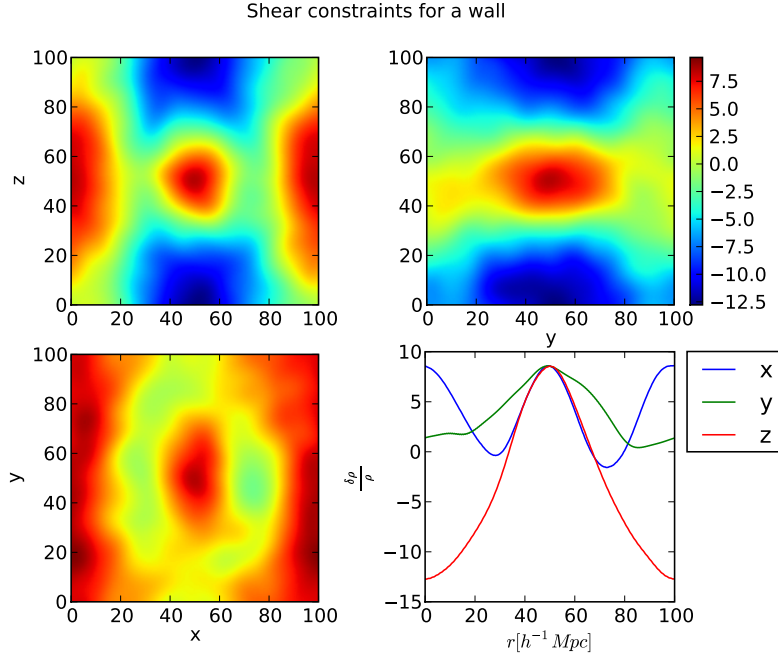


Figure 3.28: The initial conditions generated for a sheet-like structure in the large scale structure. The constraints imposed on the sphere are $s_{11} = 75 \text{ km/s/Mpc}$ and $s_{22} = 25 \text{ km/s/Mpc}$. The plots are smoothed with a Gaussian filter with a smoothing scale of $3h^{-1} \text{ Mpc}$.

Filaments

Filaments are found in the cosmic web as the strings, connecting the different kind of structures present. Initial conditions for a threadlike structure should have contraction of matter in two dimension, while in the third dimension there should be an expansion. For the program this means that there should be shear value positively defined, while two are negatively chosen. (+-)

Again the density field was subject to an elongated peak with the axial ratios $a_{21} = 0.1$ and $a_{31} = 0.1$, and a slightly lower height (2σ). The shear components are chosen $s_{11} = 100 \text{ km/s/Mpc}$ and $s_{22} = -50 \text{ km/s/Mpc}$. One would expect expansion of the matter distribution in the x -direction and contraction in the other two directions.

The simulation results can be seen in figure 3.29, exhibiting a clear quadrupole pattern.

When changing the values of the shear components to $s_{11} = 100 \text{ km/s/Mpc}$

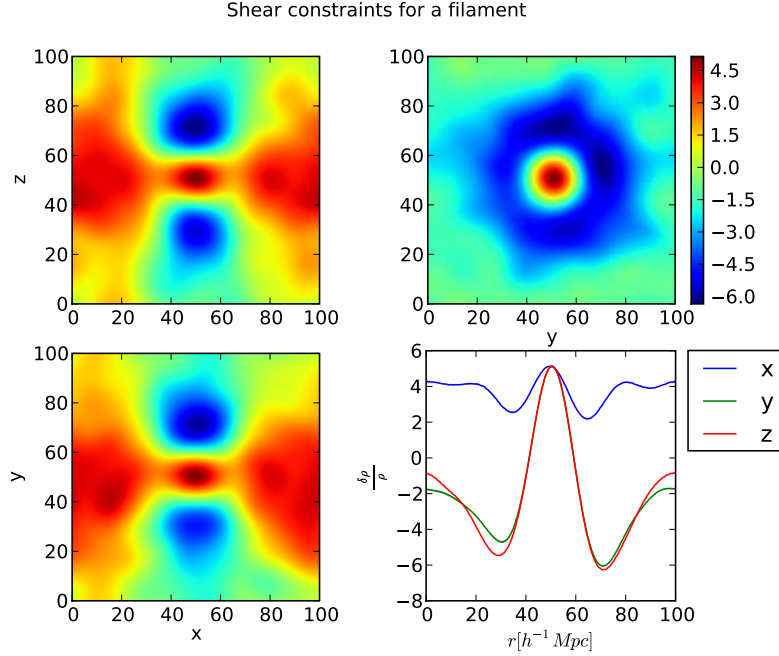


Figure 3.29: The initial conditions generated for a filament structure in the large scale structure. The constraints imposed on the sphere are $s_{11} = 100 \text{ km/s/Mpc}$ and $s_{22} = -50 \text{ km/s/Mpc}$. The plots are smoothed with a Gaussian filter with a smoothing scale of $5h^{-1} \text{ Mpc}$.

and $s_{22} = -25 \text{ km/s/Mpc}$, the matter distribution gets re sculpted according to the expectations: more contraction in the z -direction then in the y -direction of the matter distribution. Results are shown in figure 3.30 The quadrupole distribution is more profound in one direction then in the other.

As discussed earlier in this chapter, the orientation of the object and the shear of the peak are correlated. If the both the orientation and the shear are orientated along the simulation box axes, there exist a correlation between the Laplacian of the density field and Laplacian of the gravitational potential in the same direction, which can be coupled to the shear via the tidal tensor. The correlation shows in the correlation matrix.

$$\mathbf{Q} = \begin{pmatrix} \langle \nabla_i^2 f \nabla_i^2 f \rangle & \langle \nabla_i^2 f \nabla_i^2 \phi \rangle \\ \langle \nabla_i^2 \phi \nabla_i^2 f \rangle & \langle \nabla_i^2 \phi \nabla_i^2 \phi \rangle \end{pmatrix} \quad (3.30)$$

$$= \begin{pmatrix} \frac{\sigma_2^2}{5} & \frac{1}{2} H f(\Omega) \sigma_1^2 \\ \frac{1}{2} H f(\Omega) \sigma_1^2 & \frac{1}{3} H^2 f^2(\Omega) \sigma_0^2 \end{pmatrix} \quad (3.31)$$

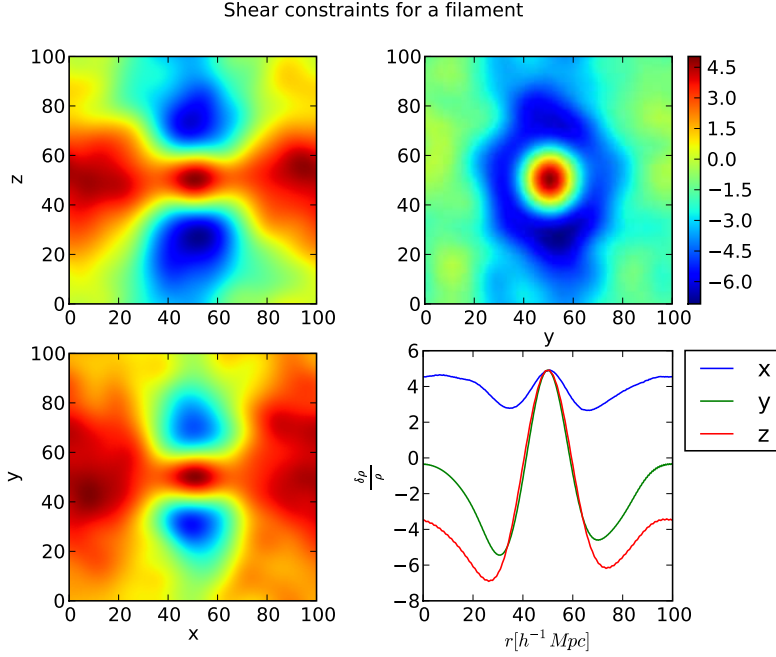


Figure 3.30: The initial conditions generated for a filament structure in the large scale structure. The constraints imposed on the sphere are $s_{11} = 100 \text{ km/s/Mpc}$ and $s_{22} = -25 \text{ km/s/Mpc}$. The plots are smoothed with a Gaussian filter with a smoothing scale of $5h^{-1} \text{ Mpc}$.

When the object and the shear are not specified along the simulation axes, the components $\nabla_k \nabla_l f$ $k \neq l$ and $\nabla_i \nabla_j \phi$ for $i \neq j$ become nonzero. The various components of the Laplacian of the density field and gravitational potential field will correlate when $k = i$ and $l = j$, imposing the two physical quantities to align. In the correlation matrix, this is visualized as:

$$\mathbf{Q} = \begin{pmatrix} \langle \nabla_i \nabla_j f \nabla_i \nabla_j f \rangle & \langle \nabla_i \nabla_j f \nabla_i \nabla_j \phi \rangle \\ \langle \nabla_i \nabla_j \phi \nabla_i \nabla_j f \rangle & \langle \nabla_i \nabla_j \phi \nabla_i \nabla_j \phi \rangle \end{pmatrix} \quad (3.32)$$

$$= \begin{pmatrix} \frac{\sigma_2^2}{15} & \frac{1}{15} H f(\Omega) \sigma_1^2 \\ \frac{1}{15} H f(\Omega) \sigma_1^2 & \frac{1}{15} H^2 f^2(\Omega) \sigma_0^2 \end{pmatrix} \quad (3.33)$$

A complete overview of the various realizations is presented in Appendix D.

Chapter 4

GRF's in spherical harmonics

The method thought of by Hoffman and Ribak has some computational considerations. As noted in the paper of van de Weygaert & Bertschinger (1996), the main limitation of the application is that of the evaluation of the correlation functions ξ_{ij} and ξ_i requires the procedure of $M^2 + M$ Fourier integrals, where M is the number of constraints put on the Gaussian density field. By replacing this number of Fourier integrals with two Fast Fourier Transforms, the computational costs reduce to $\Theta(N \log N)$ where N is proportional to the size of the simulation box cubed. As can be seen, for a large dynamic range, the diagonalization is a slow process. Binney and Quinn found a solution for this problem by writing the simulations in spherical coordinates instead of Cartesian coordinates. In a spherical coordinate system, the particular matrix is block diagonal, which suggests that diagonalizing is done by diagonalizing a number of N -dimensional matrices rather than one N^3 matrix, which reduces computational cost.

4.1 Density field in spherical harmonics

In spherical coordinates, the density field can be described in spherical harmonics multiplied by a spherical Bessel function rather than in planar waves. The derivation of the description of the density field in spherical harmonics from the time-independent Schrodinger equation can be found in E.

$$f(\mathbf{x}) = \sqrt{\frac{2}{\pi}} \kappa_n f_{lm}(k_n) j_l(k_n r) Y_l^m(\theta, \phi) \quad (4.1)$$

In this equation κ_n is a normalization constant and f_{lm} are the amplitudes of the density field. The spherical Bessel functions, denoted by $j_l(k_n r)$, are the radial solutions to the time-independent Schrodinger equation and consist of a combination of sines and cosines.

The spherical harmonics, denoted by $Y_l^m(\theta, \phi)$, are the solution for the two

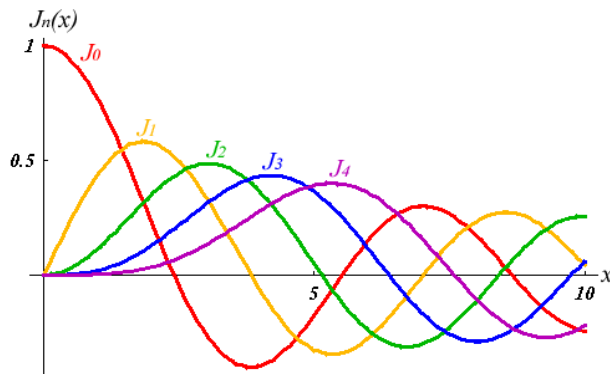


Figure 4.1: Graphs of the first order spherical Bessel functions

angles in the spherical coordinate system. These angular solutions can then again be separated into an exponential function, with only a dependence on the longitudinal angle ϕ , and a Legendre polynomial P_l^m , which only depends on the polar angle θ .

$$Y_l^m(\theta, \phi) = \left[\frac{2l+1}{4\pi} \frac{(l-m)!}{(l+m)!} \right]^{1/2} P_l^m(\cos\theta) e^{im\phi} \quad (4.2)$$

where $P_l^m(\cos\theta)$ is an associated Legendre polynomial. By scaling each point of the Y_l^m 's radially by the absolute value and coloring it according to value, it can be seen that poles are created. The number of poles depend on the value of the integer l .

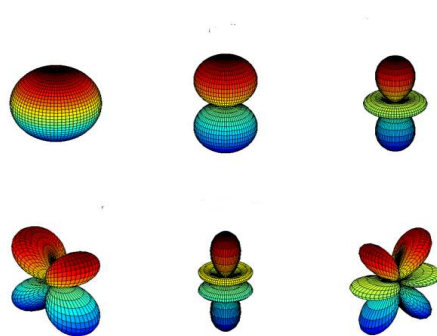


Figure 4.2: Different low-order spherical harmonics are plotted.

A list of spherical Bessel functions and spherical harmonics can be found in the Appendix E.1.

This basis of spherical Bessel functions and spherical harmonics is orthonor-

mal and complete.

$$\langle k'l'm' | klm \rangle = \frac{2kk'}{\pi} \int r^2 dr j_{l'}(kr) j_l kr \quad (4.3)$$

$$\times \int d\omega Y_{l'}^{m'}(\theta, \phi) Y_l^m(\theta, \phi) \quad (4.4)$$

$$= \delta(k - k') \delta_{l'l'} \delta_{mm'} \quad (4.5)$$

So to create a Gaussian distributed density field in spherical harmonics, it has to be proven that the amplitudes are Gaussian distributed, This can be done by sampling the probability distribution function, or more precise, the action integral $S[f]$.

In the upcoming sections, a general expression for the action integral is found, an expression for the integral in Fourier space and for an action integral with spherical harmonics as base.

4.2 General base

The density field is Gaussian distributed, which means that the probability distribution function is of the form:

$$P[f] \propto e^{-S[f]} \quad (4.6)$$

In this formula, $S[f]$ is referred to as the action integral. In real space this is defined as:

$$S[f] \equiv \frac{1}{2} \int \int d^3 \mathbf{x}_1 d^3 \mathbf{x}_2 f(\mathbf{x}_1) K(\mathbf{x}_1, \mathbf{x}_2) f(\mathbf{x}_2) \quad (4.7)$$

In this formula, K is the inverse of the correlation matrix M_{ij} , which is composed of the two point correlation function ξ_{ij} .

$$\int d\mathbf{x} K(\mathbf{x}_1 - \mathbf{x}) \xi_{ij}(\mathbf{x} - \mathbf{x}_2) = \delta_D(\mathbf{x}_1 - \mathbf{x}_2) \quad (4.8)$$

A general solution for the action integral in spherical coordinates in \mathbf{k} -space will be found. For this the Dirac notation is used, which described the state of a physical system in a complex Hilbert space. The state of a system is represented by the projection $|f\rangle$ onto a basisvector $|\mathbf{x}_1\rangle$ and written as:

$$\langle \mathbf{x}_1 | f \rangle = \int \langle \mathbf{x}_1 | \mathbf{x}_2 \rangle \langle \mathbf{x}_2 | f \rangle d\mathbf{x}_2 = f(\mathbf{x}_1) \quad (4.9)$$

where the unity matrix is defined as :

$$\mathbf{I} = \int |\mathbf{x}_2\rangle \langle \mathbf{x}_2| d\mathbf{x}_2 \quad (4.10)$$

This means that the action integral can be rewritten to Dirac notation:

$$S[f] = \frac{1}{2} \langle f | \mathbf{x}_1 \rangle \langle \mathbf{x}_1 | K | \mathbf{x}_2 \rangle \langle \mathbf{x}_2 | f \rangle \quad (4.11)$$

Using the definition for the unity matrix, a general expression for the action integral can be found. This is true whatever bases is chosen:

$$S[f] = \frac{1}{2} \langle f | K | f \rangle \quad (4.12)$$

4.3 Fourier space

When changing from real \mathbf{x} -space to Fourier or \mathbf{k} -space, the formula for the action integral will include the change of base projections. Notice that in this definition, the identity matrix again is used. The action in integral in \mathbf{k} -space can be rewritten to be:

$$\begin{aligned} S[f] &= \frac{1}{2} \langle f | \mathbf{x}_1 \rangle \langle \mathbf{x}_1 | \mathbf{k}_1 \rangle \langle \mathbf{k}_1 | \mathbf{x}_1 \rangle \langle \mathbf{x}_1 | K | \mathbf{x}_2 \rangle \langle \mathbf{x}_2 | \mathbf{k}_2 \rangle \langle \mathbf{k}_2 | \mathbf{x}_2 \rangle \langle \mathbf{x}_2 | f \rangle \\ &= \frac{1}{2} \langle f | \mathbf{k}_1 \rangle \langle \mathbf{k}_1 | K | \mathbf{k}_2 \rangle \langle \mathbf{k}_2 | f \rangle \end{aligned} \quad (4.14)$$

Since the inverse covariance matrix K is diagonal in \mathbf{k} space:

$$\langle \mathbf{k}_1 | K | \mathbf{k}_2 \rangle = K(k_1) \delta_D(\mathbf{k}_1 - \mathbf{k}_2) \quad (4.15)$$

The action integral is now defined to be:

$$S[f] = \frac{1}{2} \langle f | \mathbf{k}_1 \rangle K(k_1) \langle \mathbf{k}_1 | f \rangle \quad (4.16)$$

The above result is compared with the solution found by (van de Weygaert & Bertschinger (1996)). There the action integral was found to be equal to eq. 4.7. Rewriting this in Dirac notation in real space, the action integral is equal to eq. 4.13. The relationship between spherical coordinate systems in \mathbf{x} -space and \mathbf{k} -space is equal to:

$$\langle \mathbf{k} | \mathbf{x} \rangle = \frac{1}{\sqrt{2\pi}} e^{i\mathbf{k} \cdot \mathbf{x}} \quad (4.17)$$

So solving the action integral, it can be found that:

$$S[f] = \frac{1}{2} f(\mathbf{x}_1) \frac{e^{i\mathbf{k}_1 \cdot \mathbf{x}_1}}{\sqrt{2\pi}} \langle \mathbf{k}_1 | \mathbf{x}_1 \rangle \langle \mathbf{x}_1 | K | \mathbf{x}_2 \rangle \langle \mathbf{x}_2 | \mathbf{k}_2 \rangle \frac{e^{-i\mathbf{k}_2 \cdot \mathbf{x}_2}}{\sqrt{2\pi}} f(\mathbf{x}_2) \quad (4.18)$$

$$= \frac{1}{2} \int \int f(\mathbf{x}_1) \frac{e^{i\mathbf{k}_1 \cdot \mathbf{x}_1}}{\sqrt{2\pi}} \langle \mathbf{k}_1 | K | \mathbf{k}_2 \rangle \frac{e^{-i\mathbf{k}_2 \cdot \mathbf{x}_2}}{\sqrt{2\pi}} f(\mathbf{x}_2) d\mathbf{x}_1 d\mathbf{x}_2 \quad (4.19)$$

When working in the diagonalization of the matrix K in \mathbf{k} -space, it can be found:

$$S[f] = \frac{1}{2} \int \int \frac{e^{i\mathbf{k} \cdot \mathbf{x}_1}}{\sqrt{2\pi}} f(\mathbf{x}_1) K(k) \frac{e^{-i\mathbf{k} \cdot \mathbf{x}_2}}{\sqrt{2\pi}} f(\mathbf{x}_2) d\mathbf{x}_1 d\mathbf{x}_2 \quad (4.20)$$

When studying the above equation, the definition for the Fourier transform from the paper van de Weygaert & Bertschinger (1996) can be recognized:

$$f(\mathbf{k}) = \int \frac{d\mathbf{k}}{(2\pi)^3} f(\mathbf{x}) e^{-i\mathbf{k} \cdot \mathbf{x}} d\mathbf{x} \quad (4.21)$$

The action integral can be rewritten to:

$$S[f] = \frac{1}{2} 4\pi^2 \int \int f^*(\mathbf{k}) K(k) f(\mathbf{k}) d\mathbf{x}_1 d\mathbf{x}_2 \quad (4.22)$$

Since K is diagonal in \mathbf{k} -space, eq. 4.15 holds. By convolution theorem, it is found:

$$\int \frac{d\mathbf{k}}{(2\pi)^3} K(\mathbf{k}) P(k) e^{i\mathbf{k} \cdot (\mathbf{x}_1 - \mathbf{x}_2)} = \delta_D(\mathbf{x}_1 - \mathbf{x}_2) \quad (4.23)$$

This implies that $K(k)$ is equal to $4\pi^2/P(k)$, where $P(k)$ is the power spectrum. So the action integral can be found to be:

$$S[f] = \frac{1}{2} \int \frac{f^*(\mathbf{k})f(\mathbf{k})}{P(k)} d\mathbf{k} \quad (4.24)$$

$$= \frac{1}{2} \int \frac{|f(\mathbf{k})|^2}{P(k)} d\mathbf{k} \quad (4.25)$$

Again the action integral indicates that the amplitudes are Gaussian distributed.

4.4 Density field in Spherical harmonics

When change from a \mathbf{k} -space to a base consisting spherical harmonics, another change of coordinate systems is introduced:

$$\langle \mathbf{k}_1 | klm \rangle = \frac{2\pi i^l}{k} Y_l^m(\theta', \phi') \quad (4.26)$$

The action integral can now be rewritten to:

$$S[f] = \frac{1}{2} \int d^3\mathbf{k} \langle f|\mathbf{k} \rangle K(k) \langle \mathbf{k}|f \rangle \quad (4.27)$$

$$= \frac{1}{2} \int d^3\mathbf{k} \sum_{lm} \langle f|klm \rangle \langle klm|\mathbf{k} \rangle K(k) \times \sum_{l'm'} \langle \mathbf{k}|kl'm' \rangle \langle kl'm'|f \rangle \quad (4.28)$$

$$= \frac{1}{2} \int k^2 dk K(k) \sum_{lm'l'm'} \langle f|klm \rangle \times \quad (4.29)$$

$$\int d\omega_k \langle klm|\mathbf{k} \rangle \langle \mathbf{k}|kl'm' \rangle \langle kl'm'|f \rangle \quad (4.30)$$

The last part of this integral is equal to:

$$\int d\omega_k \langle klm|\mathbf{k} \rangle \langle \mathbf{k}|kl'm' \rangle = \frac{4\pi^2}{k^2} \delta_{ll'} \delta_{mm'} \quad (4.31)$$

The term $\langle klm|f \rangle$ is rewritten to be $f_{lm}(k)$ and the integral form of the action S becomes:

$$S[f] = \sum_{lm} \int \frac{f_{lm}^*(k) f_{lm}(k)}{2P(k)} dk \quad (4.32)$$

In which $P(k)$ is the powerspectrum and defined to be:

$$P(k) = \frac{1}{4\pi^2 K(k)} \quad (4.33)$$

So it is shown that the amplitudes $f_{lm}(k)$ in discrete \mathbf{k} -space are Gaussian distributed and the phases uniformly distributed.

In the above derivation, the relationships between the real spherical coordinate \mathbf{x} -space, a continuous spherical \mathbf{k} -space and a discrete spherical \mathbf{k} -space are

derived. When using eq. 4.21, a description of the density field in discrete \mathbf{k} -space can be found:

$$f(\mathbf{x}) = \int f(\mathbf{k})e^{-i\mathbf{k}\cdot\mathbf{x}}d\mathbf{x} \quad (4.34)$$

$$= \langle f | \mathbf{x} \rangle \langle \mathbf{x} | \mathbf{k} \rangle \quad (4.35)$$

$$= \langle f | klm \rangle \langle klm | \mathbf{x} \rangle \langle \mathbf{x} | \mathbf{k} \rangle \quad (4.36)$$

where the term $\langle \mathbf{x} | \mathbf{k} \rangle$ represent the Fourier transform with the relationship earlier defined (eq. 4.17) and the relationship found in Binney & Quinn (1991) is used:

$$\langle \mathbf{x} | klm \rangle = \sqrt{\frac{2}{\pi}} k j_l(kr) Y_l^m(\theta, \phi) \quad (4.37)$$

So the density field in spherical coordinates in discrete \mathbf{k} -space, up to a normalization constant, can be described by:

$$f(\mathbf{x}) = \sqrt{\frac{2}{\pi}} \kappa_n f_{lm}(k) k j_l(kr) Y_l^m(\theta, \phi) \quad (4.38)$$

Note that when calculations, such as Fourier Transforms, are done in a certain volume, the integral is replaced by a sum.

4.5 Constrained realizations: Binney and Quinn formalism

The requirement that the overdensity f peaks at the origin, destroys the translation invariance of the field. The density field in spherical coordinates will then look as follows:

$$f(\mathbf{x}) = \sqrt{\frac{2}{\pi}} \sum_{lmn} \kappa_n f_{lm}(k_n) j_l(k_n r) Y_l^m(\theta, \phi) \quad (4.39)$$

in which f_{lm} is a three dimensional set of amplitudes. The wave numbers are chosen in a way that ρ vanishes on the bounding sphere $r = r_{max}$. The normalization constant κ_n is defined as:

$$\kappa_n \equiv \frac{\sqrt{\pi}}{r_{max}^{3/2} j_{l+1}(k_n r_{max})} \quad (4.40)$$

The density field is required to be Gaussian, so that the statistical distribution is completely specified by it's power spectrum. In the above formula, it has to be shown that the amplitudes are Gaussian distributed. This can be done by means by the action integral. As mentioned earlier, the probability distribution function of a Gaussian density field is The density field is smoothed with the filter function $w(k_n)$ which tends to go to zero for large k_n .

$$\bar{f}(\mathbf{x}) = \sqrt{\frac{2}{\pi}} \sum_{lmn} w(k_n) \kappa_n f_{lm}(k_n) j_l(k_n r) Y_l^m(\theta, \phi) \quad (4.41)$$

We assume that our coordinate system is aligned with the principal axes of the peak positioned at the origin and Taylor expanded around this position.

$$f(\mathbf{x}) = f(0) + \frac{1}{2}[\lambda_x x^2 + \lambda_y y^2 + \lambda_z z^2] \quad (4.42)$$

Mathematically, it is preferred to work with the four equivalent numbers:

$$I_0 \equiv \sqrt{2\pi}\bar{f}(0) \quad (4.43)$$

$$I_{00} \equiv -\sqrt{2\pi}(\lambda_x + \lambda_y + \lambda_z) \quad (4.44)$$

$$I_{20} \equiv \pi\sqrt{10}\left[\lambda_z - \frac{1}{2}(\lambda_x + \lambda_y)\right] \quad (4.45)$$

$$I_{22} \equiv \frac{\pi\sqrt{15}}{2}(\lambda_x - \lambda_y) \quad (4.46)$$

These variables have coefficients that will compensate the constants coming from the Y_l^m 's. For convenience, additional symbols $I_{1m} = 0$ for $m = 0, 1$ and $I_{21} = 0$ are defined. This gives us seven constraints. (including the fact that the first derivatives have to be equal to zero, ten constraints are noted) The density field is smoothed on some scale k_0^{-1} and can be rewritten to be:

$$\sqrt{\frac{\pi}{2}}\bar{f}(\mathbf{x}) = \frac{1}{\sqrt{4\pi}} \int f_0(k)j_0(kr)kw(k)dk + \quad (4.47)$$

$$\sum_m Y_1^m(\theta, \phi) \int f_{1m}(k)j_1(kr)kw(k)dk + \quad (4.48)$$

$$\sum_m Y_2^m(\theta, \phi) \int f_{2m}(k)j_2(kr)kw(k)dk + \dots \quad (4.49)$$

By expanding the spherical Bessel functions in powers of r and filling in the appropriate terms for the Y_l^m 's, the set of constraints can be rewritten:

$$I_0 = \sum_n f_0(k_n)\kappa_n w(k_n) \quad (4.50)$$

$$I_{00} = \sum_n f_0(k_n)\kappa_n k_n^2 w(k_n) \quad (4.51)$$

$$I_{1m} = \sum_n f_{1m}(k_n)\kappa_n k_n w(k_n) \quad (4.52)$$

$$I_{2m} = \sum_n f_{2m}(k_n)\kappa_n k_n^2 w(k_n) \quad (4.53)$$

Notice that the above equations each only contain one set of indices (l, m) . This means that f_{lm} is no longer dependent on the different pairs of (l, m) . So with one pair indices dealing at the time, the density amplitude can be noted as $f_{lm}(k_n) = f_n$. Now it has to be proven that f_n is Gaussian distributed.

So, if the sum is expanded until it consists of N terms, the N number of $f_0(k_n)$ amplitudes have to satisfy two linear equations in which no other amplitudes appear, while the sets of the N amplitudes $f_{10}(k_n)$, $f_{11}(k_n)$, etcetera, only have to satisfy one linear equation per set. However, the two described cases, $l = 0$

and $2 \leq l < 0$, can be merged by defining for each l a set of N -vectors \mathbf{c}^j by:

$$\mathbf{c}_n^j \equiv \begin{cases} \kappa_n w(k_n) & l = 0, j = -1 \\ \kappa_n k_n^2 w(k_n) & l = 0, j = 0 \\ \kappa_n k_n w(k_n) & l = 1, j = 0 \\ \kappa_n k_n^2 w(k_n) & l = 2, j = 0 \end{cases}$$

By defining $I^{-1} \equiv I_0$ and $I^0 \equiv I_{lm}$ for $l = 0, 1, 2$, the seven linear equations can be rewritten to:

$$\sum_n c_n^j f_n = I^j \quad \text{where } j = \begin{cases} 0, -1 & \text{if } l = 0 \\ 0 & \text{if } 0 < l \leq 2 \end{cases} \quad (4.54)$$

and $f_n \equiv f_{lm}(k_n)$. If we think of f_n as the components of a vector in a N -dimensional space, above equation states that this vector lies in a certain generalized plane. Gram-Schmidt orthonormalization can be used to find a basis of vectors \mathbf{v}^j ($j \geq 0$) such that the first two of those vectors span the same subspace as the vectors \mathbf{c}^j . For the case $2 \leq l < 0$ this means that an orthonormal set of vectors \mathbf{v}^j must can be found, for which for example the first vector, \mathbf{v}^0 , is parallel to \mathbf{c}^0 . In the case of $l = 0$, the vectors \mathbf{v}^{-1} and \mathbf{v}^0 are simply linear combinations of \mathbf{c}^{-1} and \mathbf{c}^0 . Mathematically, this can be seen as:

$$\mathbf{v}^j = \sum_{k \leq 0} \gamma_{jk} \mathbf{c}^k \quad (j \leq 0) \quad (4.55)$$

where γ_{jk} is a number in the case $2 \leq l < 0$ and for $l = 0$ a two-by-two matrix. In order to show that the density amplitudes vector \mathbf{f} is a random Gaussian distribution, the vector is broken into a component parallel and a component perpendicular to the field of the constraining vectors \mathbf{c}^j :

$$\mathbf{f} = \mathbf{u} + \sum_{\alpha \geq 1} b_\alpha \mathbf{v}^\alpha \quad (4.56)$$

in which b_α is a real coefficient and where \mathbf{u} is defined as:

$$\mathbf{u} \equiv \sum_{j \leq 0, k \leq 0} \gamma_{jk} \mathbf{I}^j \mathbf{v}^k \quad (4.57)$$

Regardless of the values for b_α , it can be seen that $\mathbf{c}^j \cdot \mathbf{f} = \mathbf{I}^j$. This means that b_α are random variables. Now it must be proven that their probability distribution is Gaussian. Therefore, the inverse correlation matrix K is defined to be:

$$\mathbf{K}_{\alpha\beta} \equiv \sum_{n=1}^N \frac{v_n^\alpha v_n^\beta}{P_n} \quad (4.58)$$

which has eigenvalues of σ_α^2 . This can be done using the action integral, which is now a quadratic function of the coefficients b_α :

$$S = \frac{1}{2} \sum_n \frac{1}{P_n} \left(u_n^2 + \sum_{\alpha \geq 0} u_n v_n^\alpha (b_\alpha + b_\alpha^*) + \sum_{\alpha, \beta \geq 0} b_\alpha v_n^\alpha v_n^\beta b_\beta^* \right) \quad (4.59)$$

The linear term in b_α is replaced with $b_\alpha = \tilde{b}_\alpha + a_\alpha$, where a_α are complex variables where the real and imaginary parts independently Gaussian distributed. The real numbers \tilde{b}_α solve:

$$\sum_{n=1}^N \frac{v_n^\alpha}{P_n} \left(u_n + \sum_{\beta \geq 0} v_n^\beta \tilde{b}_\beta \right) = 0 \quad (4.60)$$

In order to diagonalize the matrix K , a final variable transformation is introduced: $a_\alpha \equiv \sum_{\beta \geq 0} R_{\alpha\beta} a_\beta$. Now the action integral can be rewritten to:

$$S = \frac{1}{2} \sum_n \frac{1}{P_n} \left[u_n^2 + 2 \sum_{\alpha > 0} u_n v_n^\alpha \tilde{b}_\alpha + \sum_{\alpha, \beta \geq 0} \tilde{b}_\alpha v_n^\alpha v_n^\beta \tilde{b}_\beta \right] + \frac{1}{2} \sum_{\alpha > 0} \frac{|a_\alpha|^2}{\sigma_\alpha^2} \quad (4.61)$$

Real and imaginary parts are Gaussian distributed with zero mean and variance σ_α^2 . So the amplitude vector \mathbf{f} can be written in the form of:

$$\mathbf{f} = \mathbf{u} + \sum_{\alpha > 0} \tilde{b}_\alpha v^\alpha + a_\alpha \sum_{\beta > 0} k_\beta^\alpha v^\beta \quad (4.62)$$

Chapter 5

Applications

The most frequent usage of the constrained field formalism is generating initial conditions for N-body simulations. These are applied as laboratories to analyze the (nonlinear) evolution and formation of structure through gravitational forces. By imposing various sets of constraints on a Gaussian random field, their different influences on the formation of the structure can be studied. An example of this can be found in the research of van de Weygaert & van Kampen (1993), where the depth of a void was varied to explore the consequences for its development. Also different cosmological models were explored to find their impact on the structure formation. The equivalent can be done on larger scales by simulating the large scale structure of a region of the universe. This is among others done by Ganon & Hoffman (1993) in an attempt to find initial conditions resembling our Local Group. Besides structure formation, the evolution of anything with a cosmological origin can be studied. Such an example is the Extra Galactic Magnetic Field, as was done by Dolag *et al.* (2005) in search for the origin of cosmic rays. All will be reviewed in this chapter, with a specific interest in their application of the constrained field description.

5.1 Specific objects: voids, galaxies, halos, etc.

Constraining Gaussian random fields is a perfect tool to study the influence of the various parameters, since the consequence of altering a constraint becomes directly visible in the results. The constrained simulations in earlier years were mostly focused on cluster of galaxies, since these objects are the most massive structures in the universe. When redshift sky surveys revealed the weblike structure in the universe, it became apparent that a large fraction in space consisted of voids. (de Lapparent *et al.*, 1986), (Geller & Huchra, 1989) They were believed to be created from the underdense region in the initial Gaussian density field. (Hoffman & Shaham, 1982) Instead of attracting material and collapsing with respect to the expansion of the universe, voids grew larger and emptier during their evolution. (Faber & Burstein, 1988) Astronomers discovered that voids play an important role in the formation and evolution of the large scale structure of the universe. (Icke, 1984),(Bertschinger, 1985) To obtain a complete cosmological picture, a better understanding of voids was needed.

Simulations to the rescue..

The first simulations studying voids contained an isolated, spherical symmetric void with idealized density and velocity profile. (Peebles, 1982), (Hoffman *et al.*, 1983), (Hausman *et al.*, 1983) Here the gravitational interactions with nearby objects were neglected, just as the inhomogeneities created at the origin of the void. Ikeuchi & Umemera (1984) were one of the first to follow the evolution of a underdense region in the gravitational instability scenario. The extension of this research was done by van de Weygaert & van Kampen (1993). The different aspects aspects of voids, such as shape, substructure distribution and density and velocity profiles was explored for different cosmological models using constrained initial conditions. Although up to ten constraints can be specified for a dip in a Gaussian density field (see constrained peak formalism by van de Weygaert & Bertschinger (1996)), only the depth of the void was constrained in this research. The scale of the void was chosen to be the same in all simulations to make comparison between the obtained results simpler. The constrained initial conditions were from two different fields, as suggested by the formalism of Bertschinger (1987). The mean field consisted of an approximate spherical underdense region and the residual field was completely determined by the chosen power spectrum. The superposition of the two fields created the inhomogeneities expected at the edge of the void. One of the many results of the study were shown in figure 5.1, where the substructure in a specific void is generated.

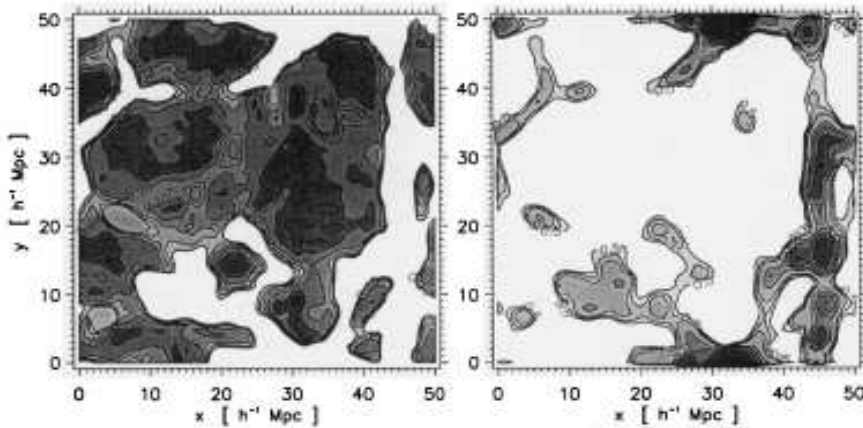


Figure 5.1: Substructure of a void. In the left panel, the underdense regions are plotted, while in the right plot the same was done for the high density regions, where the break is set at $\rho = 0.5\bar{\rho}$. Image courtesy to van de Weygaert & van Kampen (1993).

If it works for one...

If it is possible to generate constrained realizations for one type of structure, it is bound to work for other various objects. The constrained field formalism is suitable for all sorts of configurations, such as X-ray clusters (Evrard, 1990), voids (van de Weygaert & van Kampen, 1993), (clusters of) galaxies. (Evrard *et al.*, 1990), (Klypin *et al.*, 2003), (Mezler & Evrard, 1994), (van Haarlem & van de Weygaert, 1993) and dark matter halos (Romano-Diaz *et al.*, 2009), (Romano-Diaz *et al.*, 2010), (Evrard *et al.*, 2008). An example of the latter is shown in figure 5.2, where three dark matter halos are simulated.

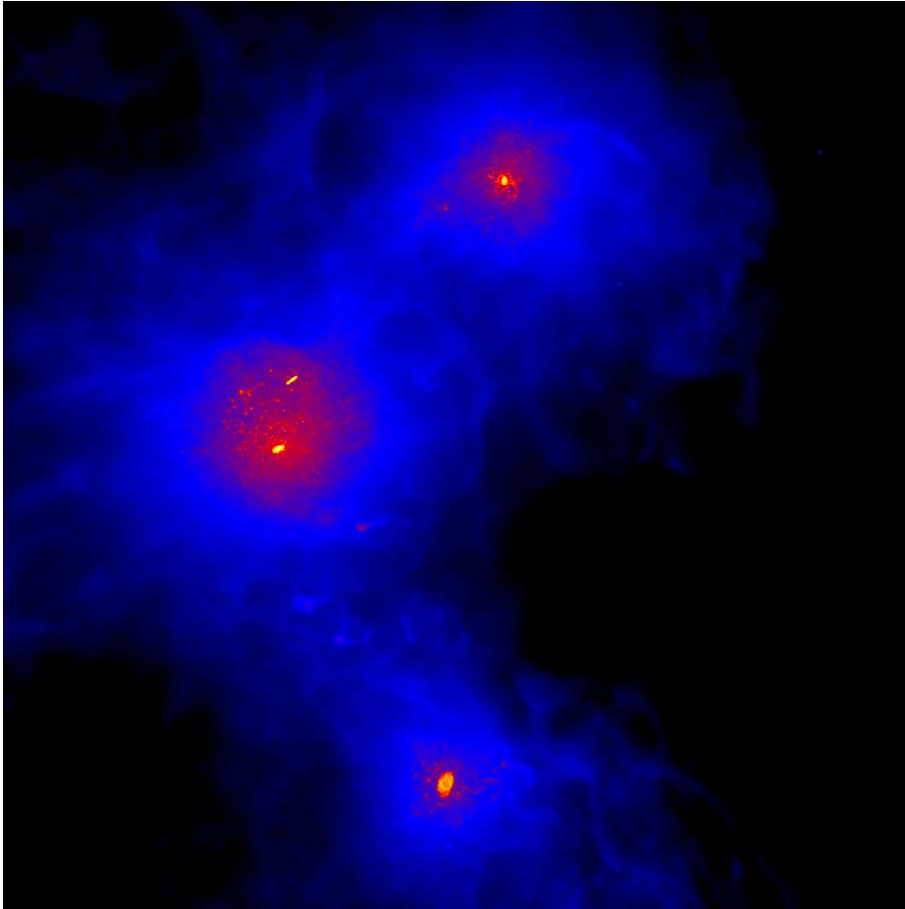


Figure 5.2: Projection of the three main halos (MW, M31, M33) along the z -direction, including the gas distribution. Image courtesy to the CLUES Project.

5.1.1 Testing theories

Since the constrained field description makes it possible to create different types of objects, it can be used as a laboratory to test and refine theories. An example of such is the ZOnes Bordering On Voidness technique by Neyrinck (2008). This method is an answer to increasing studies of voids, but the lack of definitions in this field. There is no predetermined shape for a void and by the theory of void mergers, there will be no definite shape. A problem is then to find voids in a simulations. Neyrinck developed a method, free from parameters, which should find voids in a particle distribution. Here voids are treated as underdense regions with a surrounding depression. By calculating a statistical significance for each found void, a physical interpretation can be made. Since observational effects makes it impossible to apply this method to real data, it was tested and refined using constrained simulations. A result of one of this test runs can be seen in figure 5.3. Other theories using constrained N-body simulations for test runs and refining are for example structure functions to obtain quantitative measures of large scale structure done by Babul & Starkman (1992) or the Watershed Void Finder by Platen *et al.* (2007).

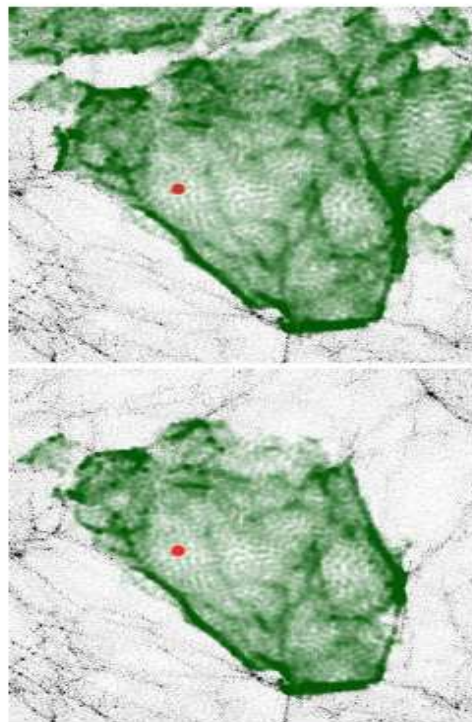


Figure 5.3: ZOBOV method applied to the Millennium Simulation. The particles are colored green when they belong to the void and black when they are not. The red dot is the absolute density minimum found. In the lower plot a correction was made for subvoids. Image courtesy to Neyrinck (2008)

5.2 Local Universe

The formation of particular structural features within a specific cosmological context can also be studied on large scales. By creating initial conditions to suite a specific region of the universe, the formation of the (large scale) structure can be studied.

Ganon & Hoffman (1993) were the first to apply the constrained field formalism as instrument in an attempt to create initial conditions resembling our Local Group. The constraints in this simulation were retrieved from the POTENT method (Dekel *et al.*, 1990), where the smoothed velocity potential was sampled on a finite number of positions to create a set of numerical values. The unconstrained realization, from which the residual field was sampled, was completely determined the SCDM cosmology power spectrum. (Blumenthal, 1984) The simulation was done on a three-dimensional cubic lattice with 32^3 grid points with a spacing of $5h^{-1} Mpc$. The obtained constrained density fields were smoothed with different smoothing radii and some of the results can be seen in figure 5.4. Here the unconstrained realization is shown in the upper left panel, together with two constrained realizations smoothed on different radii and the reference density field as obtained with POTENT in the most lower right panel.

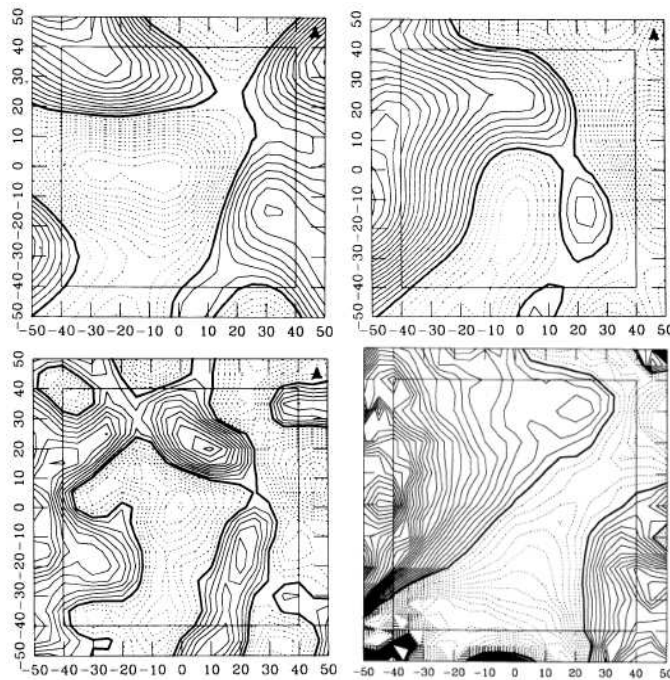


Figure 5.4: Realizations by Ganon & Hoffman (1993). From left to right, from up till down, an unconstrained realization with the Standard Cold Dark matter model, a constrained realization with the constraints on the velocity potential obtained by POTENT, smoothed on a scale of $5h^{-1} Mpc$, a constrained realization with the constraints on the velocity potential obtained by POTENT, smoothed on a scale of $12h^{-1} Mpc$ and a density field as obtained by velocity potential obtained by POTENT.

The simulation was done for different residual fields. Ganon & Hoffman (1993) noted that although the unconstrained random realizations differed considerably, the resulting maps were very similar. This means that the fluctuations in the power spectrum are particularly small with respect to the over- and underdensities in the simulation.

Present-day projects

Nowadays, various project groups recreate our Local Universe at high resolutions for different purposes. In these simulations, the different structures of the surroundings of the Milky Way can be recognized and their evolution and formation can be studied. One of the projects accomplishing this is CLUES, which stands for Constrained Local UniversE Simulations. The goal of the project is provide constrained simulations of the universe which can be used as a laboratory for astronomers. From constrained initial conditions, the formation and evolution of the the Milky Way, Andromeda Galaxy and twenty-eight other galaxies is simulated using different cosmological parameters, all based on different WMAP estimates. (Gottlober *et al.*, 2009) One of the realizations of the simulation results can be found in figure 5.5, where a slice of the large scale dark matter distribution of the Local Universe is shown. In the center of the simulation the Milky Way is situated, surrounded by the Virgo-Cluster, the Coma-cluster and the Great Attractor, all connected via the filaments and walls of the Cosmic Web.

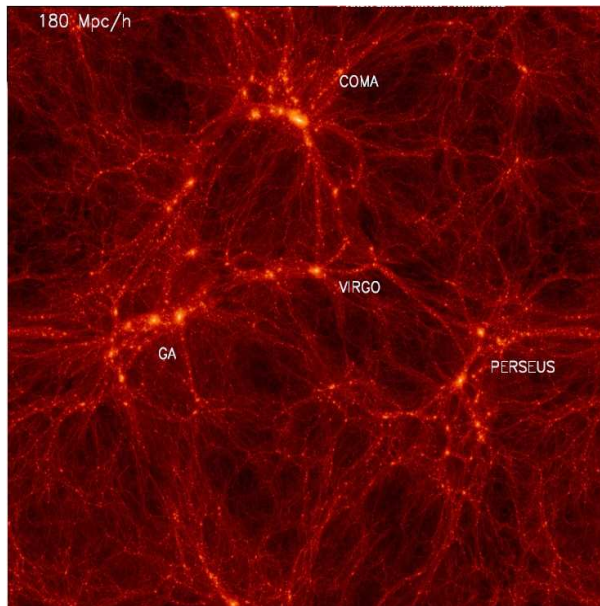


Figure 5.5: Large scale dark matter density distribution of the Local Universe. The image shows a slice through the center of the simulation box. The box size is equal to $180h^{-1} Mpc$ and the number of particles is equal to 1024^3 . Our galaxy can be found in the center of the simulation box. Image courtesy to the CLUES Project.

Another project to study the evolution and formation of large scale structure is the simulation by Springel *et al.* (2005), where the large scale structure of our Local Group was simulated. A few years later, the simulation was done again, but in a smaller simulation box to create a higher resolution. The results were checked by running another simulation with the same initial conditions and fewer particles to check that features in the higher-resolution run were also seen at lower resolution. One of the many simulation results can be found in figure 5.6, where the Local Universe is simulated. The Local Group can be found in the center of the simulation, while the Great Attractor is found on the left and the Cetus Wall on the lower right.

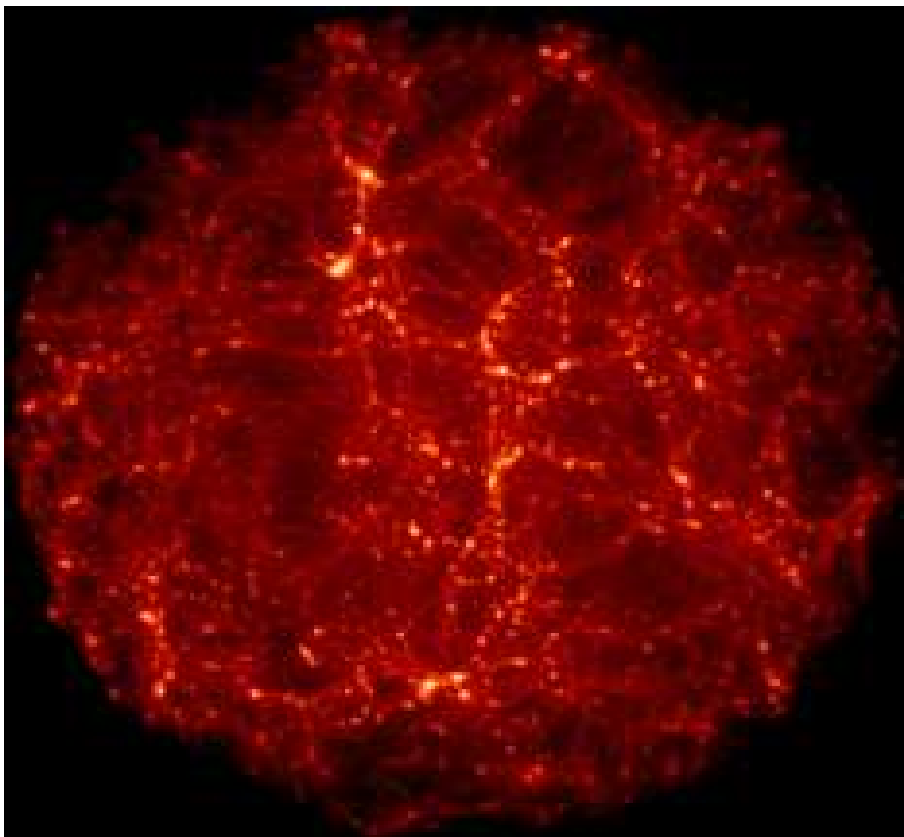


Figure 5.6: This visualization shows our "Local Universe", as simulated in the constrained realization project. The Local Group is in the center of the sphere. In the initial orientation of the sphere, the Great Attractor is on the left, and the Cetus Wall on the lower right. Image courtesy to Springel *et al.* (2005) and the Max-Planck-Institute for Astrophysics

5.2.1 Reconstruction method

The main approach of generating specified initial conditions for large scale structure N-body simulations is setting up a constrained realization and compare this with the observations done. This method requires assumptions about the power spectrum and several cosmological parameters, such as the Hubble parameter and the matter content of the universe. Methods were thought of to neutralize all the assumption made by the user. One of these methods is called the reconstruction method. In this method, an observed galaxy distribution is extrapolated back in time using different evolution theories to obtain the initial conditions in the same region of space. These results are then evolved using N-body simulation and by comparing the results, a better understanding of the cosmological model can be obtained.

Narayanan & Weinberg (1998) combined the best features of earlier done research to create the hybrid reconstruction method. By extrapolating the gravitational potential backwards in time, the initial density field can be recovered via the Poisson equation. When these conditions are now again evolved, assumptions about galaxy biasing, a value for the parameter Ω and shape of the power spectrum are implicitly done. By comparing the simulations realizations with the observations, these parameters can be estimated. A realization from Narayanan & Weinberg (1998) is found in figure 5.7, where in left panel the true initial conditions can be found and in the right panel the initial conditions are shown derived with the hybrid reconstruction method.

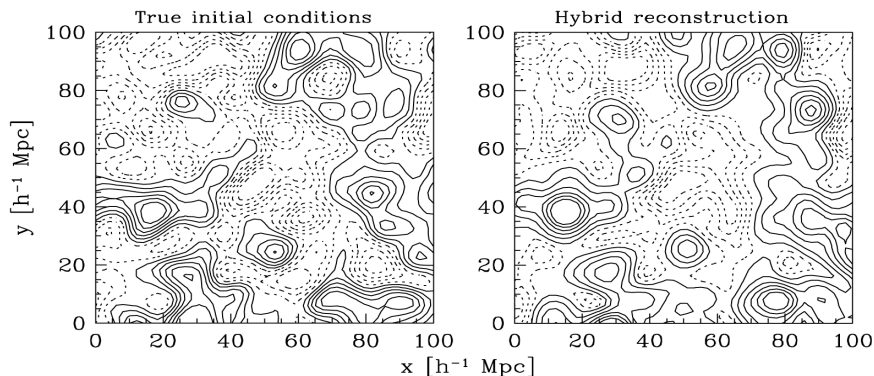


Figure 5.7: Demonstration of the hybrid reconstruction method. In the left panel, the true initial conditions are shown. The right panel contains the initial conditions derived with the hybrid reconstruction. Both realizations are smoothed with a Gaussian filter with a smoothing radius of $3h^{-1} Mpc$.

5.2.2 Extra Galactic Magnetic Field

Not only the structure formation within a cosmological model can be tested: the study can be extended to all variables who are believed to have a cosmological origin. An example is the distribution of the Extra Galactic Magnetic Field (EGMF), which is of particular interest in the study of the search of the origin of Ultra High Energy Cosmic Rays (UHECRs).

Cosmic Ray theory

UHECRs are particles or nuclei originating from an astronomical source, moving with a kinetic energy comparable to or higher than the Greisen-Zatsepin-Kuzmin limit, which is a theoretical upper limit on the energy of a cosmic ray from a distant source due to interaction with the CMB. (Greisen, 1966), (Zatsepin & Kuzmin, 1966)

Since the flux of cosmic rays is low, they can only be observed when they interact, for example when they enter the earth's atmosphere. Here they will collide with the molecules, producing a cascade of secondary lighter particles, called an air shower. An example of such a shower is shown at figure 5.8, where the different colors stand for different particles. These air shower particles are the ones which can be detected at earth.

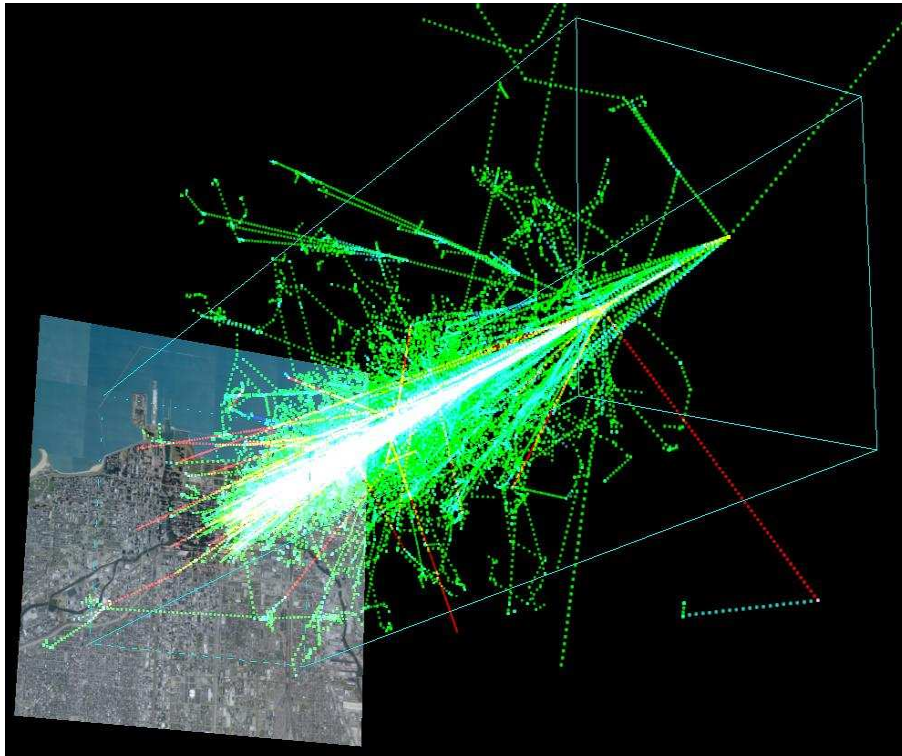


Figure 5.8: Cosmic ray air shower created by a 1TeV proton hitting the atmosphere 20 km above the Earth. Image Courtesy to the ARES project.

By studying air showers, the nature, direction and the energy of the primary

particle can be determined. The primary particle is believed to be a proton or a light nuclei of cosmic origin, since restrictions were made on the fraction of photons [Ave *et al.* (2002)] and the discovered preference for high energy air showers for light nuclei. (Bird *et al.*, 1993). So the primary particle is most likely a charged particle, it is difficult to track the cosmological source, since its path through the universe will be deflected by the EGMF. By studying the strength and the geometry of the EGMF, a better understanding of the angular distribution of air showers and the deflection of UHECRs is created. Since the EGMF is believed to have a cosmological origin and will have evolved over time under the influence of structure formation, N-body simulations are a perfect instrument to study its evolution. (Kronberg *et al.*, 1999)

Simulations

The first numerical studies on the evolution EGMF combined the magneto-hydrodynamics of the magnetized interstellar medium with the gravitational evolution of dark matter. (Dolag *et al.*, 1999), (Dolag *et al.*, 2002), (Ryu *et al.*, 1998), (Sigla *et al.*, 2003) Since the EGMF can only be observed by Faraday rotation in galaxy clusters, the simulation results and observational results are compared in these areas. Using this method, an appropriate evolution scenario for the EGMF could be found. The problems were varied in the different researches, but one common problem was discovered. In relative underdense regions compared with galaxy clusters, such as filaments or voids, the EGMF can only be found by extrapolating the data from overdense regions. This is not an accurate way to describe the geometry and strength in these underdense regions, where there is little to no data found on the EGMF.

Dolag *et al.* (2004) was the first to make use of constrained realizations. The initial conditions for the dark matter density distribution were constrained to reproduce the large scale structure around the Milky Way. The approach and the data were copied from Mathis *et al.* (2002). Here observations from the IRAS 1.2-Jy galaxy survey were smoothed and evolved linearly back in time to be used as Gaussian constraints as proposed by the Hoffman-Ribak method. This constrained realization was showed to be a appropriate initial set to obtain the large scale structure of the universe within 110 *Mpc* of the Milky Way. Advantages of the constrained field formalism in this field is that the scientist is not forced to choose an observer position, making it possible to create all-sky maps of deflection. To check whether this model is suitable, again the Faraday rotation within the simulation and observed galaxy clusters are compared. When they are in agreement, the evolution of the EGMF is quite good simulated and its geometry and strength in underdense regions should be a good representation of the truth.

The simulation was done twice with different strength and orientation of the magnetic field. The results are presented in Dolag *et al.* (2004) and Dolag *et al.* (2005). By studying the complete EGMF, an associated map of particle deflections is constructed. (see figure 5.9) These maps show that the EGMF in voids, filaments and sheets have negligible influence in deflecting the path of a high energetic particle. Even the crossing of a galaxy cluster adds such a minor deflection to the trajectory that identifying the cosmological source becomes a reality.

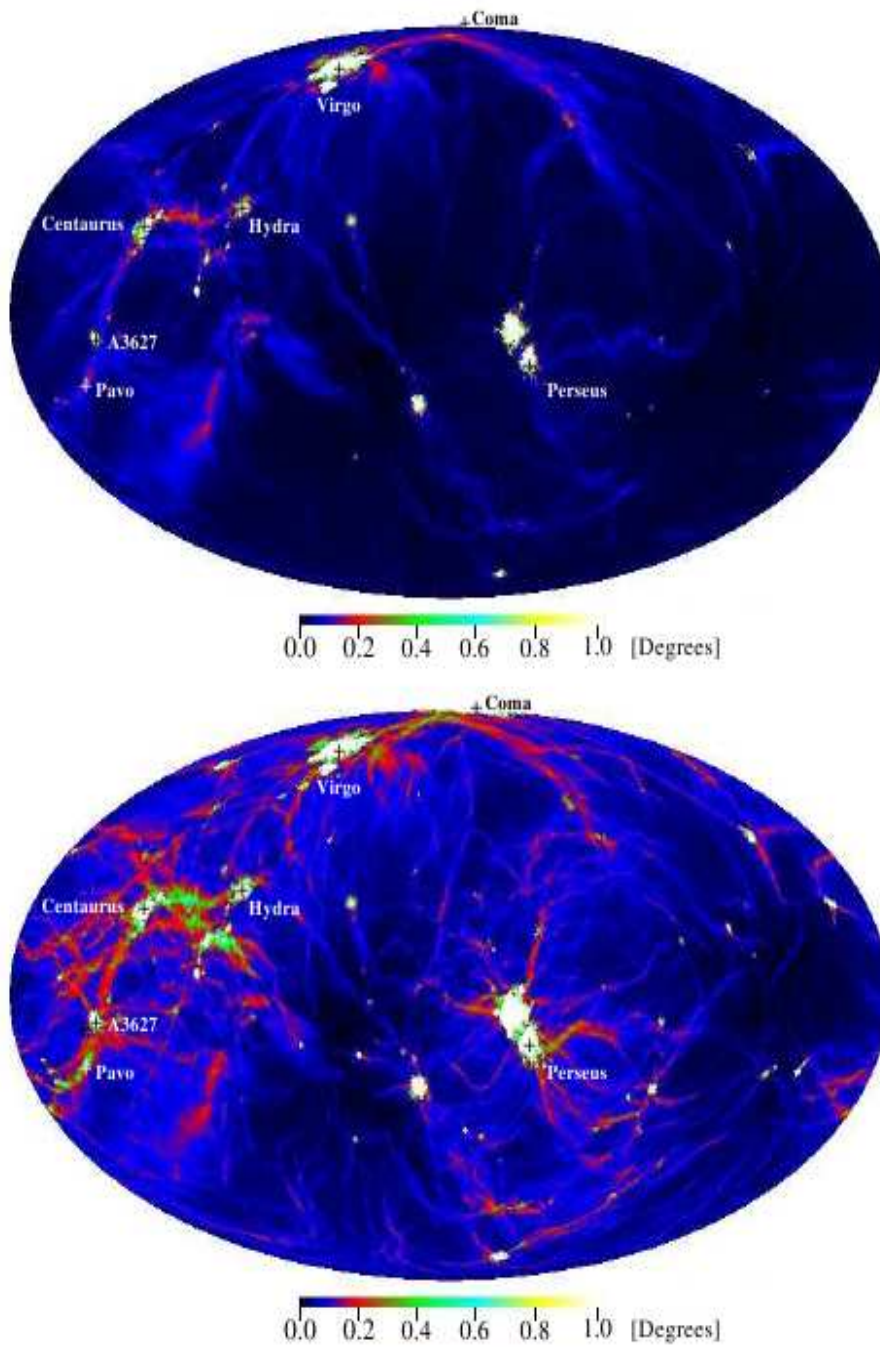


Figure 5.9: Full sky maps of expected deflection angles for protons with the arrival energy $E = 1 \times 10^{20}$ eV. The simulation is stationed within a 100 Mpc around the Milky Way and in the lower panel, energy losses due to interaction with the CMB are neglected. Image courtesy to Dolag, Grasso, Springel and Tkachev.

The obtained numerical results are used when observational data is interpreted, in search for the source of cosmic rays. The Pierre Auger Southern Observatory in Argentina is built to study simultaneously the direction and energy of the primary particle. The sixteen hundred ground detectors, covering an area of three thousand square kilometers, detect the Cherenkov radiation the secondary particles produce in water. This gives an indication of the nature of the primary particle and its arrival direction. The four complementary sites of six optical telescopes measure atmospheric fluorescence light produced by the air shower.

Sources of the cosmic rays have to be within 200 Mpc of the earth due to the GZK-effect. By observing the directions and energy of the cosmic rays, an anisotropic distribution is found. A correlation was found between the arrival directions of cosmic rays and positions of nearby Active Galactic Nuclei, suggesting that these are the most likely candidate for being the cosmological source of cosmic rays.

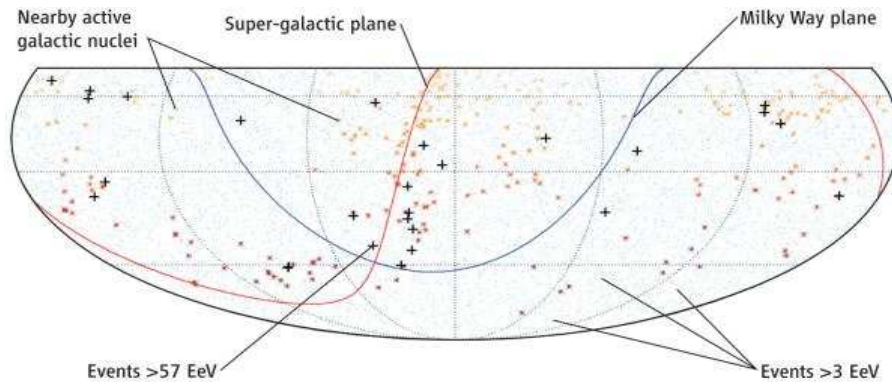


Figure 5.10: Sky map showing the detected air shower events by the Pierre Auger observatory. Low energy cosmic rays appear to originate from evenly distributed sources (blue dots), while the high energetic cosmic rays (crosses) show a correlation with the distribution of Active Galactic Nuclei (red stars). This is an indication that AGN's are a likely source for high energetic cosmic rays. Image Courtesy to the Pierre Auger collaboration (2004).

Chapter 6

Summary and Discussion

The gravitational instability scenario states that the large scale structure in the universe grew under the influence of gravity from primordial density and velocity perturbations. These perturbation fields are believed to be Gaussian and can be used as initial conditions for N-body simulations to study the formation and evolution of different types of structures. In order to generate a specific structure, user-specified initial conditions are desired. This can be done by imposing numerical values on the Gaussian random field and is called Constrained Field Formalism.

Various methods are proposed to generate constrained realizations. In this project, the main focus lies on the description of Bertschinger (1987) who was the first one to realize the importance of constrained realizations. He stated that a constrained realization could be created by adding a mean field $\bar{f}(\mathbf{x})$, which is defined as the ensemble average of all fields obeying the desired set of constraints, and the residual field $F(\mathbf{x})$, containing the random fluctuations of the power spectrum.

$$f(\mathbf{x}) = \bar{f}(\mathbf{x}) + F(\mathbf{x}) \quad (6.1)$$

The imposed set of constraints were assumed to be linear functionals of the field itself.

Hoffman & Ribak (1991) realized that when the imposed constraints are linear functionals if the field itself, the statistics of the residual field are independent of the numerical values of the imposed constraints, so that the residual field can be sampled from any realization. This reduces the computational cost considerably, making the method suitable for a large number of constraints. A constrained realization can then be written as: (van de Weygaert & Bertschinger, 1996)

$$f(\mathbf{x}) = \int \frac{d\mathbf{k}}{(2\pi)^3} [\tilde{f}(\mathbf{k}) + P(k)\hat{H}_i(\mathbf{k})\xi_{ij}^{-1}(c_j - \tilde{c}_j)]e^{i\mathbf{k}\cdot\mathbf{x}} \quad (6.2)$$

In this realization, $\tilde{f}(\mathbf{k})$ is the mean field of a random realization from which the constraints are calculated, $P(k)$ is the power spectrum, $\hat{H}_i(\mathbf{k})$ is a kernel containing a Gaussian filter with a constraint-specified factor, ξ_{ij}^{-1} is the constraint correlation matrix, c_j is the set of constraints specified by the user and \tilde{c}_j is the set of constraints found in a random realization.

The Hoffman-Ribak method is applied in various projects: re simulating the

large scale structure to test different cosmological models (Ganon & Hoffman, 1993) or studying a specific object to gain insight in the evolution processes. (van de Weygaert & van Kampen, 1993) As an example of the latter, the constrained peak formalism is studied in this research. By specifying up to eighteen constraints per over- or underdensity, the initial local density perturbation and peculiar velocity fields can be specified. This will influence the evolution of the initial conditions in the N-body simulation.

The constrained realization based on the constrained peak formalism are explored. The computational implementation is used to create user specified initial conditions for N-body simulations to form walls, filaments, peaks and voids. The simulations were done on a periodic cubic three dimensional lattice with a size of $L = 100h^{-1} Mpc$ and a number of particles equal to 256^3 . Because of the periodic boundary conditions, the average density of the simulation box must be equal to the average density of the universe. This is a large disadvantage of this method, since the generated constrained realization will not always provide us with a realistic image. For certain extreme constraints, an overdense region will always be surrounded by an underdense region. This will then naturally influence the evolution of a specified structure. An example of such a situation can be found in figure 6.1. There are always other limitations when using a simulation, such as the scale of the object with respect to the size of the simulation box.

Extrema

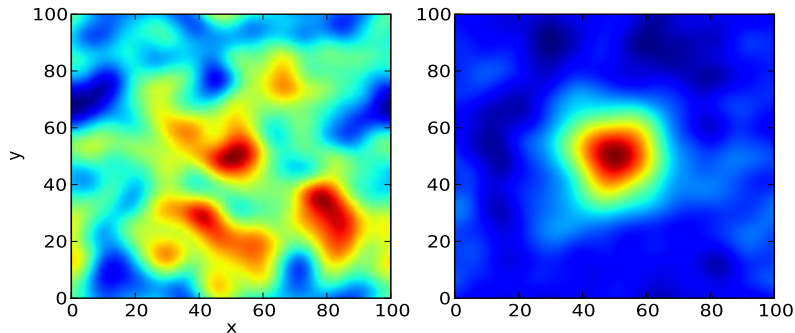


Figure 6.1: Extreme numerical constraints will ensure that overdense regions are surrounded by underdense regions in the Hoffman-Ribak method. Notice that blue is the underdense region, while red is the overdense region.

The Hoffman-Ribak method is based on the assumption that the perturbation fields are Gaussian distributed. But on small scales, the density distribution is believed to be lognormal. (Sheth *et al.*, 1994) Sheth (1995) solved this problem

by defining a new field as the natural logarithm of the density field, ensuring its Gaussianity and making it again applicable for the Hoffman-Ribak method.

The main advantage of the Hoffman-Ribak method is that it is applicable to construct a constrained realization subject to a large number of constraints. Because all constraints are linear convolutions with the density field, implementation in Fourier space is straightforward, keeping the algorithm quite efficient. Efficiency is true for more algorithms, such as the proposed change of coordinate system by Binney & Quinn (1991). By writing the density fields into spherical coordinates, a formalism was set up appropriate for studying galaxy- and cluster formation.

$$f(\mathbf{x}) = \sqrt{\frac{2}{\pi}} \kappa_n f_{lm}(k_n) j_l(k_n r) Y_l^m(\theta, \phi) \quad (6.3)$$

An advantage of this choice of coordinate system is the possibility to implement constraints on the angular momentum. Just as for the Hoffman-Ribak method, artificial boundary conditions are induced, imposing again the requirement that the average density of the simulation box is equal to the average density of the universe. A major disadvantage of the Binney-Quinn method over the HR-method is the fact that it is only suitable for a local set of constraints, containing an obvious center of symmetry.

Other methods are thought of to create constrained realizations. Salmon (1996) used the technique of Frenk *et al.* (1985), where a Gaussian random field was created as the convolution of white noise with a filter, defined as the square root of the power spectrum. By imposing constraints on a Gaussian random field, a new Gaussian field is created with different mean and variance. Salmon (1996) noticed that by filtering a Gaussian random field with a specific filter, a new Gaussian random field appeared with the same mean and variance as the constrained realization. Since Gaussian fields are determined by their statistics, the two obtained fields are indistinguishable. The advantage of this method is the use of white noise. Since this is uncorrelated in real space, the convolution does not have to be calculated in Fourier space. Omitting an FFT makes the algorithm computationally faster and suitable for a large number of constraints. Also the grid points do not have to be evenly spaced without an FFT, making the method suitable for adaptive mesh refinement.

All the methods described above have their advantages and their problems. But all methods described above can generate constrained realizations, which gain insight in the formation and evolution of structure after evolution. One last, colorful result of constrained realizations can be found in figure 6.2.

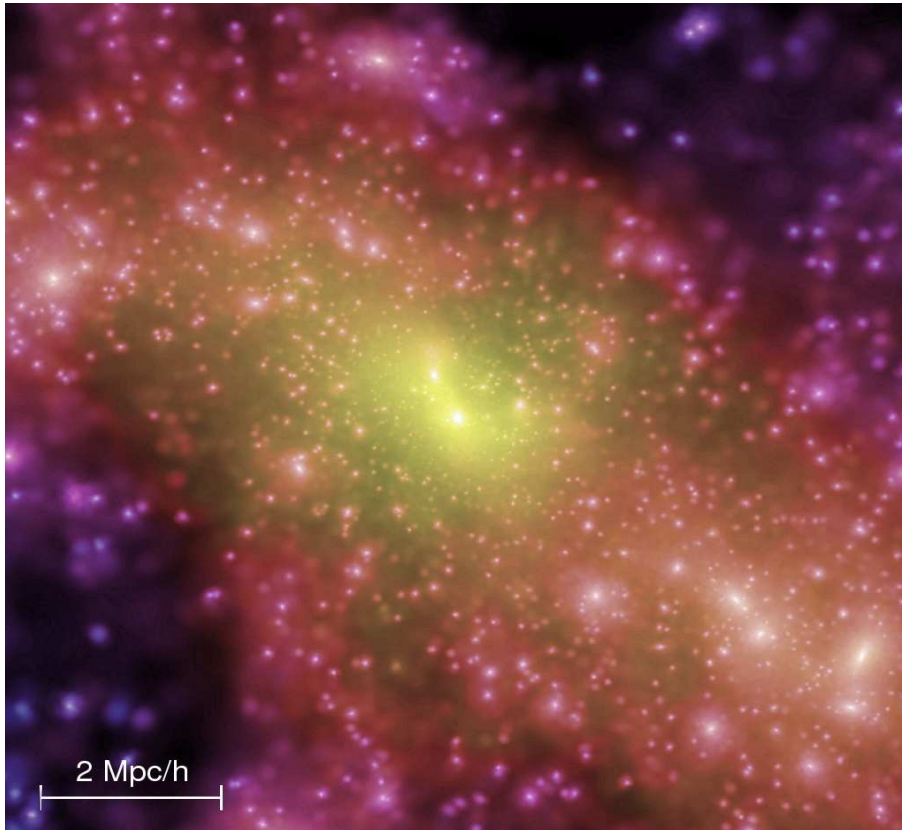


Figure 6.2: Dark matter distribution within a galaxy. The image shows a slice through the center of the simulation box. Image courtesy to the Millenium Project.

Bibliography

- Ave, M., Hinton, J.A., Vazquez, R.A., Watson, A.A., & Zas, E. 2002. Physical review d, vol. 65, issue 6, id. 063007. *Constraints on the ultrahigh-energy photon flux using inclined showers from the haverah park array.*
- Babul, A., & Starkman, G.D. 1992. Astrophysical journal, part 1 (issn 0004-637x), vol. 401, no. 1, p. 28-39. *A quantitative measure of structure in the three-dimensional galaxy distribution - sheets and filament.*
- Bardeen, J.M., Bond, J.R., Kaiser, N., & Szalay, A.S. 1986. Astrophysical journal, part 1 (issn 0004-637x), vol. 304, p. 15-61. *The statistics of peaks in gaussian random fields.*
- Bertschinger, E. 1985. Astrophysical journal supplement series (issn 0067-0049), vol. 58, p. 39-65. *Self-similar secondary infall and accretion in an einstein-de sitter universe.*
- Bertschinger, E. 1987. Astrophysical journal, part 2 - letters to the editor (issn 0004-637x), vol. 323, p. 1103-1106. *Path integral methods for primordial density perturbations: sampling of constrained gaussian random fields.*
- Bertschinger, E. 2001. The astrophysical journal supplement series, volume 137, issue 1, pp. 1-20. *Multiscale gaussian random fields and their application to cosmological simulations.*
- Binney, J., & Quinn, T. 1991. Royal astronomical society, monthly notices (issn 0035-8711), vol. 249, p. 678-683. *Gaussian random fields in spherical coordinates.*
- Bird, D. J., Corbatp, S.C., Dai, H.Y., Dawson, B.R., Elbert, J.W., Gaiser, T.K., Green, K.D., Huang, M.A., D.B., Ko, S., Larsen, C.G., Loh, E.C., Luo, M., Salamon, M.H., Smith, D., Sokolsky, P., Sommers, P., Stanev, T., Tnag, J. L., Thomas, S.B., & Tilav, S. 1993. Physical review letters, volume 71, issue 21, november 22, 1993, pp.3401-3404. *Evidence for correlated changes in the spectrum and composition of cosmic rays at extremely high energies.*
- Blumenthal, G.R. 1984. Bulletin of the american astronomical society, vol. 16, p.918. *Dark matter in the universe: Astrophysical constraints and effects on galaxy formation.*
- Bond, J. R., Kofman, L., & Pogosyan, D. 1996. Nature, volume 380, issue 6575, pp. 603-606. *How filaments of galaxies are woven into the cosmic web.*

- Coles, P., & Jones, B. 1991. Royal astronomical society, monthly notices (issn 0035-8711), vol. 248, jan. 1, p. 1-13. *A lognormal model for the cosmological mass distribution.*
- de Lapparent, V., Geller, M.J., & Huchra, J.P. 1986. Astrophysical journal, part 2 - letters to the editor (issn 0004-637x), vol. 302,. *A slice of the universe.*
- Dekel, A., Bertschinger, E., & Faber, S.M. 1990. Astrophysical journal, part 1 (issn 0004-637x), vol. 364, dec. 1, 1990, p. 349-369. *Potential, velocity, and density fields from sparse and noisy redshift-distance samples - method.*
- Dolag, K., Bartelmann, M., & Lesch, H. 1999. Astronomy and astrophysics, p. 348-351. *Sph simulations of magnetic fields in galaxy clusters.*
- Dolag, K., Bartelmann, M., & Lesch, H. 2002. Astronomy and astrophysics, v.387, p.383-395. *Evolution and structure of magnetic fields in simulated galaxy clusters.*
- Dolag, K., Grasso, D., Springel, V., & Tkachev, I. 2004. Jetp letters, vol. 79, pp. 583-587, 2004; pisma zh. eksp. teor. fiz. 79: 719-723. *Mapping deflections of ultrahigh energy cosmic rays in constrained simulations of extragalactic magnetic fields.*
- Dolag, K., Grasso, D., Springel, V., & Tkachev, I. 2005. Journal of cosmology and astroparticle physics, issue 01, pp. 009,. *Constrained simulations of the magnetic field in the local universe and the propagation of uhecrs.*
- Evrard, A.E. 1990. Astrophysical journal, part 1 (issn 0004-637x), vol. 363, p. 349-366. *Formation and evolution of x-ray clusters - a hydrodynamic simulation of the intracluster medium.*
- Evrard, A.E., Silk, J., & Szalay, A.S. 1990. Astrophysical journal, part 1 (issn 0004-637x), vol. 365, p. 13-21. *The morphology-density relation for galaxies in a cold dark matter-dominated universe.*
- Evrard, A.E., Bialek, J., Busha, M., White, M., Habib, S., Heitmann, K., Warren, M., Rasia, E., Tormen, G., Moscardini, L., Power, C., Jenkins, A.R., Gao, L., Frenk, C.S., Springel, V., White, S.D.M., & Diemand, J. 2008. The astrophysical journal, volume 672, issue 1, pp. 122-137. *Virial scaling of massive dark matter halos: Why clusters prefer a high normalization cosmology.*
- Faber, S.M., & Burstein, D. 1988. Large-scale motions in the universe (a89-42951 18-90). princeton, nj, princeton university press, p. 115-167. *Motions of galaxies in the neighborhood of the local group.*
- Frenk, C.S., White, S.D., Efstathiou, G., & Davis, M. 1985. Nature (issn 0028-0836), vol. 317, oct. 17, 1985, p. 595-597. *Cold dark matter, the structure of galactic haloes and the origin of the hubble sequence.*
- Ganon, G., & Hoffman, Y. 1993. Astrophysical journal, part 2 - letters (issn 0004-637x), vol. 415, no. 1, p. l5-l8. *Constrained realizations of gaussian fields - reconstruction of the large-scale structure.*
- Geller, M.J., & Huchra, J.P. 1989. Science (issn 0036-8075), vol. 246, nov. 17, 1989, p. 897-903. *Mapping the universe.*

- Gottlober, S., Hoffman, Y., Yepes, G., & Martinez-Vaquero, L.A. 2009. 5th international workshop on the dark side of the universe, aip conference proceedings, volume 1178, pp. 64-75. *The clues project: Constrained local universe simulations.*
- Greisen, K. 1966. Phys. rev. lett. 16, 748- 750. *End to the cosmic ray spectrum?*
- Harrison, E.R. 1970. Physical review, volume 1, pp 2727-2730. *Fluctuations at the threshold of classical cosmology.*
- Hausman, M.A., Olson, D., & Roth, B.D. 1983. Astrophysical journal, part 1 (issn 0004-637x), vol. 270, p. 351-359. *The evolution of voids in the expanding universe.*
- Hoffman, G.L., Salpeter, E.E., & Wasserman, I. 1983. Astrophysical journal, part 1 (issn 0004-637x), vol. 268, p. 527-539. *Spherical simulations of holes and honeycombs in friedmann universes.*
- Hoffman, Y., & Ribak, E. 1991. Astrophysical journal, part 2 - letters (issn 0004-637x), vol. 380, p. 15-18. *Constrained realizations of gaussian fields: a simple algorithm.*
- Hoffman, Y., & Shaham, J. 1982. Astrophysical journal, part 2 - letters to the editor, vol. 262, nov. 15, 1982, p. 123-126. *On the origin of the voids in the galaxy distribution.*
- Horizonproject. <http://www.projet-horizon.fr>.
- Icke, V. 1984. Royal astronomical society, monthly notices (issn 0035-8711), vol. 206, p. 1p-3p. *Voids and filaments.*
- Ikeuchi, S., & Umemera, M. 1984. Progress of theoretical physics, vol. 72, no. 2, pp. 216-232. *Nonlinear growth of density contrast and formation of galaxies in a neutrino-dominated universe.*
- Klypin, A., Hoffman, Y., Kravtsov, A.V., & Gottlober, S. 2003. The astrophysical journal, volume 596, issue 1, pp. 19-33. *Constrained simulations of the real universe: The local supercluster.*
- Knuth, D.E. 1981. Second edition volume 2 of the art of computer programming. *Seminumerical algorithms.*
- Komatsu, E., Dunkley, J., Nolte, M.R., Bennet, C.L., Gold, B., Hinshaw, G., Jarosik, N., Larson, D., Limon, M., Page, L., Spergel, D.N., Halpern, M., Hill, R.S., Kogut, A., Meyer, S.S., Tucker, G.S., and W. Wollack, J.L. Weiland, & Wright, E.L. 2009. The astrophysical journal supplement, volume 180, issue 2, pp. 330-376. *Seven-year wilkinson microwave anisotropy probe observations: Cosmological interpretation.*
- Kronberg, P.P., Lesch, H., & Hopp, U. 1999. The astrophysical journal, volume 511, issue 1, pp. 56-64. *Magnetization of the intergalactic medium by primeval galaxies.*

- Lahav, O., Lilje, P.B., Primack, J.R., & Rees, M.J. 1991. Royal astronomical society, monthly notices (issn 0035-8711), vol. 251, p. 128-136. *Dynamical effects of the cosmological constant.*
- Mathis, H., Lemson, G., Springel, V., Kauffmann, G., White, S.D.M., Eldar, A., & Dekel, A. 2002. Monthly notices of the royal astronomical society, volume 333, issue 4, pp. 739-762. *Simulating the formation of the local galaxy population.*
- Mezler, C.A., & Evrard, A.E. 1994. Astrophysical journal, part 1 (issn 0004-637x), vol. 437, no. 2, p. 564-583. *A simulation of the intracluster medium with feedback from cluster galaxies.*
- Narayanan, V.K., & Weinberg, D.H. 1998. The astrophysical journal, volume 508, issue 2, pp. 440-471. *Reconstruction analysis of galaxy redshift surveys: A hybrid reconstruction method.*
- Neyrinck, M.C. 2008. Monthly notices of the royal astronomical society, volume 386, issue 4, pp. 2101-2109. *Zobov: a parameter-free void-finding algorithm.*
- Oort, J.H. 1983. Annual review of astronomy and astrophysics. volume 21 (a84-10851 01-90). palo alto, ca, annual reviews, inc., p. 373-428. *Superclusters.*
- Peebles, P.J.E. 1980. Princeton university press. *The large scale structure of the universe.*
- Peebles, P.J.E. 1982. Astrophysical journal, part 1, vol. 257, p. 438-441. *The peculiar velocity around a hole in the galaxy distribution.*
- Peebles, P.J.E., & Yu, J.T. 1970. Astrophysical journal, volume 162, pp 815-836. *Primeval adiabatic perturbation in an expanding universe.*
- Pen, U. 1997. Astrophysical journal letters v.490, p.1127. *Generating cosmological gaussian random fields.*
- Platen, E., van de Weygaert, R., & Jones, B.J.T. 2007. Monthly notices of the royal astronomical society, volume 380, issue 2, pp. 551-570. *A cosmic watershed: the wvf void detection technique.*
- Press, W.H., Vetterling, W.T., Teukolsky, S.A., & Flannery, B.P. 1992. Second edition, p.273, cambridge university press. *Numerical recipes in fortran: the art of scientific computing.*
- Prunet, S., Pichon, C., Aubert, D., Pogosyan, D., Teyssier, R., & Gottloeber, S. 2008. The astrophysical journal supplement series, volume 178, issue 2, pp. 179-188. *Initial conditions for large cosmological simulations.*
- Romano-Diaz, E., Shlosman, I., & an Y. Hoffman, C. Heller. 2009. The astrophysical journal, volume 702, issue 2, pp. 1250-1267. *Dissecting galaxy formation. i. comparison between pure dark matter and baryonic models.*
- Romano-Diaz, E., Shlosman, I., & an Y. Hoffman, C. Heller. 2010. eprint arxiv:1002.4200. *Dissecting galaxy formation: Ii. comparing substructure in pure dark matter and baryonic models.*

- Ryu, D., Kang, H., & Biermann, P.L. 1998. *Astronomy and astrophysics*, v.335, p.19-25. *Cosmic magnetic fields in large scale filaments and sheets.*
- Salmon, J. 1996. *Astrophysical journal* v.460, p.59,. *Generation of correlated and constrained gaussian stochastic processes for n-body simulations.*
- Scherrer, R.J. 1992. *Astrophysical journal*, volume 384, pp 391-395. *Cosmological explosions from cold dark matter pertubations.*
- Sheth, R.K. 1995. Constrained realizations and minimum variance reconstruction of non-gaussian random fields.
- Sheth, R.K., Mo, H.J., & Saslaw, W.C. 1994. *Astrophysical journal*, part 1 (issn 0004-637x), vol. 427, no. 2, p. 562-573. *The distribution of iras galaxies on linear and nonlinear scales.*
- Sigla, G., Miniati, F., & Ensslin, T. 2003. *Physical review d*, vol. 68, issue 4, id. 043002. *Ultrahigh energy cosmic rays in a structured and magnetized universe.*
- Springel, V., White, S.D.M., Jenkins, A., Frenk, C.S., Yoshida, N., Gao, L., Navarro, J., Thacker, R., Croton, D., Helly, J., Peacock, J.A., Cole, S., Thomas, P., an A. Evrard, H. Couchman, Colberg, J., & Pearce, F. 2005. *Nature* 435, 629-636. *Simulations of the formation, evolution and clustering of galaxies and quasars.*
- Sugiyama, N. 1995. *Astrophysical journal supplement* v.100, p.281. *Cosmic background anistropies in cold dark matter cosmology.*
- van de Weygaert, R., & Bertschinger, E. 1996. *Monthly notices of the royal astronomical society*, vol. 281, p. 84. *Peak and gravity constraints in gaussian primordial density fields: an application of the hoffman-ribak method.*
- van de Weygaert, R., & van Kampen, E. 1993. *R.a.s. monthly notices*, volume 263, no.2, p.481. *Voids in gravitational instability scenarios - part one - global density and velocity fields in an einstein - de-sitter universe.*
- van Haarlem, M., & van de Weygaert, R. 1993. *Astrophysical journal* v.418, p.544. *Velocity fields and alignments of clusters in gravitational instability scenarios.*
- Zatsepin, G.T., & Kuzmin, V.A. 1966. *Journal of experimental and theoretical physics letters* 4, 7880. *Upper limit of the spectrum of cosmic rays.*
- Zel'dovich, Ya.B. 1970. *Astronomy and astrophysics*, volume 5, pp 384-89. *Gravitational instability: an approximate theory for large density pertubations.*

Appendix A

Linear evolution of perturbation fields

When describing the evolution of the structure of the universe, it is preferred to specify the evolution of the fluctuations in quantities that deviate from the background. It is therefore more convenient to work in comoving coordinates, so that the comoving position of an object becomes:

$$\mathbf{x}(t) = \frac{\mathbf{r}(t)}{a(t)} \quad (\text{A.1})$$

in which $a(t)$ is the expansion factor of the universe and chosen so that $a(t_0) = 1$ for t_0 being the present epoch.

On large scales the matter and radiation content of the universe can be considered to be a continuous fluidum. Evolution of a fluid is dictated by the three fluid equations: the continuity equation, describing the conservation of mass, the Euler equation, describing the acceleration of the fluid elements and the Poisson equation, specifying the sources of the gravitational field and thereby coupling the density and the gravitational potential perturbation field. The fluid equations in comoving coordinates of matter perturbations:

$$\frac{\partial \mathbf{v}}{\partial t} + \frac{1}{a}(\mathbf{v} \cdot \nabla)\mathbf{v} + \frac{\dot{a}}{a}\mathbf{v} + \frac{1}{a}\nabla\phi = 0 \quad (\text{A.2})$$

$$\frac{\partial f}{\partial t} + \frac{1}{a}\nabla(1+f)\mathbf{v} = 0 \quad (\text{A.3})$$

$$\nabla^2\phi = 4\pi G a^2 f \bar{\rho} \quad (\text{A.4})$$

In the case of small density and velocity perturbations, the higher order terms in the continuity and Euler equation, representing the nonlinear coupling terms, can be neglected. In that case, the set of fluid equations for matter perturbations in comoving coordinates can be linearized yielding:

$$\frac{\partial \mathbf{v}}{\partial t} + \frac{\dot{a}}{a}\mathbf{v} + \frac{1}{a}\nabla\phi = 0 \quad (\text{A.5})$$

$$\frac{\partial f}{\partial t} + \frac{1}{a}\nabla_x\mathbf{v} = 0 \quad (\text{A.6})$$

$$\nabla^2\phi = 4\pi G a^2 f \bar{\rho} \quad (\text{A.7})$$

A.1 Solutions

We will solve this for an universe containing of a cosmological constant, dark matter, baryonic matter and radiation with values consistent with the Λ CDM model.

A.1.1 Solution for density perturbations

In order to solve the linearized equations for perturbations in the density field, the time derivative of the linearized continuity equation is substituted in the divergence of the linearized Euler equation. Combining the result with the Poisson equation yields:

$$\frac{\partial^2 f}{\partial t^2} + 2\frac{\dot{a}}{a}\frac{\partial f}{\partial t} = 4\pi G f \bar{\rho} \quad (\text{A.8})$$

The result is a second-order partial differential equation in time alone. The solution can be split into a spatial component and a time component.

$$f(\mathbf{x}, t) = D_1(t)f_1(\mathbf{x}) + D_2(t)f_2(\mathbf{x}) \quad (\text{A.9})$$

in which $D_1(t)$ and $D_2(t)$ are the universal density growth factors for the linear evolution of density perturbations and $f_1(\mathbf{x})$ and $f_2(\mathbf{x})$ represent the corresponding spatial configuration of the cosmic primordial matter distribution. The first half of the solution is called the growing mode solution and the second half the decaying mode solution. The growth factors depend on the cosmological background and evolve according to:

$$\frac{\partial^2 D}{\partial t^2} + 2\frac{\dot{a}}{a}\frac{\partial D}{\partial t} = 4\pi G f \bar{\rho} \quad (\text{A.10})$$

Solving the above system for an universe with matter, radiation and a cosmological constant, the Hubble parameter is given by the following relationship:

$$H^2(t) = H_0^2[\Omega_{r,0}a^{-4} + \Omega_{m,0}a^{-3} + (1 + \Omega_0)a^{-2} + \Omega_{\Lambda,0}] \quad (\text{A.11})$$

By differentiating this expression once and twice and adding them, it is found:

$$\ddot{H} + 2H\dot{H} = H_0^2 H \left(3\frac{\Omega_{m,0}}{2a^3} + 4\frac{\Omega_{r,0}}{a^4} \right) \quad (\text{A.12})$$

$$\approx H_0^2 H \frac{3\Omega_{m,0}}{2a^3} \quad (\text{A.13})$$

$$\ddot{H} + 2H\dot{H} = 4\pi G H \rho_m \quad (\text{A.14})$$

This is also a second order differential equation with the solution in a spatial and a time component. This equation, describing the evolution of H , is multiplied by $D(t)$ and subtracted with $H(t)$ times the equation for $D(t)$, yielding:

$$D\ddot{H} - H\ddot{D} + 2H(D\dot{H} - H\dot{D}) = 0 \quad (\text{A.15})$$

Remembering that $H(t) = \dot{a}/a$, it is found:

$$a^2 \frac{d}{dt}(\dot{D}H - H\dot{D}) + \frac{da^2}{dt}(\dot{D}H - H\dot{D}) = 0 \quad (\text{A.16})$$

This results in the differential equation:

$$\frac{d}{dt} \left[a^2 H^2 \frac{d}{dt} \left(\frac{D}{H} \right) \right] = 0 \quad (\text{A.17})$$

with the solution yielding:

$$D(t) = H(t) \int \frac{dt}{a^2 H^2(t)} \quad (\text{A.18})$$

A.1.2 Gravitational potential perturbations

The density distribution and the gravitational potential distribution are coupled via the Poisson relation. (eq. A.7) Notice that when working in an universe with matter and a cosmological constant, the dark matter remains uniformly distributed and does not have to be taken into account. The gravitational potential can then be found by taking the integral over the Green's function.

$$\phi(\mathbf{x}, t) = -G\rho_m a^2 \int d\mathbf{x}' f_m(\mathbf{x}', t) \frac{1}{|\mathbf{x}' - \mathbf{x}|} \quad (\text{A.19})$$

where the integral is over comoving space. Since the integral contains the evolution of the density perturbations, the gravitational potential perturbations evolve according to an universal potential perturbation growth factor, which yields for the growing mode solution:

$$\phi(\mathbf{x}, t) = D_\phi(t) \phi_0(\mathbf{x}, t) = \frac{D(t)}{a(t)} \phi_0(\mathbf{x}, t) \quad (\text{A.20})$$

Since the peculiar gravitational acceleration is equal to the gradient of the gravitational potential perturbation, it evolves in the growing mode solution according to:

$$g(\mathbf{x}, t) = D_g(t) g_0(\mathbf{x}, t) = \frac{D(t)}{a^2(t)} g_0(\mathbf{x}, t) \quad (\text{A.21})$$

A.1.3 Velocity perturbations

In the linear regime, the peculiar velocity consists of a pure gradient potential flow:

$$\mathbf{v} = \mathbf{v}_{||} \quad (\text{A.22})$$

The relation between the peculiar gravitational acceleration and the peculiar velocity is found in the Poisson equation:

$$\nabla \cdot \mathbf{v} = -a \nabla \cdot \frac{\partial}{\partial t} \left(\frac{\nabla \phi}{4\pi G \bar{\rho} a^2} \right) \quad (\text{A.23})$$

$$= a \nabla \cdot \frac{\partial}{\partial t} \left(\frac{\mathbf{g}}{4\pi G \bar{\rho} a} \right) \quad (\text{A.24})$$

Because \mathbf{v} and \mathbf{g} are both gradients of the potential, they can be left out. The found relation between \mathbf{g} and the linear density growth factor is used to find:

$$\mathbf{v} = \frac{1}{D} \frac{dD}{dt} \left(\frac{\mathbf{g}}{4\pi G \bar{\rho}} \right) \quad (\text{A.25})$$

Notice that the peculiar velocity is directly and linearly proportional to the peculiar gravitational acceleration. The proportionality factor is:

$$\frac{1}{D} \frac{dD}{dt} = H(t) \frac{a}{D} \frac{dD}{da} \equiv Hf \quad (\text{A.26})$$

so we find:

$$\mathbf{v} = \frac{Hf}{4\pi G\bar{\rho}} \mathbf{g} \quad (\text{A.27})$$

From this relationship the growth factor for peculiar velocities in the growing mode solution can be derived:

$$D_v(t) = aD(t)Hf(\Omega_m) \quad (\text{A.28})$$

In the above equation, $f(\Omega_m)$ is defined as the dimensionless linear growth factor. Its first approximation was made by Peebles in 1980 and was found to be $f \approx \Omega_m^{0.6}$. Lahav *et al.* (1991) worked out this estimate for the dimensionless linear growth factor for an universe with matter and a cosmological constant:

$$f(\Omega_m, \Omega_\Lambda) \approx \Omega_m^{0.6} + \frac{\Omega_\Lambda}{70} \left(1 + \frac{\Omega_m}{2} \right) \quad (\text{A.29})$$

As can be seen, the dimensionless growth factor mainly depends only the matter content of the universe.

Appendix B

Defining most likely field

The set of constraints imposed on a Gaussian random field are incorporated in the action integral in the following way:

$$S[f] = \frac{1}{2} \int \int f(\mathbf{x}_1) K(\mathbf{x}_1 - \mathbf{x}_2) f(\mathbf{x}_2) d\mathbf{x}_1 d\mathbf{x}_2 - C^t \xi_{ij}^{-1} C \quad (\text{B.1})$$

where ξ_{ij} is the ij th element of the constraint correlation matrix, C is a vector containing the set of constraints, f is the density perturbation field and K is the inverse of the correlation matrix. The i th constraint $C_i(\mathbf{x}_i)$ can be written as a convolution with a delta Dirac function. Since the inverse correlation matrix K and the autocorrelation function are the inverse of each other, multiplication of these two create a Dirac delta function. Combining these two facts, one get the following equation.

$$C_i(\mathbf{x}_i) = \int d\mathbf{x}_1 \int d\mathbf{x}_2 \xi(\mathbf{x}_1) K(\mathbf{x}_1 - \mathbf{x}_2) C_i(\mathbf{x}_i - \mathbf{x}_2) \quad (\text{B.2})$$

In Fourier space the following definition is found, using the convolution theorem:

$$C_i(\mathbf{x}_i) = \int \frac{d\mathbf{k}}{(2\pi)^3} \hat{C}_i(\mathbf{k}) P(k) \hat{K}(\mathbf{k}_e^{-i\mathbf{k} \cdot \mathbf{x}_i}) \quad (\text{B.3})$$

where \hat{C}_i is the Fourier transform of C_i and is the Fourier transform of $\xi(\mathbf{x})$ and $\hat{K}(\mathbf{k})$ is the Fourier transform of $K(\mathbf{x})$. Studying the definition for the power spectrum by Bertschinger (eq. 2.29), a similar expression can be described for $P_i(\mathbf{k})$:

$$(2\pi)^3 \hat{P}_i(k_1) \delta_D(\mathbf{k}_1 - \mathbf{k}_2) = \langle \hat{C}_i(\mathbf{k}_1) \hat{f}^*(\mathbf{k}_2) \rangle \quad (\text{B.4})$$

Combining the two results for the power spectrum, a relation between the Fourier components of the constraint function and the density field can be found:

$$\hat{C}_i(\mathbf{k}) = \frac{\hat{P}_i(k)}{P(k)} \hat{f}(\mathbf{k}) \quad (\text{B.5})$$

Appendix C

Proof statistics residual field

Hoffman and Ribak realized that the entire conditional probability distribution function of the residual field was independent of numerical values of the constraint set Γ . This can be proven by choosing two constraint sets of equal size. The first is denoted by $\Gamma_1 = C_i[f : \mathbf{x}_i] = c_{1,i}$ for $i = 1, \dots, M$ and the second one is denoted by $\Gamma_2 = C_i[f : \mathbf{x}_i] = c_{2,i}$ for $i = 1, \dots, M$. The mean fields of the sets are denoted by $\bar{f}_1(\mathbf{x})$ and $\bar{f}_2(\mathbf{x})$. Now a random field $f_1 \in \Gamma_1$ is chosen and translated by a field $T_{2,1}(\mathbf{x})$ into the field $f_T(\mathbf{x})$:

$$f_T(\mathbf{x}) = f_1(\mathbf{x}) + T_{2,1}(\mathbf{x}) \quad (\text{C.1})$$

where

$$T_{2,1} \equiv \bar{f}_2(\mathbf{x}) - \bar{f}_1(\mathbf{x}) = \xi_i(\mathbf{x})\xi_{ij}^{-1}(c_{j,2} - c_{j,1}) \quad (\text{C.2})$$

This implies that the mean field $\bar{f}_1(\mathbf{x})$ is transformed into the mean field $\bar{f}_2(\mathbf{x})$. By restricting the constraints to be linear;

$$C_i[f_1 + f_2; \mathbf{x}] = C_i[f_1; \mathbf{x}] + C_i[f_2; \mathbf{x}] \quad (\text{C.3})$$

the obeyed constraint set for the new field f_T can be recognized as Γ_2 . This is true regardless of the chosen field $f_1(\mathbf{x}) \in \Gamma_1$. By noting that the inverse translation transforms the field $f_2(\mathbf{x})$ back into $f_1(\mathbf{x})$, it is found that:

$$P[f_1 | \Gamma_1] = P[f_2 | \Gamma_2] \quad (\text{C.4})$$

The conditional probabilities for the corresponding residual fields are equal to:

$$P[F_1 | \Gamma_1] = P[f_1 | \Gamma_1] = P[f_2 | \Gamma_2] = P[F_2 | \Gamma_2] \quad (\text{C.5})$$

If the residual field is transformed under the translation, it is found to be invariant. This implies:

$$P[F | \Gamma_1] = P[F_1 | \Gamma_1] = P[F | \Gamma_2] = P[F_2 | \Gamma_2] = \quad (\text{C.6})$$

Appendix D

Overview configurations

A complete overview of the configurations generated in chapter three. First a table of the density constraints will be presented, followed by peculiar velocity and shear constraints. Density constraints (peaks)

Velocity constraints

# objects	R_f [Mpc]	constraints	values
1	$4h^{-1}$	height shape velocity	$\nu = 2.5\sigma$ $a_{12} = a_{13} = 1$ $v_x = 850 \text{ km/s}$
1	$4h^{-1}$	height shape velocity	$\nu = 2.5\sigma$ $a_{12} = a_{13} = 1$ $v_y = 850 \text{ km/s}$
1	$4h^{-1}$	height shape velocity	$\nu = 2.5\sigma$ $a_{12} = a_{13} = 1$ $v_z = 850 \text{ km/s}$
1	$4h^{-1}$	height shape velocity	$\nu = 2.5\sigma$ $a_{12} = a_{13} = 1$ $v_x = 250 \text{ km/s}$
1	$4h^{-1}$	height shape velocity	$\nu = 2.5\sigma$ $a_{12} = a_{13} = 1$ $v_x = 500 \text{ km/s}$
1	$4h^{-1}$	height shape velocity	$\nu = 2.5\sigma$ $a_{12} = a_{13} = 1$ $v_x = 750 \text{ km/s}$
1	$4h^{-1}$	height shape velocity	$\nu = 2.5\sigma$ $a_{12} = a_{13} = 1$ $v_x = 1000 \text{ km/s}$
1	$4h^{-1}$	height shape velocity	$\nu = 2.5\sigma$ $a_{12} = a_{13} = 1$ $v_x = 1250 \text{ km/s}$
1	$4h^{-1}$	height shape velocity	$\nu = 2.5\sigma$ $a_{12} = a_{13} = 1$ $v_x = 1500 \text{ km/s}$
2	$4h^{-1}$	height shape velocity	$\nu = 2.5\sigma$ $a_{12} = a_{13} = 1$ $v_x = 1000 \text{ km/s}$
	$4h^{-1}$	height shape velocity	$\nu = 2.5\sigma$ $a_{12} = a_{13} = 1$ $v_x = -1000 \text{ km/s}$
2	$4h^{-1}$	height shape velocity	$\nu = 2.5\sigma$ $a_{12} = a_{13} = 1$ $v_x = 1250 \text{ km/s}$
	$4h^{-1}$	height shape velocity	$\nu = 2.5\sigma$ $a_{12} = a_{13} = 1$ $v_x = -750 \text{ km/s}$

Shear Constraints

# objects	R_f [Mpc]	constraints	values
1	$15h^{-1}$	height curvature shape shear	$\nu = 3\sigma$ $x_d = 15$ $a_{12} = 1, a_{13} = 0.1$ $s_{11} = 50\text{km/s/Mpc}, s_{22} = 50\text{ km/s/Mpc}$
1	$15h^{-1}$	height curvature shape shear	$\nu = 3\sigma$ $x_d = 15$ $a_{12} = 1, a_{13} = 0.1$ $s_{11} = 75\text{km/s/Mpc}, s_{22} = 25\text{ km/s/Mpc}$
1	$15h^{-1}$	height curvature shape shear	$\nu = 2\sigma$ $x_d = 15$ $a_{12} = 0.1, a_{13} = 0.1$ $s_{11} = 100\text{km/s/Mpc}, s_{22} = -50\text{ km/s/Mpc}$
1	$15h^{-1}$	height curvature shape shear	$\nu = 2\sigma$ $x_d = 15$ $a_{12} = 0.1, a_{13} = 0.1$ $s_{11} = 100\text{km/s/Mpc}, s_{22} = -25\text{ km/s/Mpc}$

	# objects	R_f [Mpc]	constraints	values	Note
Reference	1	$4h^{-1}$	height curvature shape orientation	$\nu = 3\sigma$ $x_d = 10\sigma_2$ $a_{12} = a_{13} = 1$ $\alpha = \beta = \varphi = 0$	
	1	$4h^{-1}$	height	$\nu = 1\sigma$	
	1	$4h^{-1}$	height	$\nu = 2\sigma$	Curvature, shape and orientation equal to reference
	1	$4h^{-1}$	height	$\nu = 3\sigma$	Curvature, shape and orientation equal to reference
	1	$4h^{-1}$	height	$\nu = 5\sigma$	Curvature, shape and orientation equal to reference
	1	$4h^{-1}$	height	$\nu = 7\sigma$	Curvature, shape and orientation equal to reference
	1	$4h^{-1}$	height	$\nu = 10\sigma$	Curvature, shape and orientation equal to reference
	1	$4h^{-1}$	height	$\nu = -3\sigma$	Shape and orientation equal to reference. Curvature $x_d = -10\sigma_2$
	1	$4h^{-1}$	curvature	$x_d = 5\sigma_2$	Height, shape and orientation equal to reference
	1	$4h^{-1}$	curvature	$x_d = 20\sigma_2$	Height, shape and orientation equal to reference
	1	$4h^{-1}$	curvature	$x_d = -20\sigma_2$	Shape and orientation equal to reference. Height $\nu = -3\sigma$
	1	$4h^{-1}$	shape	$a_{12} = 1, a_{13} = 2.5$	
	1	$4h^{-1}$	shape	$a_{12} = 1, a_{13} = 2.5$	Orientation equal to reference. Height $\nu = -3\sigma$ and curvature $x_d = -10\sigma_2$
	1	$4h^{-1}$	orientation	$\alpha = \beta = 45$	Height, shape and curvature equal to reference
	1	$4h^{-1}$	orientation	$\alpha = \beta = 45$	Shape equal to reference. Height $\nu = -3\sigma$ and curvature $x_d = -10\sigma_2$
	2	$4h^{-1}$	height	$\nu = 3\sigma$	
		$4h^{-1}$	shape	$a_{12} = a_{13} = 1$	
		$4h^{-1}$	height	$\nu = 4\sigma$	
		$4h^{-1}$	shape	$a_{12} = 1.1, a_{13} = 0.8$	
	3	$4h^{-1}$	height	$\nu = 3\sigma$	
		$4h^{-1}$	shape	$a_{12} = a_{13} = 1$	
		$4h^{-1}$	height	$\nu = 4\sigma$	
		$5h^{-1}$	shape	$a_{12} = 1.1, a_{13} = 0.8$	
		$5h^{-1}$	height	$\nu = 3.5\sigma$	
		$5h^{-1}$	shape	$a_{12} = a_{13} = 2$	
	3	$4h^{-1}$	height	$\nu = 3\sigma$	
		$4h^{-1}$	shape	$a_{12} = a_{13} = 1$	
		$4h^{-1}$	height	$\nu = 4\sigma$	
		$5h^{-1}$	shape	$a_{12} = 1.1, a_{13} = 0.8$	
		$5h^{-1}$	height	$\nu = -3.5\sigma$	
		$5h^{-1}$	shape	$a_{12} = a_{13} = 2$	

Appendix E

General solution time-independent Schrodinger equation in spherical coordinates

In a spherical coordinate system, the density field can be described by spherical harmonics multiplied by a spherical Bessel function instead of planar waves. This can be retrieved from the time-independent Schrodinger equation, which is given by:

$$\hat{H}\varphi = E\varphi \quad (\text{E.1})$$

with the \hat{H} Hamiltonian operator and the energy E can be given as $\hbar^2 k^2/2m$, where \hbar is the Planck constant h divided by 2π , k is the wave number and m is the mass of the particle. In spherical coordinates the operator \hat{H} can be given as follows:

$$\hat{H} = \frac{\hat{p}_r^2}{2m} + \frac{\hat{L}}{2mr} \quad (\text{E.2})$$

where for the radial momentum \hat{p}_r can be found:

$$\hat{p}_r = -i\hbar \frac{1}{r} \frac{\partial}{\partial r} r \quad (\text{E.3})$$

and for the angular momentum \hat{L} :

$$\hat{L} = \hbar^2 \left[\frac{1}{\sin\theta} \frac{\partial}{\partial\theta} \left(\sin\theta \frac{\partial}{\partial\theta} \right) + \frac{1}{\sin^2\theta} \frac{\partial^2}{\partial\phi^2} \right] \quad (\text{E.4})$$

The solution for the wave function can be found by separating of variables:

$$\varphi_{klm}(r, \theta, \phi) = R_k(r) Y_l^m(\theta, \phi) \quad (\text{E.5})$$

For the radial part of the solution, the time-independent Schrodinger equation becomes:

$$\left[- \left(\frac{1}{r} \frac{d^2}{dr^2} r \right) + \frac{l(l+1)}{r^2} \right] R_{kl}(r) = \frac{2mE}{\hbar^2} R_{kl}(r) \quad (\text{E.6})$$

By substituting the variables $E \equiv \hbar^2 k^2 / 2m$ and $x \equiv kr$, the above equation becomes a spherical Bessel differential equation:

$$\frac{d^2}{d^2 r} R(x) + \frac{2}{x} \frac{dR(x)}{dx} = \left[1 - \frac{l(l+1)}{x^2} \right] R(x) = 0 \quad (\text{E.7})$$

For the angular momentum, the solutions can be found by solving the time-independent Schrodinger equation for the angular momentum squared and the angular momentum in the x , y or z direction. Since the last three operators all commute with the angular momentum squared operator, the eigenfunctions are the same.

$$\widehat{L}^2 \varphi_{lm} = \hbar^2 l(l+1) \varphi_{lm} \quad (\text{E.8})$$

$$\widehat{L}_z \varphi_{lm} = \hbar m \varphi_{lm} \quad (\text{E.9})$$

The solutions for the eigenfunctions are called spherical harmonics and denoted by the symbol $Y_l^m(\theta, \phi)$. When solving the above equations for the angular momentum operator \widehat{L}_z , it can be found that:

$$\frac{\partial}{\partial \phi} Y_l^m = im Y_l^m \quad (\text{E.10})$$

This determines only the ϕ -dependence of the solution, which means that the eigenfunctions Y_l^m can be separated by variables into:

$$Y_l^m(\theta, \phi) = \Phi_m(\phi) \Theta_l^m(\theta) \quad (\text{E.11})$$

The set of functions $\Phi_m(\phi)$ is defined by:

$$\Phi_m(\phi) = \frac{1}{\sqrt{2\pi}} e^{im\phi} \quad (\text{E.12})$$

with m being a positive or negative integer or zero. Then the Y_l^m has the form of:

$$Y_l^m(\theta, \phi) = \frac{1}{\sqrt{2\pi}} e^{im\phi} \Theta_l^m(\theta) \quad (\text{E.13})$$

When substituting the above equation into the time independent Schrodinger equation with the angular momentum squared operator and inserting the expression for the angular momentum operator squared, the following expression for the set of functions $\Theta_l^m(\theta, \phi)$ can be found with variable $\mu \equiv \cos\theta$:

$$\frac{d}{d\mu} \left[(1 - \mu^2) \frac{d\Theta_l^m}{d\mu} \right] + \left[l(l+1) - \frac{m^2}{1 - \mu^2} \right] \Theta_l^m = 0 \quad (\text{E.14})$$

The solutions to these functions are the so-called associated Legendre polynomials $P_l^m(\mu)$ multiplied by a factor.

$$\Theta_l^m(\mu) = \left[\frac{2l+1}{2} \frac{(l-m)!}{(l+m)!} \right]^{1/2} P_l^m(\mu) \quad (\text{E.15})$$

where $P_l^m(\mu)$ are given by a differential form of the formula of Rodrigues:

$$P_l^m(\mu) = (-1)^m (1 - \mu^2)^{m/2} \frac{d^m P_l(\mu)}{d\mu^m} \quad (\text{E.16})$$

where $P_l(\mu)$ is given by the actual formula of Rodrigues:

$$P_l(\mu) = \frac{1}{2^l l!} \frac{d^l}{d\mu^l} (\mu^2 - 1)^l \quad (\text{E.17})$$

This will give the final solution for the wave function to be:

$$\varphi_{\mathbf{k}} = j_l(k_n r) Y_l^m(\theta, \phi) \quad (\text{E.18})$$

E.1 Expressions for the spherical harmonics and spherical Bessel functions

Below here there are some expressions for a few of the spherical harmonics and the spherical Bessel functions;

Spherical Bessel Functions

$$\begin{aligned} Y_0^0 &= \left(\frac{1}{4\pi}\right)^{1/2} \\ Y_1^1 &= -\frac{1}{2} \left(\frac{3}{2\pi}\right)^{1/2} \sin\theta e^{i\phi} \\ Y_1^0 &= \frac{1}{2} \left(\frac{3}{\pi}\right)^{1/2} \cos\theta \\ Y_1^{-1} &= \frac{1}{2} \left(\frac{3}{2\pi}\right)^{1/2} \sin\theta e^{-i\phi} \\ Y_2^2 &= \frac{1}{4} \left(\frac{15}{2\pi}\right)^{1/2} \sin^2\theta e^{2i\phi} \\ Y_2^1 &= -\frac{1}{2} \left(\frac{15}{2\pi}\right)^{1/2} \sin\theta \cos\theta e^{i\phi} \\ Y_2^0 &= \frac{1}{4} \left(\frac{5}{\pi}\right)^{1/2} (3\cos^2\theta - 1) \\ Y_2^{-1} &= \frac{1}{2} \left(\frac{15}{2\pi}\right)^{1/2} \sin\theta \cos\theta e^{-i\phi} \\ Y_2^{-2} &= \frac{1}{4} \left(\frac{15}{2\pi}\right)^{1/2} \sin^2\theta e^{-2i\phi} \end{aligned}$$

Spherical harmonics

$$\begin{aligned} j_0(x) &= \frac{\sin x}{x} \\ j_1(x) &= \frac{\sin x}{x^2} - \frac{\cos x}{x} \\ j_2(x) &= \left(\frac{3}{x^3} - \frac{1}{x}\right) \sin x - \frac{3}{x^2} \cos x \\ j_3(x) &= \left(\frac{15}{x^3} - \frac{6}{x}\right) \frac{\sin x}{x} - \left(\frac{15}{x^2} - 1\right) \frac{\cos x}{x} \end{aligned}$$